**warwick.ac.uk/lib-publications**

# TRANSITION TO COLLECTIVE MOTION OF SPERMATOZOA IN DIFFERENT CONFINEMENTS AND AT VARIABLE TEMPERATURES.

by

MARIA CHIARA ROFFIN

A thesis submitted to the University of Warwick for the degree of

**Doctor of Philosophy in Physics**

UNIVERSITY OF WARWICK, DEPARTMENT OF PHYSICS

May 2019

# Acknowledgements

This journey, culminating in this thesis, would have not been possible without the help and support of many people. I will try to not forget anyone. First and foremost, I would like to thanks my supervisors Dr. Vasily Kantsler and Dr. Petr Denissenko for their support and help during this journey, you thaught me a lot. I would like to thank our collaborator Anton Bukatin for the help and the enlightening discussions.

Secondly, I have to admit that this experience would have not been competed without the unconditional support of my parents, they are the source of all my strength and a never ending flow of support and help, always ready to listen to my problems, mostly my mother, for never having "peli sulla lingua" and telling me things as they are. Sometimes problems look so big without your point of view on the situation. My family, what are we without our family? For myself I can say I would be nobody, I don't think they understand how much strength they give me every time we speak. I wish that I can make my grandmothers proud, and even if Nonna Gio is not very happy I do not have lunch with her every Saturday, I hope she is proud of me and happy to be here for the end of this journey too, I do remember the day she told me she would have never seen me graduating, hopefully this will be the third time! My cousins, the distance brought us close together, I thank you for checking up on me on the hard times and for making my trips to Aosta the best possible. My uncles and auntie, we had so many health issues in this past four years, but we powered through them all and here we are. I would like to give a special thanks to Martina. Since she was born she has been the brightest moment of my days, I am so happy I am your "auntie" and I hope I can help you in your future as I you helped me. You are the best part of my days, I am so grateful to your parents for letting me call you so many times, for letting me be part of your life and to tell you about crazy auntie Maria.

I would like to thank my Dominican family, 10 years ago I arrived in you family and you adopted me as if I was one of your daughters. I am so proud to be part of your family. Galia, you smiley little girl, I can't wait to meet you!

There are two special people in my life, that I cannot consider simply my friends. The first one is Didier, you have been my friend for my entire life, I cannot remember a single year without your presence. Your courage and soul inspire me every day! You will always be my little brother. And then there is Marika. She is the most amazing woman I know, if she

won't conquer the world I don't know who could! I miss you every single day and I feel like the luckiest woman on Earth to have you as a friend.

And finally, to say so, the humongous list of friends that helped me through this 4 long, but they still flew by, years. In order to not forget anyone, let's start with the italian friends: Stefano Merola, your friendship is so valuable to me, you are always there for my good and bad moment, I wish you the best, you deserve it. Federica Pizzato, thanks for the support and for always finding time to come visit me, you made me feel back at home every year. My girls, Federica Russo, Manuela and Marisol: you girls have contagious smiles, but I am still waiting for you to come visit me!

And then we have the British friends, I couldn't imagine that I would have so many. Starting with my house mates: Andrea, we shared the house since day one, what a journey! Thank you for being there for me even in the bad moments; Matt, thanks for being there to pick me up at the darkest time, I don't think I would have made it out of it without you and your powerful hugs! Sam, I know I thank you every day, but really, thank you so much. You arrived and made everything better. But let's be honest, two friends have been the most important in this Country: Zach, I cannot begin to describe the happiness I feel seeing his smiley face! He is the most positive man I crossed path with and I feel lucky to have him as my friend, I would even dare saying my best friend. And finally I have Katie (and Jed), you not only were worried sick for me when I was at my worst, but you were there to pick up the pieces and to help through that damn depression. You were the one I could turn to for comfort and you were always there for me, ever when at the hospital! I can just say "Thank you for everything!"

We can then turn the attention to my fellow colleagues, this office was less of a prison with you guys in it. Richard, thank you for dealing with my technology debacles, now that you left I won't be able to have my PC working. Max, thanks for the uncountable coffees together and for introducing me to DnD, I swear that as soon as this is finished I will be back!

I would like to give one last thank to the people of the library caf. They have always been there to hand me coffees, which, let's be honest is as vital as blood. But they went over that, Mirko, Vanessa, Becky, Davide and Kelly, you guys were there for a smile and for kind words. I always say that you guys adopted me!

I think these are all the people that matter. Guys, we made it! Each and every one of you helped to make this possible, I hope I made you proud.

# Declaration

I declare that this thesis reports my work between May 2015 and May 2019 under the supervision of Dr. Vasily Kantsler and Dr. Petr Denissenko. The studies in this thesis have not been submitted either in full or in part to this or any other academic institution for the admission of a higher degree. The work is the candidate's own work, except when indicated otherwise by reference in the text. Any views expressed is this thesis is the one of the author.

# Contents

*" Look, this is no time to doubt our mission. You took an oath when you entered sperm training school: to fertilize an ovum or die trying. "*

Everything you always wanted to know about sex but were afraid to ask.

- Woody Allen -

# Abstract

Sperm motility and its collective motion is a subject still poorly investigated. We aim at studying different environmental conditions that can and do affect the motility of sperm cells, focusing into transitions to collective motion.

With increasing concentration of swimmers, sperm cells in a suspension can switch from random motion to organised collective turbulence, which we call "spermulence". This phase transition is strongly influenced by the boundaries of the system, which influence conditions for the transition to spermulence. Complexity of the boundary may lead to oscillatory modes where the flow in suspension reverses periodically. Moreover, the confinement can be used by the swimming sperm cells as an efficient strategy to progress towards a point and this particular phenomenon can be important when designing methods for artificial insemination.

In addition to the confinement, other environmental conditions, such as temperature and fluid viscosity, would influence the motion of sperm cells. We demonstrate that cells change the radius of curvature of their trajectories when swimming in a hotter environment. This change in trajectory will result in formation of ring-like structures in a two dimensional system, that will turn into a oscillatory motion, with waves propagating throughout the entire system. Self-organisations on such a wide scale and with such consistency have not been yet seen in the spermatozoa investigations.

While working with sperm cells, a new method for swarming bacterial experiments has been invented, allowing for bacteria to live on an agar plate and move in the space for long times compared to their usual live span in devices. This techniques allow bacteria to swarm for hours on agar surface previously modified with the desired structure.

# Chapter 1

# Introduction

## 1.1 Introduction

The displays of collective moving animals, like fishes or birds, can result most fascinating. But systems of animals moving in space are not the only examples of interacting moving units. With the advance in technology, new physical and chemical systems show interacting properties of the self-propelled particles composing the moving units of the system. Indeed, the extremely small has very captivating structures that resemble the one seeing by animals. In the past few decades there has been a lot of interest about the microscale interaction that lead highly concentrated systems of swimming units to move collectively in the space either for long or short period of times. Many studies concentrates on the easy units to grow and to model, like *Escherichia coli* or *Bacillus subtilis* bacteria, or others look at the swimming algae like *Chlmydomonas*. But many more biological "animacules" not only swim, but create fascinating turbulent structures. For decades ram owners have been aware of the *"spermulence"* arising within highly concentrated samples of high motility sperm cells. This phenomenon is so well known that up to now, the method to asses the quality of the ram sperm samples relies on the visual inspection of the collected sample and on the experience of the farmer to define where on the 1 to 5 scale the turbulence can be placed. It is necessary to control the collected samples to be able to filter through and chose the best and most motile one for the fertilization, so that the chances of a successful in loco fecundation can be as high as possible. It is hence important for farmers to have a reliable fecundation rate for their animals, if not so, the economical feedback could be detrimental.

Most importantly, the recent decrease in fertility rates for humans sample is very alarming, making the study of the motility property of sperm cells very important.

The aim of this work is to look at the not so explored world of sperm motion trying to understand as much as we can about it. Mostly, understanding how the fluid property

change depending on concentrations, with transition from chaotic to collective motion or by confinement. We are interested in seeing what conditions can lead to a more efficient displacement of spermatozoa. Finally, since in the female body the sperm cells have to travel towards the ovum, it is important to understand the correlation between cell motion versus the temperature of the system.

## 1.2 Outline of the thesis

This works start with Chapter 2, explaining the fundamentals of motility in a low Reynolds number environment, the cell hydrodynamical interactions, the model for collective motion simulation and analysis. Finishing with an explanation of the biological structures of the spermatozoa. Chapter 3, concentrates on the experimental methods, looking briefly at the microscopy techniques used, the soft lithography for channel making and the particle image velocimetry techniques used for the image analysis.

The first experimental chapter, Chapter 4, focuses on the transition from random to collective motion for sperm cells in a bulk environment. We analyse the density conditions for the phase transition to happen. The next chapter, Chapter 5, looks at the role of confinement in the transition to collective motion. We then look at highly concentrated suspensions and how the shape of the environment they are confined in modifies the overall spermulence. We conclude in Chapter 6, where we change another environmental condition: the temperature. We analyse how this temperature variation affect both the single cell and collective motion of the fluid.

# Chapter 2

# Swimming at a microscale

In this first chapter of the thesis, we would like to introduce some basic concepts of fluid dynamic at the microscale that can be used to understand the systems we describe for collective motion of self-propelled microswimmers. In addition, we review the simplest model that can be used to describe a collective system of self-propelled particles. Finally, we will describe the biological and morphological components of the swimmers that we will use in this work, the spermatozoon.

## 2.1 Fluid Dynamics at Low Reynolds Number

Considering an organism in a fluid, in order to find the force distribution acting on the organism, it is necessary to solve for the flow field $\boldsymbol{u}$ and the pressure $p$ in the fluid surrounding the organism. The flow satisfied the Navier-Stokes equations, in case of an incompressible Newtonian fluid with density $\rho$ and viscosity $\eta$.

$$\rho\left(\frac{\partial}{\partial t} + \mathbf{u} \cdot \nabla\right)\mathbf{u} = -\nabla p + \eta \nabla^2 \mathbf{u}; \qquad \nabla \cdot \mathbf{u} = 0 \tag{2.1}$$

That will need boundary conditions appropriate to the considered system, for example for a deformable body swimming with no-slip boundary conditions, the velocity of the material points on the body surface are equal to the one at the boundary.

When flow field and pressure are known, the stress tensor can be defined as:

$$\boldsymbol{\sigma} = -p\mathbb{1} + \eta[\nabla \mathbf{u} + (\nabla \mathbf{u})^\mathsf{T}] \tag{2.2}$$

where $\mathbb{1}$ is the identity tensor. The stress tensor can be used to define the hydrodynamic force $\boldsymbol{F}$ and torque $\boldsymbol{T}$ by integrating over the surface $S$ of the body:

$$\mathbf{F}(t) = \int\int_S \boldsymbol{\sigma} \cdot \mathbf{n} dS;$$

$$\mathbf{T}(t) = \int\int_S \mathbf{x} \times (\boldsymbol{\sigma} \cdot \mathbf{n}) dS \tag{2.3}$$

where $\boldsymbol{n}$ is the unit vector normal to the surface and $\boldsymbol{x}$ is the position on the surface of the body.

### 2.1.1 The scallop theorem

The Reynolds number is a dimensionless quantity, and can be interpreted in different physical ways, but the classical interpretation is the ratio between the inertial and viscous forces per unit volume in the fluid. In fact, let's consider an object of size $a$ and velocity $\boldsymbol{u}$ moving in a fluid with viscosity $\eta$ density $\rho$ and kinematic viscosity $v$ the Reynolds number is defined as:

$$Re = \frac{au\rho}{\eta} = \frac{au}{v} \tag{2.4}$$

When looking at the case of a micro-swimmer, like a sperm cell, of size $\sim 50\mu m$, with velocity $u \sim 50\mu m$, swimming in water (in water $v \sim 10^{-6}m^2s^-1$), the Reynolds number is $Re \approx 10^{-4} \ll 1$. Swimming at low Reynolds numbers the viscous forces dominates over the inertial one on the fluid. Hence, considering the limit of $Re = 0$, the Navier-Stokes equations (2.1), can be simplified into the Stokes equations:

$$-p + \eta\nabla^2\mathbf{u} = 0; \qquad \nabla \cdot \mathbf{u} = 0 \tag{2.5}$$

Which is a linear and time independent equation, hence symmetric under time reversal, meaning that what is happening at low Reynolds number at a specific time is determined only by the forces exerted on the object at that specific time and completely independent from the forces acting on the object in the past.

This characteristic is important for swimmers that change their shape periodically, as explained in the so called "scallop theorem" by Purcell in 1977 [1].

If we define swimming as a series of body deformations that propel the body and leads to motion in the fluid, to able to move in low Reynolds number conditions, the deformation has to be cyclical and not dependent on external forces.

The reciprocal motion can be defined as that specific type of motion where the body undergoes a deformation and goes back to the initial form through the same deformation in reverse. At low Reynold number, this type of motion doesn't result in movement, since it retraces the deformation already done but backwards, resulting in a net null motion.
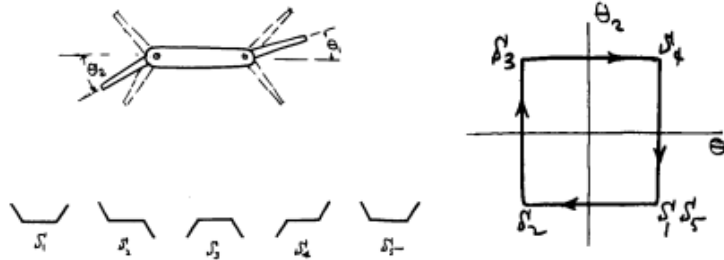
Figure 2.1: Purcell swimmer, from Purcell talk in 1977 [1]. Two hinged swimmer that moved the extremities in a cyclical motion, each space configuration from $S_1$ to $S_5$ correspond to a point in the configuration space that instead of being reciprocal, moves in a cyclical path in the $\theta_1$ to $\theta_2$ space.
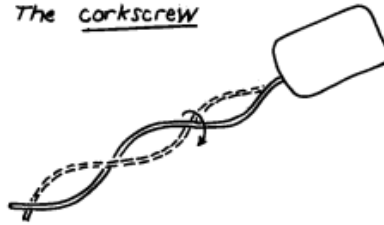


Figure 2.2: Real solutions for purcell swimmers, again from the talk in 1977, [1]. The first one is a flexible oar with the two parts deform separately, while the second is a corkscrew swimmer, which rotating on itself moves in space.

An example of a real swimmer not able to move in low Reynolds number environment is the scallop. A scallop in order to move opens and closes the shell, squirting water outside. This type of motion would result in a return to the initial position of the scallop, without any net movement of the animal.

The reason why a scallop won't move in low Reynolds number is that its shape deformation has only one degree of freedom in the configuration space, which makes him reverse to the initial position without actually moving forward, as it happens at higher Reynolds numbers. The so called Purcell swimmer, is the easiest version of a low Reynolds number swimmer, and it has two hinges that moves cyclically in a 2 dimensional configuration space as shown in figure 2.1. It moves from configuration $S_1$ to $S_5$ moving around the $\theta_1$ and $\theta_2$ coordinates in the configuration space, not moving reciprocally in the configuration space, hence being able to actually move in space.

Other possible swimmers can be imagined to be able to swim in the low Reynolds world. The two most common solution to the low Reynolds conundrum: the flexible oar and the corkscrew, fig. 2.2. The first one is a flexible oar deforming, in which the top and bottom part of the oar bend separately and at different times, not creating a reciprocal movement and making it possible for the swimmer to move. The corkscrew swimmer, in this type of motion the animal keeps turning on itself, creating a non reciprocal motion and propelling it.

### 2.1.2 Motion of a solid body

Considering a solid body in a viscous fluid, the Stokes equation (2.5), is linear. If $\mathbf{F}$ is the external force exerted on the body and $\mathbf{T}$ the external torque, the body will have a velocity U and a rotation rate $\Omega$, which satisfy:

$$
\begin{pmatrix} F \\ T \end{pmatrix} = \begin{pmatrix} A & B \\ B^T & C \end{pmatrix} \cdot \begin{pmatrix} U \\ \Omega \end{pmatrix}; \qquad \begin{pmatrix} U \\ \Omega \end{pmatrix} = \begin{pmatrix} M & N \\ N^T & O \end{pmatrix} \cdot \begin{pmatrix} F \\ T \end{pmatrix} \tag{2.6}
$$

The matrix on the left hand side is called "resistance" matrix of the body, while the right hand side one is the "mobility" matrix [2]. We then consider the reciprocal theorem [3], which is a property of the Stokes flows and depends on their linearity. If we have a volume V, bounded by a surface S with $\mathbf{n}$ being its outward normal, in V there are two solutions of the Stokes equation, eq. (2.5), named $\mathbf{u}_1$ and $\mathbf{u}_2$, that satisfy at infinity the same boundary condition, then $\boldsymbol{\sigma}_1$ and $\boldsymbol{\sigma}_2$ are the respective stress flows, then the reciprocal theorem states that the mixed virtual works are equal:

$$
\int\int_S \mathbf{u}_1 \cdot \boldsymbol{\sigma}_2 \cdot \mathbf{n} dS = \int\int_S \mathbf{u}_2 \cdot \boldsymbol{\sigma}_1 \cdot \mathbf{n} dS \tag{2.7}
$$

This property of the fluid is important because it forces the two matrices to be symmetric [3].

Quickly doing a dimensional analysis on the matrix system we have that, at low Reynolds number, the stresses scale as $\sim \eta U/L$, then the sub-matrix $[A] \sim \eta L \sim [M]^{-1}$, $[B] \sim \eta L^2 \sim [N]^{-1}$, and $[C] \sim \eta L^3 \sim [O]^{-1}$.

Looking at the case of a solid sphere of radius R the submatrices take the following values: $\mathbf{A} = \mathbf{M}^{-1} = (6\pi\eta R)\mathbf{I}$ and $\mathbf{C} = \mathbf{O}^{-1} = (8\pi\eta R^3)\mathbf{I}$, while the cross-coupling terms, N and B, vanish by symmetry.

This two matrix equations allow us to describe three major properties. The first one is the drag anisotropy, crucial for motion at Reynolds number near zero, as discussed in subsection 2.1.4. To satisfy the drag anisotropy, the matrices $\mathbf{A},\mathbf{M},\mathbf{C}$ and $\mathbf{O}$ have to be not isotropic.

The second property is that specific geometries, like chiral bodies, have non zero **B** and **N** submatrices, hence, when there is no mirror symmetry plane, the translational motion can be driven by angular forcing. Finally, these matrices can be used to calculate the diffusion constants of solid bodies.

### 2.1.3   Flow singularities

Given the linearity of the Stokes equations, eq. (2.5), there is a possibility to solve for the pressure and flow through the mathematical methods using linear superimposition of solution.

The Green function is the classical solution and for a point force, defined as a Dirac-delta function ($\delta(\mathbf{x} - \mathbf{x}')\mathbf{F}$) is:

$$\mathbf{u}(\mathbf{x}) = \mathbf{G}(\mathbf{x} - \mathbf{x}') \cdot \mathbf{F} \tag{2.8}$$

where the tensor **G** is called Oseen tensor, the term stokeslet [4], is the fundamental solution of eq. (2.8) for the Oseen tensor and it is defined as:

$$\mathbf{G}(\mathbf{r}) = \frac{1}{8\pi\eta}\left(\frac{\mathbf{I}}{r} + \frac{\mathbf{r}\mathbf{r}}{r^3}\right), \qquad r = |\mathbf{r}| \tag{2.9}$$

For the pressure we have:

$$p(\mathbf{x}) = \mathbf{H}(\mathbf{x} - \mathbf{x}') \cdot \mathbf{F}, \quad \text{with} \quad \mathbf{H}(\mathbf{r}) = \frac{\mathbf{r}}{4\pi\mathbf{r}^3} \tag{2.10}$$

A stoklet is a representation of the flow created on the fluid by a point force **F**, as a singularity at the position $\mathbf{x}'$. The decay of the velocity field in space goes like $1/r$. We can easily show the decay if we consider a 3D force **F** on the fluid and linearity of the Stokes flow, the flow velocity will be dependent on $\theta$, which is the angle between the force **F** and the distance $\mathbf{r}$, as: $u \sim Ff(\theta, \mathbf{r}, \eta) \sim g(\theta)F/\eta r$, with F being just the magnitude of the force.

A very important property of the stokeslet solutions is the directional anisotropy. Starting from eq. (2.9), we evaluate the velocity in the direction parallel and perpendicular to the direction of the applied force **F**, obtaining $u_\parallel = F/4\pi\eta r$ and $u_\perp = F/8\pi\eta r$, which results in a perpendicular flow twice as big as the perpendicular: $u_\parallel = 2u_\perp$. This anisotropy is the same as the anisotropy defined in the previous section, from eqs. (2.6), that drives the motion for long slender bodies, as explained in section 2.1.4.

By differentiating the fundamental solution [5], eq. (2.9), we obtain the complete set of singularities for the viscous flow. The first derivative gives a flow field decaying as $1/r^2$, which is the force dipole, the second gives a source dipole and a force quadrupole, with a velocity decay of $1/r^3$, and so on.

Using the flow past a sphere example used in the previous chapter [5], the solution for that problem, is a combination of a stokeslet and a source dipole at the center of the sphere.

In a low Reynolds number environment, the motion of the boundaries created an instantaneous response in the fluid, hence the rate at which the particle in the fluid are carried in the flow is slower than the diffusivity of the velocity perturbations in the fluid. This means that the momentum of a swimmer changes at a rate that is negligible compared to the magnitude of the forces from the surrounding viscous fluid. Hence, Newton's law becomes and instantaneous balance of forces/torques:

$$\mathbf{F}_{ext}(t) + \mathbf{F}(t) = 0, \qquad \mathbf{T}_{ext}(t) + \mathbf{T}(t) = 0 \tag{2.11}$$

Consequently, the cells are force and torque free while swimming at low Reynolds number, leading to the exclusion of the flow singularities that describe point force and point torque while looking at the far field system [6]. Given that it is possible to describe the flow by multiple flow singularities, the one with the slowest decay in space is the one dominating in the far-field. Hnce, when a cell is swimming, the best representation of the far flow field is a symmetric force dipole or stresslet [7]. The far field behaviour of a swimming cell is important when looking at the hydrodynamic interactions.

Finally, the presence of solid boundaries modify the flow singularities. We will look at the interaction of swimmers with the boundaries later in this chapter.

### 2.1.4 Drag based theory

Let's consider a body submerged in a viscous fluid, with its surface deforming in a time-varying way with velocity field on its surface $\mathbf{u}_s(t)$. At every instant this swimmer can be considered a solid body with velocity $\mathbf{U}(t)$ and rotation $\mathbf{\Omega}(t)$. On the swimmer's surface the instantaneous velocity is $\mathbf{u} = \mathbf{U} + \mathbf{\Omega} \times \mathbf{r} + \mathbf{u}_s$. The boundary conditions define the way to derive the velocity $\mathbf{U}$ and torque $\mathbf{\Omega}$. A squirmer is a swimmer whose shape remains constant and all deformations are parallel to the surface. If we consider a spherical squirmer of radius R, the velocity and the rotation of the swimmer are [8]:

$$\mathbf{U} = \frac{1}{4\pi R^2} \int\int_S \mathbf{u}_s dS; \qquad \mathbf{\Omega} = \frac{3}{8\pi R^3} \int\int_S \mathbf{n} \times \mathbf{u}_s dS$$

After considering the solid body interacting with the fluid, we have to look how to model the flagellum that propels the body. To model a flagellum of a sperm cell we can represent the flagellum as a collection of short filaments which movement can be described as follow.

Considering a thin filament immersed in a fluid and deforming in time, the flow it creates will induces movement on the filament itself. The tangent vector $\mathbf{t}$ s describes the filament,
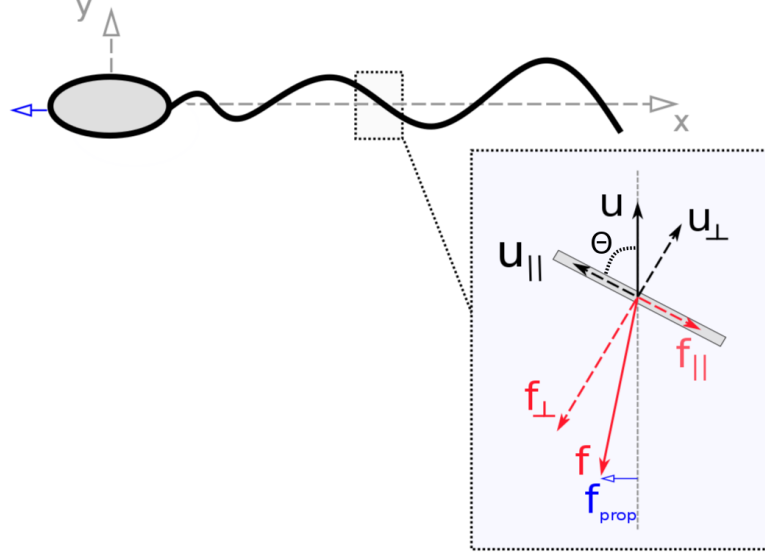
Figure 2.3: The anisotropy in slender filaments allow for a propulsive force to arise, figure from [2].

where s is the distance along the filament where the tangent vector is positioned. The instantaneous deformation is defined by the velocity field $\mathbf{u}(s,t)$, at distance s and time t. The resulting local viscous drag force per unit length, which is opposing the motion of a slender filament is defined as:

$$\mathbf{f} = -\zeta_\parallel \mathbf{u}_\parallel - \zeta_\perp \mathbf{u}_\perp \tag{2.12}$$

with $\mathbf{u}_\parallel$ and $\mathbf{u}_\perp$ being the projections of the local velocity on the local filament tangent and the $\zeta_{\parallel,\perp}$, being the corresponding drag coefficients.

Back at considering the flagellum, modelled by short straight segments, moving with velocity $u$ at an angle $\theta$, as shown in figure 2.3. We then project to the filament obtaining: $u_\parallel = u\cos\theta$, $u_\perp = u\sin\theta$, $f_\parallel = -\zeta_\parallel u_\parallel = -\zeta_\parallel u\cos\theta$ and $f_\perp = -\zeta_\perp u_\perp = -\zeta_\perp u\sin\theta$. In case of isotropic drag we have that $\zeta_\parallel = \zeta_\perp$, resulting in a force directed as the velocity of the filament. However, if the drag is anisotropic ($\zeta_\parallel \neq \zeta_\perp$), the drag has an additional component, perpendicular to the direction of the velocity [9, 10], $f_{prop}$:

$$\mathbf{f}_{prop} = (\zeta_\parallel - \zeta_\perp)u\sin\theta\cos\theta\mathbf{e}_x \tag{2.13}$$

From Purcell's scallop theorem, we know that the filament velocity $u$ and its orientation $\theta$ have to vary periodically in time in order to obtain a net propulsion. And for biologically bodies, with a flagellum of length L, with a small amplitude $y(x,t)$, the generated propulsive force on the filament, eq. (2.13), gives:

$$\mathbf{F}_{prop} \sim (\zeta_\perp - \zeta_\parallel) \int_0^L \left( \frac{\partial y}{\partial t} \frac{\partial y}{\partial x} \right) dx \mathbf{e}_x \tag{2.14}$$

Considering a planar wave deformation, which travels in the x direction as $y(x,t) = f(x - ct)$ we then have that $\mathbf{F}_{prop} = c(\zeta_\parallel - \zeta_\perp) \int f^2(\eta) d\eta \mathbf{e}_x$, with $\eta$ being the viscosity, where propulsion is directed opposite to the one of the wave. With a wave-like movement, the product $\left( \partial y/\partial t \cdot \partial y/\partial x \right)$ has a constant sign over all the filament, hence all the parts composing the filament, contribute to the propulsion [11].

In a real flagellum, though, the deformations are not of small amplitude, hence the model has to be modified to account the large amplitude deformations, but since we are considering real flagella, the fact that they are long (L) and thin (a) allow us to model them as slender rods, modelling a flagellum as a line of singular solutions of the appropriate strength of the Stokes flow, which by deforming creates a induced flow in the surrounding fluid.

In a first approximation, let's try to calculate the resistance matrix for a straight rigid rod of length L and radius a, the external force is uniformly distributed over the length of the rods, with constant force per unit length. The rod is modelled by N stokeslets equally spaced along the x-axis, $x_j = (jL/N, 0, 0)$. A short segment of the rod induces a far field flow that is represented by a stokeslet. The force of each stokeslet, when assuming uniformly distributed forces, is equal to $F_{ext}/N$, without considering hydrodynamical interactions between the different segments of the flagellum, the velocity of each segment is $\mathbf{u} = \mathbf{F}_{ext}/\zeta_{seg}$, with $\zeta_{seg} \propto \eta a$ being the resistance coefficient of the segment.

As shown in figure 2.4, when each segment move, it induces a flow that helps the movement of the other segments of the filament, hence the flow induced by the segment j is:

$$\mathbf{u}_j(x) = \frac{1}{8\pi\eta|x - x_j|} (\mathbf{I} + \mathbf{e}_x \mathbf{e}_x) \cdot (\mathbf{F}_{ext}/N)$$

From which is possible to calculate the velocity of the i-th segment in the filament as:

$$\mathbf{u}(\mathbf{x}_i) = \mathbf{F}_{ext}/\eta_{seg} + \sum_{j \neq i} \mathbf{u}_j(\mathbf{x}_i) \tag{2.15}$$

Considering that $N >> 1$, the integral can replace the sum, considering as the integration bounds $-L/2$ and $L/2$, excluding the region of size a around the point $x_i$:

$$\mathbf{u}(\mathbf{x}_i) = \frac{\mathbf{F}_{ext}}{\eta_{seg}} + \frac{1}{8\pi\eta} \int \frac{1}{|\mathbf{x}_i - \mathbf{x}|} (\mathbb{1} + \mathbf{e}_x \mathbf{e}_x) \cdot \mathbf{F}_{ext} \frac{dx}{L} \tag{2.16}$$

Solving the integral and evaluating it disregarding the end effect by using $|x_i| << L$, keeping only the leading order in $\ln(L/a)$ and considering $\mathbf{u}(\mathbf{x}_i)$ constant for a rigid rod, we then obtain [2] :
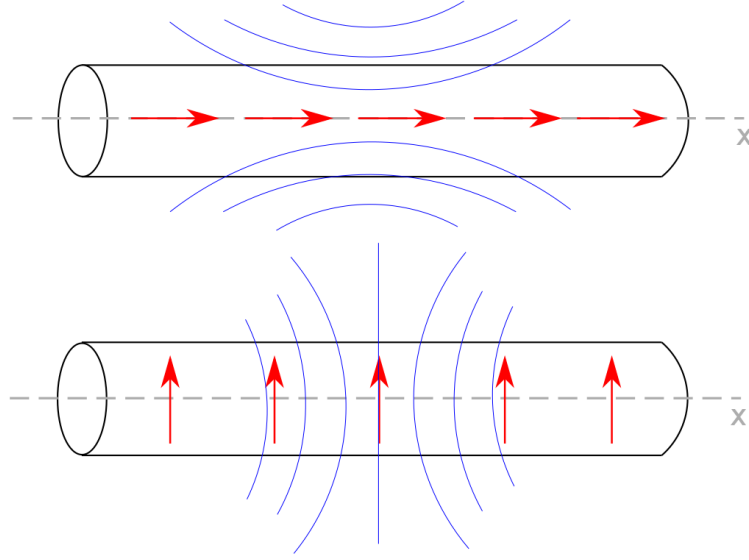
Figure 2.4: Rod subject to external forces: longitudinal in the top figure and perpendicular in the bottom one. Stokeslets are represented by the arrows, while the blue lines are the flow field of the central stokeslet. The rod get pushed by the induced flow of every stokelet in the rod, figure from [2].

$$\mathbf{u} = \frac{\ln(L/a)}{4\pi\eta}(\mathbb{1} + \mathbf{e}_x\mathbf{e}_x) \cdot \mathbf{f}_{ext} \qquad (2.17)$$

where the external imposed force per unit length is $\mathbf{f}_{ext} = \mathbf{F}_{ext}/L$. In this simple model we have no internal cohesive forces, only hydrodynamical force acting in between the differ- ent composing part of the filament. The drag per uni length is $\mathbf{f} = -\mathbf{f}_{ext}$ and the compo- nents of the force perpendicular and parallel to the x-axis are:

$$f_\parallel = -\zeta_\parallel u_\parallel; \qquad f_\perp = -\zeta_\perp u_\perp \qquad (2.18)$$

and $\zeta_\perp = 2\zeta_\parallel = 4\pi\eta/ln(L/a)$. This anisotropy, as mentioned previously in this section and in section 2.1.2, is necessary for the drag-based thrust.

Introducing a small deformation of the filaments, as a gentle curve with $ka << 1$ with $k^2 = |\partial^2 r/\partial s^2|$, where $r(s)$ is the position of the centerline of the filament. If the curvature of the filament is very small, then the solutions are the same as the one for a straight filament. For this local drag theory, eq. (2.17), we considered only the leading order in $1/\ln(L/a)$, which allow this theory to be valid only for exponentially thin filaments [4, 9, 12].

Let's now consider an example, to try to see how the local drag thory shown until now can be used to decribe the problem of a spherical swimmer with prescribed stroke. We look at a spherical body, of radius $R_b$, propelled by a planar sine wave [11] beating like $y(x,t) = b\sin(kx - \omega t)$ and we try to find the flow velocity $\mathbf{U}$ that gives net force and moment on the swimmer equal to zero.
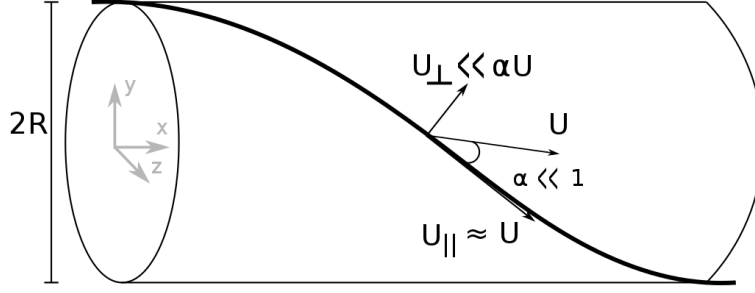
Figure 2.5: Forces acting on a segment of an helical flagellum pulled through a viscous fluid with speed U, figure from [2].

Considering the drag force per unit length, eq. (2.18), acting on the filament, which gives that the total forces per unit length have a propulsive component. We then use equation (2.14) for the propulsive forces that derive from the deformation of the filament and a drag component, which comes from the resistance to x-axis translation for the considered swimmer. Let's consider in addition the drag force on the sphere as: $\zeta_0 R_b U = 6\pi\eta R_b U$ and we balance all the forces acting on both filament and body, finally let's use the sinusoidal wave form and average over a period of the oscillation, we obtain [2]:

$$\langle \mathbf{U} \rangle = -\frac{\zeta_\perp - \zeta_\parallel}{2\zeta_\parallel} \frac{\omega k b^2}{1 + (\zeta_0 R_b)/(\zeta_\parallel L)} \tag{2.19}$$

where $\zeta_0$ is the resistance of the body. In case the flagellum is much longer than the radius of the spherical body, $L >> R_b$, we have that the drag and the propulsive forces increase by the same amount of length increase, leading to a speed that is independent of L for fixed k and b.

Another example, more close to the subject of this work is, is the propulsion mechanism of an *E. coli* bacteria, where its helix rotates. The helix, which is lying on the x-axis, has a radius R which is much smaller than the body's radius, hence the pitch angle $\alpha$ is very small. A motor creates the rotation of the helix, with rotation $\Omega_m$ relative with the body, while $\Omega$ is the angular speed of the helix and $\Omega_b$ is the counter-rotation of the body. The relation between the angular speeds is: $\Omega_b + \Omega = \Omega_m$. Using eq. 2.6, but considering only the components on the x-axis, for external force F and moment M, we have:

$$\begin{pmatrix} F \\ M \end{pmatrix} = \begin{pmatrix} A & B \\ B & C \end{pmatrix} \cdot \begin{pmatrix} U \\ \Omega \end{pmatrix}; \tag{2.20}$$

Looking only at the leading order in $\alpha$, for $L >> R_b, R$, the resistance coefficients can be computed approximately. The coefficient A has to be computed by considering a helix pulled at velocity U but not rotating ($A \approx \zeta_\parallel L$), vice versa C when the helix rotates with rotation $\Omega$ but is prevented from moving along the x axis ($C \approx \zeta_\perp R^2 L$). While B, since there is symmetry in the matrix, can be computed by looking either at the moment needed to avoid a translating helix to rotate or at the force to keep a rotating helix from being pulled in the x direction ($B \approx -(\zeta_\perp - \zeta_\parallel)\alpha RL$) [2], figure 2.5.

In order to calculate the swimming speed U, we start from the forces and moments acting on both the body and the flagellum. For a spherical body: $F = -\zeta_0 R_b U$ and $M = -\zeta_r R_b^3 \Omega_b$, with $\zeta_r = 8\pi$ being the rotational resistance [2]. The velocity U, and the rotations $\Omega$ and $\Omega_b$ are:

$$U \approx \alpha \frac{\zeta_\perp - \zeta_\parallel}{\zeta_\parallel} \left( \frac{\zeta_r}{\zeta_\perp} \right) \left( \frac{R_b^3}{RL} \right) \Omega_m; \tag{2.21}$$

$$\Omega_b = \Omega_m + \mathcal{O}(R_b/L); \qquad \Omega \approx \Omega_m (\zeta_r/\zeta_\perp) R_b^3/(R^2 L)$$

The velocity is linear in $\alpha$, so the handedness of the helix defines the direction of U. If in case of a planar wave there is no need of a body to have propulsion, eq. (2.19), but in case of a helix propulsion system, if $R_b = 0$, then $U = 0$.

### 2.1.5 Slender body theory

In the previous sections we looked at exponentially slender filaments, but in a real flagellum, the relation between the radius a and the typical length scale for shape deformations in the flagellum L, is $a/L \sim 10^{-2}$, and in the previous theories, $1/log(L/a)$ needs to be much smaller than 1.

In order to improve the model we take advantage of the slenderness of the filament so that the solution for the 3D filament surface dynamics can be replaced by the dynamics of the centerline described by an appropriate distribution of flow singularities [4]. Two different approaches can be used to find these solutions. Firstly, considering the solution as an extension of the local theory described previously, approximating as a series of logarithmically smaller terms [13, 14, 15]. In this case, the flow field close to the filament is locally two dimensional and it diverges logarithmically away from the filament (Stokes' paradox of 2D flows, [16]). On the other hand, a line distribution of stokeslets of unknown strengths describes the flow in the far field and diverges logarithmically near the filament.
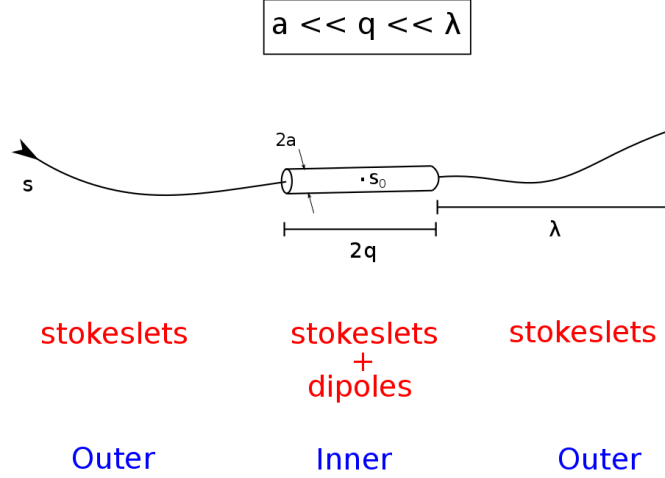
Figure 2.6: Lighthill model for the singularity construction of the flagellar hydrodynamic in the slender-body theory. The flow field at point $s_0$ on the rod is computed by combining the outer and inner problems stokeslets solutions, defined by the intermediate length scale q. The inner problem is represented by a distribution of both stokeslets and dipoles, while the outer problem only by a distribution of stokeslets. The final dipole strength is found imposing that the result should be independent of q, figure from [2].

This diversion is due to the line integration of stokeslets that in the near field go like $1/r$. Matching the two asymptotic behaviours it is possible to derive a series of terms of order $1/log(L/a)^n$ that give the stokelet strengths order by order. The leading order is the local drag theory value and gives a stokelet distribution proportional to the local velocity. The second order, is an integral equation of the shape and velocity of the filament. The consequent terms can be generated systematically [17, 18, 19].

This approach is an extension of the local drag theory described preciously in section 2.1.4. The major problem of this approach is that the expansion is made of terms $1/log(L/a)$ smaller than the previous, which leads to requiring a large number of terms in order to have an accurate description of the flow.

Another option is to solve at every instant an integral equation that is the derivation for the distribution of the singularities along the filament [20, 21, 22]. Alternatively, as done by Lighthill [12, 23], the solution is a line distribution of stokeslets and source dipoles and the dipole distribution's strength is proportional to the stokeslets one. Hence, looking at a location along the filament, $s_0$, which is a slender rod, it exists a length scale, q, at which $a << q << L$. At the location $s_0$, the flow field at the surface of the filament is the sum of two flows, the first one is the so called inner problem, which is the one deriving from the singularities within the distance q from $s_0$, and the second one is the outer problem, which comes from the singularities at a distance larger than $s_0$, (see figure 2.6). Consid-

ering $q >> a$, the source dipoles, decay faster than the stokeslets, the latter contribute almost uniquely on the outer problem flow field. While for the inner problem the flow is the sum of stokeslets and source dipoles, and it is possible to find that the complete solution is independent of q [2, 12, 23].

The dipole strength is proportional to the stokeslet one and the resulting velocity of the filament at $s = s_0$ is given by:

$$\mathbf{u}(s_0) = \frac{\mathbf{f}_\perp(s_0)}{4\pi\eta} + \int_{|\mathbf{r}_0 - \mathbf{r}| > \delta} \mathbf{G}(\mathbf{r}_0 - \mathbf{r}) \cdot \mathbf{f}(s) \, ds \tag{2.22}$$

with $\mathbf{f}$ is the local strength of the stokeslets distribution, G is the Oseen tenson, as in eq. (2.9), $\delta$ is the natural cutoff, from regularisation of the divergence due to self-interaction and $\mathbf{f}_\perp$ is the perpendicular projection to the filament of the stokeslets distribution.

This mathematical formulation is less accurate than other more rigorous solutions, but it is easily implemented numerically and hence used very often to model filaments in different environment, as for example near the boundaries [24, 25, 26, 27, 28].

## 2.2 Collective Motion

In nature, microswimmers are found swimming in semi-dilute and dense suspensions. In order to fully characterise the complex dynamical behaviour of collective motion, it is necessary to understand the underlying physical cooperative mechanisms on various levels: from the interactions between single cells and fluid-mediated interactions to the generic principles for the large-scale pattern formation.

### 2.2.1 Hydrodynamic interactions

There are three major types of hydrodynamic interactions that can be considered to study micro-organisms swimming in a viscous environment: cell to cell, cell to boundary and flagella interactions.

#### 2.2.1.1 Cell to cell

Naturally micro-organisms swim in a dense or semi-diluted environment, where the cells interact between each other more or less frequently depending on the concentration. Micro-swimmers can interact hydrodynamically with each other through the flow created by each swimmer, which can be felt by other nearby swimmers. These generated flows can, in certain situations, affect the dynamic, not only of a single swimmer, but of the entire population of swimmers present in the environment. One relevant example here is a sperm sample, they naturally swim in a dense, at times up to 6 billions cells per millilitre (ram),
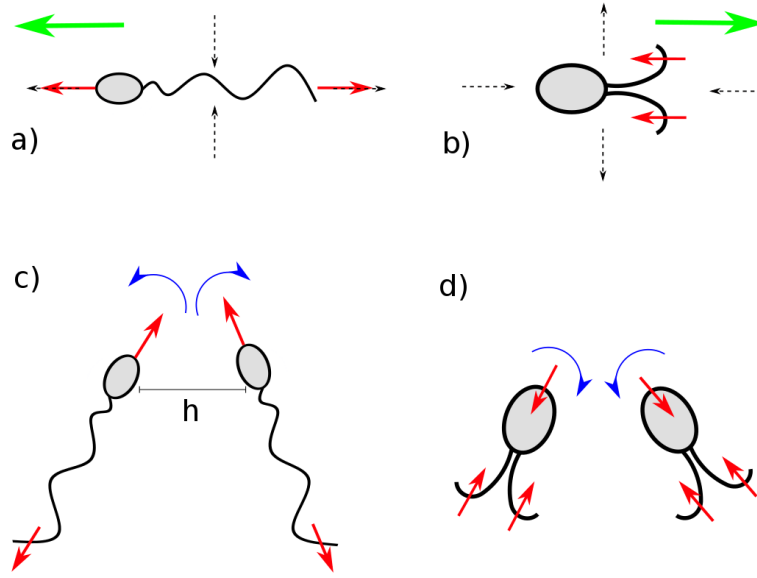
Figure 2.7: Interactions between two swimmers. The black dotted arrows in **a)** and **b)** define the flow field around the swimmer. The big arrow define the swimming direction, left for a pusher and right for the puller, while the red arrows show the direction of the stroke of the flagella. In figure **c)** and **d)** the interactions between the swimmers are displayed. Blue arrows show the direction of the reorientation after the interaction, figure from [2].

suspension and they show the so called spermulence [29], which is the parallel to bacterial turbulence [30, 31, 32, 33, 34, 35, 36]. Moreover sperm cells of the wood mouse swim faster when aggregated [37], while opossum spermatozoa create pairs in order to swim more efficiently in very viscous fluids [38] and for similar reasons the fishfly sperm cells cluster in dense bundles [39]. Finally, sperm cells in sea urchin, create very interesting structures composed of vortices that move in a liquid-like manner in the space [40].

Hence it is important to understand how the flow field created by a single swimmer can affect the motions of its neighbours. If we consider two cells and we look at how cell 1 reacts to the flow field created by cell 2, we obtain two hydrodynamical interactions: the first one is the velocity field created by cell 2 that carry cell 1 along its flow, the second is reorentational, cell 1 perceive the velocity gradient which tends to change the direction of swimming of cell 1.

The far field flow generated by a swimming cell, is a force dipole and hence decays as $1/r^2$. Two different types of force dipole can be accounted for, one is where the force dipole, **p**, oriented in the same direction as the swimming, is positive and the other is when it is negative. Pushers are swimmers with $p > 0$, like sperm cells and *E.coli*, and they draw fluid from the sides and push it in long axis direction (*e*). On the other hand, when $p < 0$, the swimmers draw fluid from the long axis direction and push it to the sides, these type of cells are called pullers and an example is the *Chlamydonomas* algae.

The dipole **p** = $p$**e** induces a flow at a distance **r** that is:

$$\mathbf{u}(\mathbf{r}) = \frac{p}{8\pi\eta r^3}[3\cos^2\theta - 1]\mathbf{r} \qquad (2.23)$$

where $\theta$ is the angle between $\mathbf{e}$ and $\mathbf{r}$. The dipole strength depends on the swimming speed of the cell, U, and its typical length scale, L, in such a way that: $|p| \sim \eta U L^2$.

When two cells are swimming in an aligned direction, $\theta = 0$, then the relative velocity scales as $\Delta u_{al} \sim p/\eta r^2$, while if they are side by side, $\theta = \pi/2$, we have that $\Delta u_{sbs} \sim -p/\eta r^2$. Both relative velocities depends on the force dipole sign, hence for $p > 0$, pushers, when side by side they attract each other, while when aligned they repel each other. Vice versa for pullers, $p < 0$, that repel each other when side by side and attract each other when aligned.

When one cell is affected by the velocity field gradient of a neighbouring cell, their direction changes, reorienting accordingly to the gradient. The vorticity field is defined as the curl of the velocity field, $\boldsymbol{\omega} = \nabla \times \mathbf{u}$, and interacting cells subject to this flow will rotate as: $\boldsymbol{\Omega} = \boldsymbol{\omega}/2$ if cells are spherical, otherwise an additional term, $E = 1/2[(\nabla\mathbf{u}) + (\nabla\mathbf{u})^T]$ has to be added to account for the symmetrical part of the rate of strain [41, 42].

As in the case of the velocity flow field, the vorticity flow field depends on the sign of p, leading to two different results for the reorientation in case of pushers or pullers, leading them to reorient towards their attractive configuration. Nearby pushers reorient side by side, while nearby pullers will end up aligned in the elongated direction [2], as shown in figure 2.7.

The hydrodynamical interactions described here are the leading order of cell to cell interaction, but in order to reach higher accuracy when modelling systems of many cells, higher order effects should be considered, the most important are the active component of the hydrodynamical interactions and the higher singularities for the dipole flow induced by a cell. In case of the active interactions, previously we have consider only what cell 1 feels from the flow field created by the other cell, but we never considered that the flow field of cell 1 will create a disturbance flow that will influence the velocity and the orientation of cell 2. This reflection interaction is weaker compared to the one describe previously and in space it decays faster. In the second case, we only looked at the cells as a dipole on the leading order, without considering the higher singularities like source dipoles and quadrupoles that have a faster decay, which can be important when computing correlations.

These cell to cell interactions play a strong role when we move away from the dilute regime and we have more dense suspensions, in which the cells organise and create very complex dynamics. Example are jet and swirls [43], or long wavelength waves [44, 45] and turbulence [32, 33].
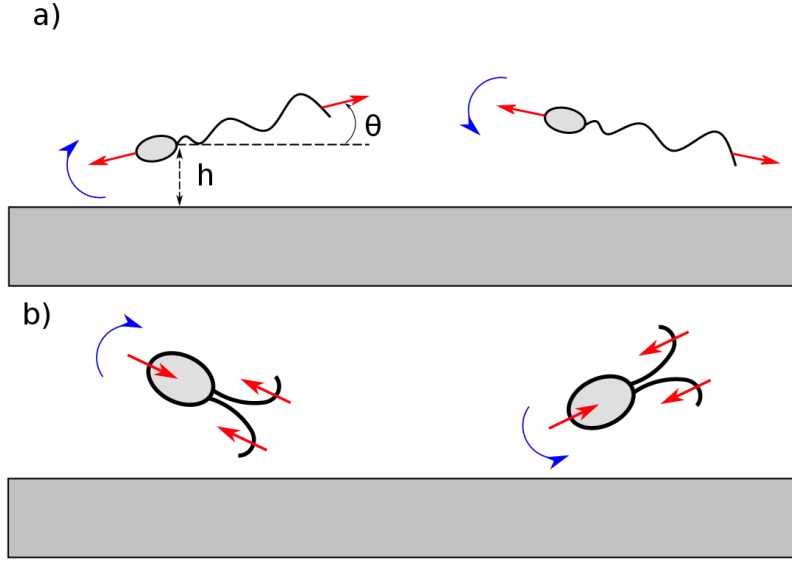
Figure 2.8: A swimming cell located at a distance h and angle $\theta$ from the boundary, will reorient. The rotation is dependent on the type of swimmer considered, for pushers **a)**, like sperm cells, the hydrodynamical interactions will reorient the swimmer in the direction parallel to the wall. For puller **b)**, like Chlamydomonas, the reorientation is perpendicular to the surface, figure from [2].

### 2.2.1.2 Cell to boundary

When cells swim they will have some interaction with the physical walls constraining them inside the physical environmen. The presence of confinement influences the motion of swimmers, modifies the concentration of chemicals that can influence motility and modify the hydrodynamic stresses that affect the motion of the cell [46]. Hence boundaries change the motion of cells, which swim differently at the wall or in the bulk. For example, sperm cells try to reach a vaginal wall and swim along it in order to arrive and fertilise the egg [29].

Boundaries modifies primarily four aspect of cell motion. First of all, boundary influences the cell velocity [47, 48, 49, 50, 51]. Intuitively a cell should slow down at a boundary since the wall increase the viscous drag, but since the swimmer method of propulsion is itself drag based, the result is not that straight forward. In order to simplify the matter, let's consider only a flagellum, without head, that beats as a planar wave, and as seen for eq. (2.19), the flagellum, for a given wave form, has a speed that increases with the ratio between parallel and perpendicular drag coefficients, which for their part, increase at the wall: $\zeta_\perp$ faster than $\zeta_\parallel$. For fixed waveforms, this unbalance in the increase leads to a ratio $\zeta_\perp/\zeta_\parallel$ that increases near a wall, meaning that the drag based propulsive force generated by the flagellum increases near a wall. Similarly the resistive drag on the swimmer increases near a wall, but this increase is weaker than the propulsion one, leading to an increase in the

speed of a swimmer near a wall. In this case when there is an increase in speed for a swimmer there is the need to increase the rate of work produced by the swimmer. On the other hand, if we assume that the swimmer swims with constant power, then the swimmer's speed will decrease near a boundary, leading, except in case of some specific wave forms [48, 49], to a decrease in the swimming efficiency.

In addition, boundaries can influence the cell trajectory. When *E.coli* cells swim near a surface, their trajectories transform from linear to circular [52, 53, 54, 55, 56]. Their propulsion is chiral and when the derived axisymmetric propulsive force is averaged, *E.coli* swims on a straight line while away from the wall. However, near a surface the time average axisymmetry is broken by the chiral propulsion itself, because interaction with a wall created non-zero components in the motility matrix. When the helix is parallel to the surface there is non-zero coupling between the helix rotation around its axis and the force perpendicular to the helix axis but parallel to the surface. A force which rotates opposite to the helix rotation, creates a net effect that produces a torque when the cell is at the wall, and since swimming bacteria are torque-free, the cell rotates in such a way that counter-balance the wall-induce torque.

Thirdly, when a cell swims near a wall, its bulk flow field does not satisfy the no-slip boundary condition and to model the interaction images on the other side of the wall are necessary. Hence the cell at a distance $h$ and angle $\theta$ from the wall, will be influenced by the image flow field and its gradient, leading to a rotation proportional to $\Omega \sim -p\theta/\eta h^3$ that is directed perpendicular to the body and parallel to the surface. Basically the cell is interacting with an mirror image of itself, allowing us to treat it similarly to a cell to cell interaction. As in the case of cell to cell interaction, if the swimmer is a pusher it will be attracted by the mirror cell and will then swim next to it, reorienting parallel to the surface [57, 58], see figure 2.8. The attractive speed is then scaling like: $u_\perp \sim p/\eta h^2$. On the other hand, a puller like swimmer will be reoriented perpendicularly to the surface and hence will swim away from it, but is the cells are confined they will always and continuously swim into a wall; while pusher like cells will just remain at the surface. Both methods though, lead to accumulation of cells at the boundary.

Finally, the cell to cell interactions can be potentially reduced by the presence of a wall. This can be explained considering the singularities of a flow field generated by a cell at a distance $h$ from the surface. Its mirror image flow field can potentially cancel the singularities at the far field. Hence the overall flow at distance grater than $h$ from the wall can be weaker than it would be if the cell was away from the wall.

#### 2.2.1.2.1 Sperm hydrodynamics near surfaces

The sperm cells need to swim in the female tract in order to arrive at the egg, hence they naturally move in a confined environment, that at times can be extremely tortuous and full of obstacles [59, 60]. Many works tackled the problem of sperm swimming at a surface for different species [61, 62, 63, 64, 65, 66, 67, 68, 69]. The main observation is that sperm cells have a curvilinear or circular trajectory when swimming close to a surface. The analysis of the trajectories at a surface is important when we consider that the swimming strategy of sperm cells is to move sliding over a surface, when reach it. In the work from Bukatin et al. [70], asymmetries in the curvature of the midpiece of spermatozoa tail have been noticed, which affect strongly the swimming trajectory of the cells, giving a curvature right or left to the trajectories of the swimming sperm cells [71, 72], as shown in figure 2.9 a). Many possible reasons for the midpiece curvature can be assumed. The combination of the rotation of the planar beating in a step-wise way and the midpiece curvature lead to a reorientation through right or left turning of cells when faced with reversing flow.

Many works have tried to analyse and explain the behaviour of sperm cells near a surface [71, 72, 74, 61, 75, 64, 68]. In general, the pusher like cells should reorient parallel to the surface and the motion can be studied through numerical simulations of the Navier-Stokes equations [76, 77] or mesoscale simulations can help understanding the attraction and motion at a wall [71, 74]. In this last case, the flow field around a sperm cells is dipolar in the bulk, but when close to a wall it becomes asymmetric. Given the presence of the wall on one side, the flux coming in the midpiece is from only the bulk direction and it results stronger than the one for a single cell in bulk [78]. The midpiece is then attracted to the surface by this asymmetry in the surrounding flow field, on the other hand the end part of the tail has a flow component that repels the tail from the wall, lifting the terminal piece of the tail. This creates a tilt in the sperm axis direction that turns the sperm cell towards the wall, enhancing the wall attraction [71, 72, 78]. Experimental work [73], in agreement with the theoretical one, shows the sliding motion of sperm cells over a wall, with tail lift and head against a wall, allowing the estimation of the sperm cells minimum turning radius, see figure 2.9 b) B and C. If the cell is long $l$, oriented at the point of the head, tangentially to the surface, the radius of curvature of the trajectory $R$ can be found from observations as [73]:

$$\frac{\delta}{l} \approx \frac{l/2}{R}; \quad \rightarrow \quad R \approx \frac{l}{2\delta}l \tag{2.24}$$

with $\delta$ being the radius of the conical envelope of the beating pattern. From the experimental results $R \sim 150\mu m$ for a human spermatozoon.

Experimentally [73], when these sliding sperm cells then reach a corner, they do not follow it but if it is a concave sharp corner, they mostly do not escape and get trapped in the
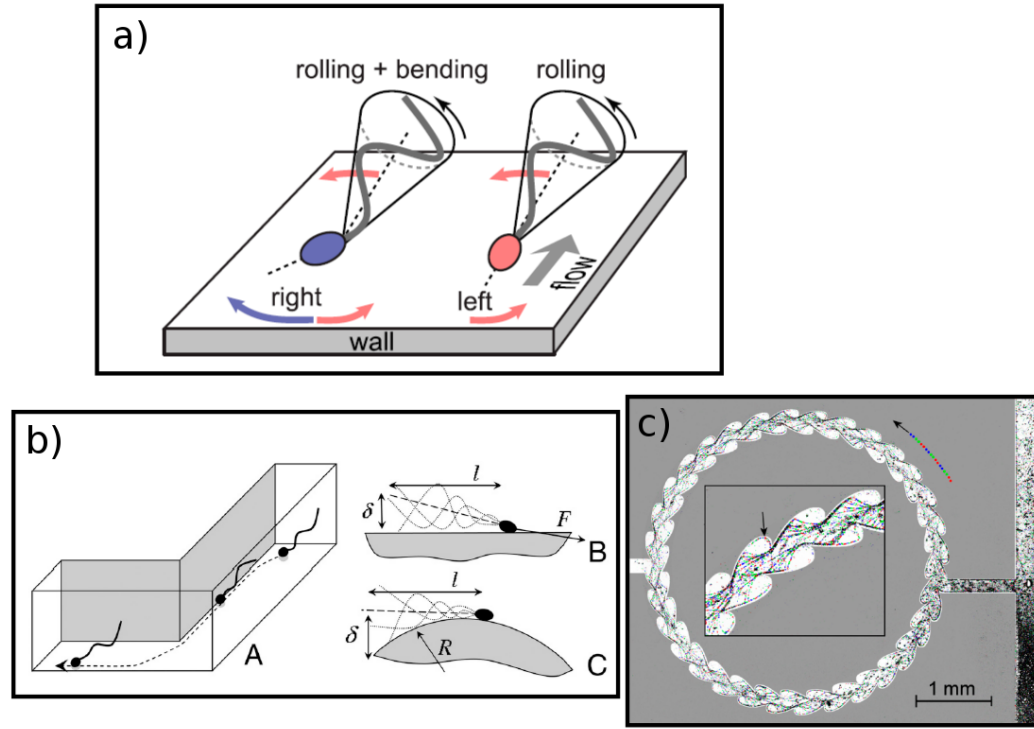
Figure 2.9: **a)** Shows the turning mechanism extrapolated by [70], where the both left (red) and righ (blue) turning cells roll, in the conical envelope, the flagellum counter-clockwise. This leads to a torque turning to the left, but since the blue cells (right turning) have a tilted head, the torque is counteracted by an opposing force that is larger, leading to right turn direction of motion for the cell. **b)-A** Shows the behaviour of a sperm cell at a hard corner. The cell swims against the wall but when the corner is reached, it departs from the wall and swims forward until another boundary is found. **b)-B** Schematic description of the technique of a sperm cell moving head against the wall at a boundary. **b)-C** Shows the schematic representation for the estimation of the minimum turning radius, as described by [73]. Finally, **c)** shows how the swimming strategy for sperm cells can be used to create microfluidic devices to direct the flow of spermatozoa in a desired direction. In this ansotropic "one way running track" as defined by the authors [73], the cells swim counter-clockwise and in the insert it is possible to notice that cells swimming in the opposite directions are redirected towards the counter-clockwise flow only by feature proper of the channel.

corner, but when the convex curvature is approached they leave the wall and continue swimming following the direction their head pointed at, until they reach the next wall and resume to slide on it, as shown in figure 2.9 b) A. This methodology of swimming can be used to direct sperm cells' motion with a specific pattern of the microchannel. With "clover-leaf" structures it is possible to guide the cells and redirect the one that try to swim upstream, see figure 2.9 c), creating a unidirectional flux of sperm cells towards a point. This technique has been used in this work to concentrate cells in desired locations, like pools where experiments were carried out.

Figure 2.10: Schematic of the hydrodynamical interactions between two sperm flagella. Two nearby sperm cells with a different phase in their beating motion will, after some time, phase lock and coordinate their beating, figure from [2].

### 2.2.1.3 Flagella interactions

The final interaction we take into account is the one between flagella. We will focus on eukaryotic flagella, like sperm cells, and cilia. It has been seen [39, 79, 80, 81] that two sperm cells swimming nearby will, after a transient time, beat in phase. To explain this phenomenon we can consider, in a first simplified way, two swimmers similar to two Taylor sheet swimming with the same prescribed waveform. In this case for the two swimmers it will be more energetically convenient to swim in phase and the more their phase are different the more energy they will dissipate. Thus, at the beginning, when the two swimmers have different phase, their velocity are different too, but their phase difference evolves in such a way that after a transient they will be either perfectly in phase with $\phi = 0$ or out of phase $\phi = \pi$. In simulations both configurations are stable and theoretical work suggested that the waveform asymmetry in between front and back of the flagellum is responsible for the phase locking [79, 80].

If we now look at real eukaryotic cells their flagellar waveform is not fixed, but its form is the result of the balance between internal force from the molecular motors, the elastic and viscoelastic resistance from the flagellar structure and the viscous resistance of the external fluid. This delicate balance is disrupted by the presence of a second swimmer nearby that changes the forces in the surrounding fluid, consequently changing the shape of the flagellum of the first cell. These changes induced by the neighbouring cells are responsible for the phase locking [81].

In a recent work [82], where a system of multiple sperm cells has been modelled, it was found that there is a tendency to aggregate in clusters where the flagella are aligned.

The majority of the studies about phase locking is concerning cilia, when they are highly packed they behave in such a way that their shape changes in a coordinated manner with just a very small phase difference, creating the so called metachronal waves that propagates along the surface covered by cilia [83, 84, 85].

Many theoretical studies [27, 26, 25, 86, 87, 88, 89] in the years have tried to model and explain the flagellar coordination, here we would briefly mention two approaches used.

Firstly, a very accurate model for ciliar beating can be created, trying to model the correct internal forces of the axoneme and the resistances [26]. When the beating mechanism is modelled, two cilia are placed near and it has been seen that after two beating cycles they will be in phase[26]. While the propagating wave arises when multiple cilia are placed on a surface. In the both cases it is energetically more convenient for cilia to beat in phase or, as for a large number of them, with a very small phase difference [27]. The second approach, simplifies the model for the ciliar beating, but concentrating on the conditions necessary to have phase locking. For example considering the cilia arranged into a lattice where their movement depends on a balance between the rotation induced by the other cilia in the lattice and Brownian motion, the cilia, after a short time will create a coordinated beating pattern that will create itself a net flow [86, 87, 88, 89].

### 2.2.2 Microscale collective motion

As already mentioned, microswimmers in nature are found in semi-dilute or dense solutions.

The most commonly experimentally studied organism for microscale collective motion is bacteria. Even though these systems consist in many interacting micro-organisms their macroscopic behaviour is non trivial. Many theoretical and experimental works try to understand them [90, 91, 92, 93, 94, 95, 96, 97, 98].

When high concentration of bacteria are present either swarming on an agar plate or swimming in a fluid, they create fascinating patterns and show turbulent motion. Simple models [98] of self-propelled particles have been proposed to explain the intermediate range hydrodynamics, while more complex one [99], which take into account further biological details, can capture the more complicated behaviours.

Large scale orientational coherence has been seen in *B.Subtilis* [33], which is called zooming bionematics, and resemble the molecular alignment shown by nematic liquid crystals. In this phase the cells swim in clusters in the fluid, with speed larger than the single cell velocity.

Coordinated motion is not only used by bacteria, but in recent studies [39, 100, 101, 102, 103, 104] it has been seen that spermatozoa exploit collective motion to increase significantly their own motility, create pattern and cooperate efficiently in confinement.

After looking at single interactions between cells, their flagella and between cells and walls, it is time to analyse a system of collective particles, as one of self-propelled rods.

#### 2.2.2.1 Bacterial collective motion

Looking at a system of self-propelled particles, a simple physical interaction as volume exclusion of the rod-like microswimmers will lead to alignment. In this case two main types

of interactions have to be distinguished: firstly the polar interactions, where the alignment is in the swimming direction and nematic interactions, where alignment is independent from the direction of motion.

In a 2D system of self-propelled particles that can cross each other, the rods are modelled as linear chains of overlapping beads [105, 106, 107]. In these type of systems, self-propulsion leads to enhanced aggregation and formation of clusters [105, 106, 108, 107, 109, 110, 111]

Comparing simulation results for system of self-propelled rods, with simulations and analytical calculations for Vicsek model [93] and continuum hydrodynamical models, it is possible to notice that for Viscek and continuum models the polar and nematic interactions have to be distinguished: polar interactions lead to moving density waves [112, 113], while for nematic interactions high-density bands with rods moving parallel to the band itself but moving in bot directions have been predicted [114].

In these types of simulations, given the nature of the rods representation by a chain of beads, the nematic interactions are the dominant contribution, while the polar component is present but not as significant [105]. This means that there is a larger probability for parallel alignment than antiparallel after rods collisions.

Simulations of self-propelled rods without noise, show very interesting phase diagram as function of aspect ratio of rods, a, and volume fraction, $\phi$ [108]. In this phase diagram six major motion states have been found as shown in figure 2.11.

For small volume fractions, it is possible to observe a dilute phase for the entire range of aspect ratios. With increasing volume fraction, several phases of densely packed rods arise. Their internal structures differ and depend on the aspect ratio. With increasing aspect ratio it is possible to distinguish: a jammed phase for very short rods and intermedaite to high volume fractions, a turbulent phase for intermediate rods and high volume fractions, local nematic alignment and swarming phase for intermediate to large rods and intermediate volume fractions and finally a laning phase for very long rods and high volume fractions.

In the dilute state, little or no cooperative motion is seen, but with increasing volume fraction of very short rods, the mean square displacement of the moving particles drops of nearly two orders of magnitude along the transition curve from dilute to jammed phase. On the other hand, very long rods at intermediate volume fraction exhibit swarming behaviour with large spatiotemporal density fluctuations. The very long rods, with further increase in volume fraction there is a transition from swarming to laning, characterised by a discontinuous increase of the correlation length for the spatial velocity correlation function. The laning phase exhibit assembles of rods in homogeneous lanes.

The bionematic phase, characterised by the coexistence of vortices and jet-like structures, exhibit large fluctuations in the local vortex density and, in the phase diagram, is the phase
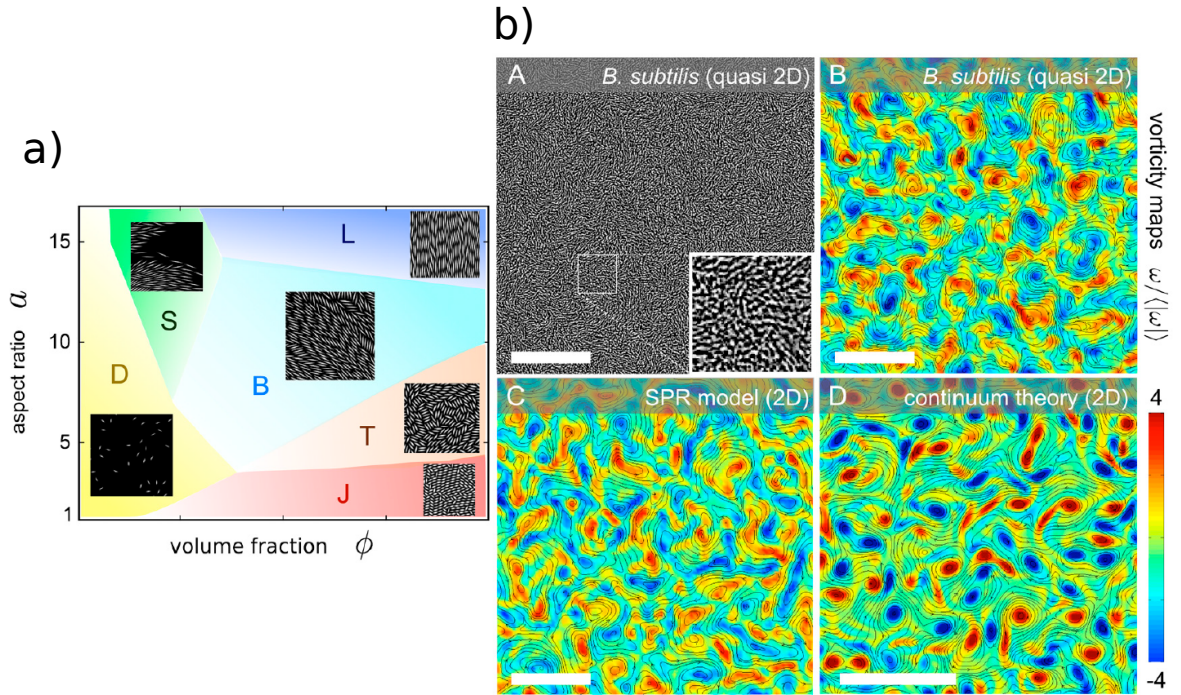
Figure 2.11: **a)** Schematic of a non-equilibirum phase diagram for the self-propleed particle model. Varying the aspect ratio of the particles and their volume fraction it is possible to distinguish six different phases: dilute state D, jammed state J, swarming state S, laning state L, bionematic phase B and turbulent phase T. **b)** Firstly, **A** is the experimental snapshot of aquasi-2D bacterial suspension with high volume fraction, then there are 3 schematics of vorticity fields with flow stream lines, for the turbulent phase: **B** is for the quasi-2D bacterial experiment, **C** from the simulations of the self-propelled particles with aspect ratio a=5 and volume fraction $\phi = 0.84$ and finally **D** for the continuum theory. In this latter case, the range of the simulation was adapted to the experimental field of view by matching the typical vortex size. All the scale bars are 50 $\mu$m. Figures from [108]

adjacent to both swarming and laning phases.

However, the most important and interesting phase predicted by this model is the homogeneous turbulent state, that arise for intermediate aspect ratios and high volume fractions. The aspect ratio for which the turbulent phase appears is the typical aspect ration of the most commonly used bacteria for experimental studies. At high volume fractions, with decreasing aspect ratio there is a transition between the bionematic and the turbulent phase, that is characterised by velocity distribution, correlation function and density fluctuations. Indeed, the velocity distribution for the bionematic phase is broad and non-Gaussian, but it is shown to be Gaussian in the center for the turbulent phase, as shown in figure 2.12 A. Additionally, the velocity correlation function for the bionematic phase smoothly decreases, its oscillations even out given the presence of bionematic jets as dis-
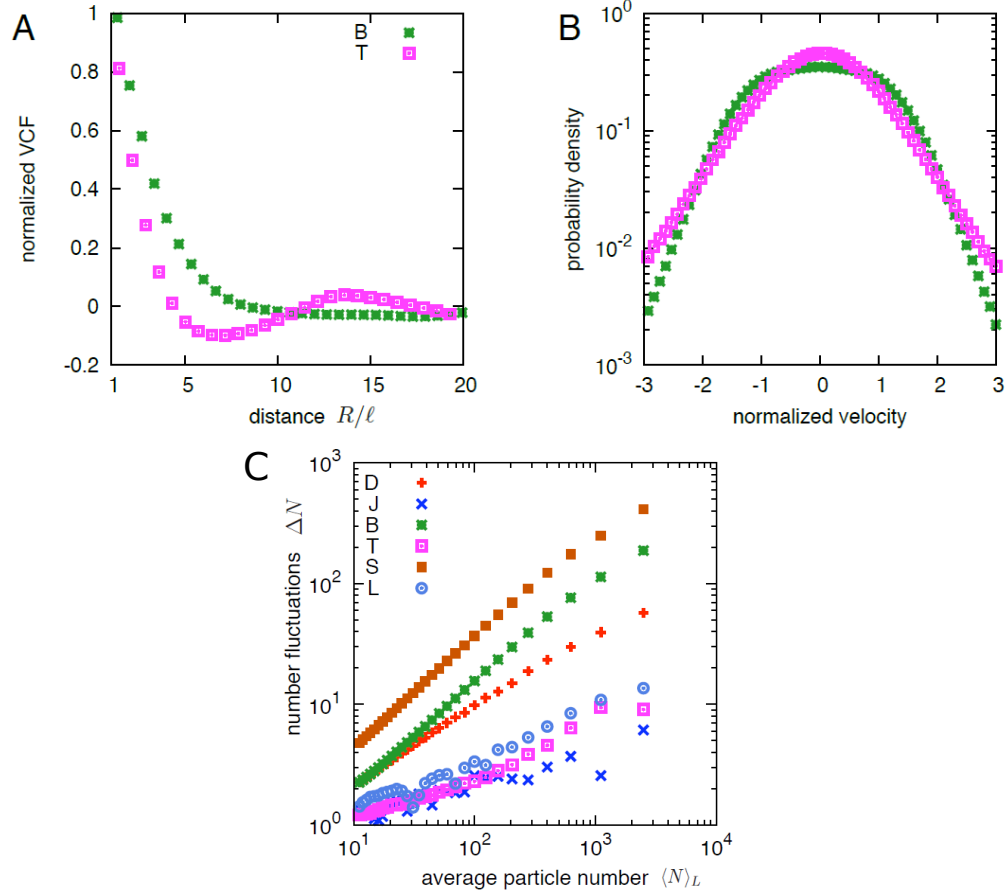
Figure 2.12: Comparison between different phases. **A** shows the velocity correlation functions (VCFs), where the distance R is normalised by the bacterial length *l*. The correlation function for the bionematic phase decreases smoothly, while for the turbulent phase a negative minimum is found and characterise the typical vortex size $R_v$. **B** shows the distribution of Cartesian velocity component for both the bionematic phase with a=9 and $\phi$=0.55 and turbulent phase, with aspect ratio is a=5 and volume fraction $\phi = 0.84$. The distribution for the turbulent phase is approximately Gaussian with exponential tails, while the bionematic phase has a broadened distribution that is not Gaussian. **C** shows the typical number fluctuations as a function of the average particle number for the different states. The power-law scaling reveals big number fluctuations for the swarming and bionematic phases, while the fluctuations result strongly suppressed in the dense jamming, turbulent and laning phases. Figures from [108].

cussed in [115], but the velocity correlation function of the turbulent phase shows a minimum that represents the typical vortex size $R_v$ (figure 2.12 B), that in 2D is around three times the bacteria length $L$. Finally, the number of fluctuations are less stronger in the turbulent phase than in the bionematic one, see figure 2.12 C.

The turbulent phase is characterised by typical random swirls and and vortices in the velocity fields, which are characteristic of turbulence at high Reynolds number. This phase has been observed in both surfaces and 3D bulk suspension of *B.Subtilis* [108, 33, 35, 116,

117] and studied in theoretical and simulation works [118, 108, 119, 36].

In order to compare the microswimmer turbulent phase with the high Reynolds number turbulence the energy power spectrum $E(k)$ can be calculated, where $k$ is the wave vector, which correlate to the Fourier transform of the spatial velocity correlation function. Looking at the behaviour of $E(k)$ in the classical turbulence we have that it is predicted to scale in 3D as $E(k) \sim k^{-5/3}$, called Kolmogorov-Kraichnan scaling [120], while in 2D, there are an energy-inertial upward cascade which goes as $E(k) \sim k^{-5/3}$ and an enstrophy transfer downward cascade decaying as $E(k) \sim k^{-3}$. Now, considering the 2D bacterial turbulence two different regimes have been found: for small $k$, the energy spectrum decays as $E(k) \sim k^{5/3}$, while for large $k$, the decay was $E(k) \sim k^{-8/3}$ [108]. Thus, self-sustained bacterial turbulence at small scales has some properties in common with classical turbulence, but it differs from it at large scales [108].

#### 2.2.2.2  Sperm cells collective motion

In recent years the topic of spematozoa turbulence, or spermulence, has gained interest. Indeed, some experimental studies [101, 102, 100, 40, 39, 121] have been carried on, showing interesting swarming behaviours of high concentration sperm cell system, as the trains of woodmouse sperm [100, 101] or the arrangement in vortices of sea urchin sperm [40].

As mentioned in section 2.2.1.3, flagella interactions would lead to beating synchronisation. When two spermatozoa swimming at a distance smaller than one sperm length, it is necessary to take into account the full hydrodynamic interactions between the two time-dependent flagellar shapes. The beating of the flagella influence each other and that typically leads to phase locking, for example synchronising their beating pattern [122]. This hydrodynamical interaction between sperm flagella has two effects: a synchronisation at short time scales and for longer times an attraction [122]. The two sperm cells swimming close to each other will synchronise their beating with a time dependent on the initial phase difference, for example for a phase difference of $\frac{1}{2}\pi$ the synchronisation will appear after two beating, while they will synchronise after about 5 beatings for a $\pi$ phase difference [122]. A difference in swimming velocities will adjust the relative position of the two spermatozoa and when the beats of flagella will be in phase, the velocities will rapidly transition and become identical.

Experimentally both synchronisation and attraction of sperm cells have been observed [121, 122] and for example, when the sperm heads are strongly coupled mechanically then the flagella beat in synchrony [121].

Collective behaviour of sperm cells at a finite concentration have been studied mainly numerically [122], where a mesoscale simulation was performed for a 2D system with a density of about three spermatozoa per square sperm length. The beating frequencies $\omega$

are selected from a Gaussian distribution with variance $\delta_f = \langle (\Delta\omega)^2 \rangle^{1/2} / \langle \omega \rangle$. The frequencies are not chosen equal for every simulated sperm cells since in nature not all the sperm beat at the same frequency.

Changing the width $\delta_f$ of the Gaussian frequency distribution, the simulated system react differently. For variance $\delta_f = 0$ when a cluster is formed, unless there is a strong external force acting on it, like a head to head cluster collision, it will not disintegrate. For $\delta_f > 0$ there are different beat frequencies and the phase difference between a cells and other cells in the cluster increases in time, hence cells manage to leave the cluster only after a sufficiently long time frame. Moreover, there is a balance between formation and break-up of clusters and the cluster size can grow by both merging with other clusters or collecting cells in its path. The average cluster size depends on $\delta_f$, being larger for small variance values than for large $\delta_f$.

Cluster size for $\delta_f = 0$ will continue to grow in time, without reaching a minimum, while for $\delta_f > 0$, the cluster size remain stationary after 50 beats. If we look how the average cluster size depends on the variance $\delta_f$ of the frequency distribution, we notice that it decays exponentially as [122]: $\langle n_c \rangle \sim \delta_f^{-\gamma}$, where $\gamma = 0.20 \pm 0.01$. Indication that the cluster size diverges for $\delta_f \to 0$ is given by the negative exponent.

On the other hand, experimental work on sperm turbulence has been performed in the recent times [103], where the fresh undiluted ram semen has been confined in a glass chamber of a centimetre by a centimetre in size with a variable height h = 100,150,200 $\mu$m. Whirlpool structures have been seen in the system, as shown in figure 2.13 **a)** and **b)**, which are clusters of cells that result forced by hydrodynamic interaction into local alignment. From the derived flow fields, it results that there is a linear relation between energy and entrophy of the system and their ration will give the integral length scale $L^* = (E/\Omega)^{1/2}$ (figure 2.13 **c)**). From the experimental data, the whirlpools are detected separately and their length scale $l^*$ is calculated using the major axis of the ellipses contouring the whirlpool itself. This length scale results to be similar to the integral length scale calculated through the velocity fields. Furthermore, using a two point correlation function, it has been seen that the integral length scale $L^*$ defines the typical correlation length independently from the initial energy of the system.

The Fourier analysis is the used to analyse the internal length scale of the velocity field from the swimmer size $a$ to the integral length scale $L^*$. The resulting energy spectrum, shown in figure 2.13 **d)**, is divided into three regimes. The first one, for small wavelengths $k$, shows a saturation to a white noise plateau. Here the largest vortex reaches the size of the integral scale $L^*$, up to a critical wavelength $k_c = 2\pi L^*$, where the the velocity fluctuations are uncorrelated in space and form a random set of coherent structures. The second regime is above the critical wavelength $k_c$, where there is a clear power law decay of the power spectrum as $k^{-3}$, which is very similar to the power spectra decay found for quasi-
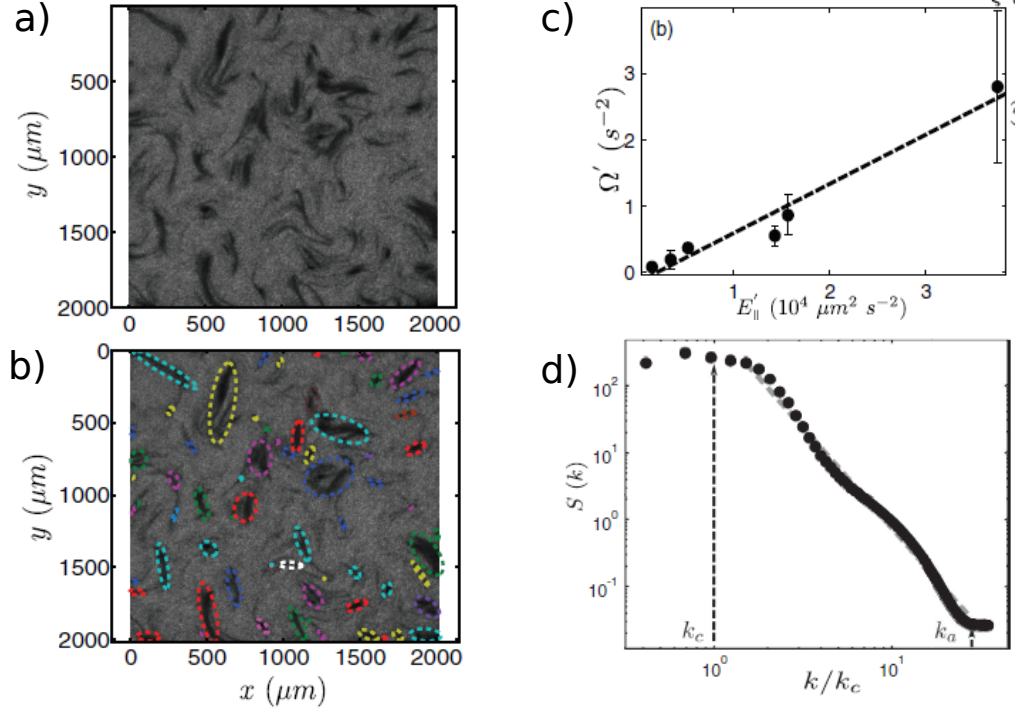
Figure 2.13: Spermulence plots. **a)** shows the phase-contrast microscope images of fresh semen placed between two glass plates separated by 150 $\mu$m. **b)** shows the whirlpool detection, segmentation, and ellipse extraction. **c)** represents the 2D fluctuating kinetic energy $E$ plotted versus the fluctuating enstrophy $\Omega$ for six different experiments for the 100 $\mu$m chamber. The error bars are calculated from the enstrophy standard deviation and the dotted line shows the linear trend associated with a constant ratio between energy and entrophy, the square root of which provides the integral length $L^*$. Finally, **d)** shows the fluctuating energy spectrum plotted versus the modulus of the wavelength $k$ rescaled by a critical wavelength $k_c = 2\pi L^*$, for six different experiments in the 100 $\mu$m chamber. The spectrum displays three regimes: between $k_c$ and $k_a$ the motion is well correlated and presents the $k^{-3}$ power law represented by the gray dotted line, $k > k_a$ which, at the individual scale, defines the uncorrelated noise and $k < k_c$ where there are large scale coherent but uncorrelated structures. Figures from [103].

2D turbulent flows. The final and third region is for large wavelength $k > k_a = 2\pi/a$, where the power spectrum saturates, showing again a white noise regime consistent with the size of the single swimmers. These three regions suggest that the velocity correlations build up from the individual swimmer scale $a$ to a large collective scale $L^*$. Dilution of the samples affects mostly the smaller scales leading to a decrease of velocity correlations and to a lower energy, while for larger scales the flow is mainly unaffected by the dilution, showing the whirlpool structures.

Finally, the height of the channel doesn't seem to influence drastically this system, which is hence considered fairly robust representation of a quasi-2D system, where multiple layers of sperm cells are present, showing a behaviour close to bacterial turbulence.
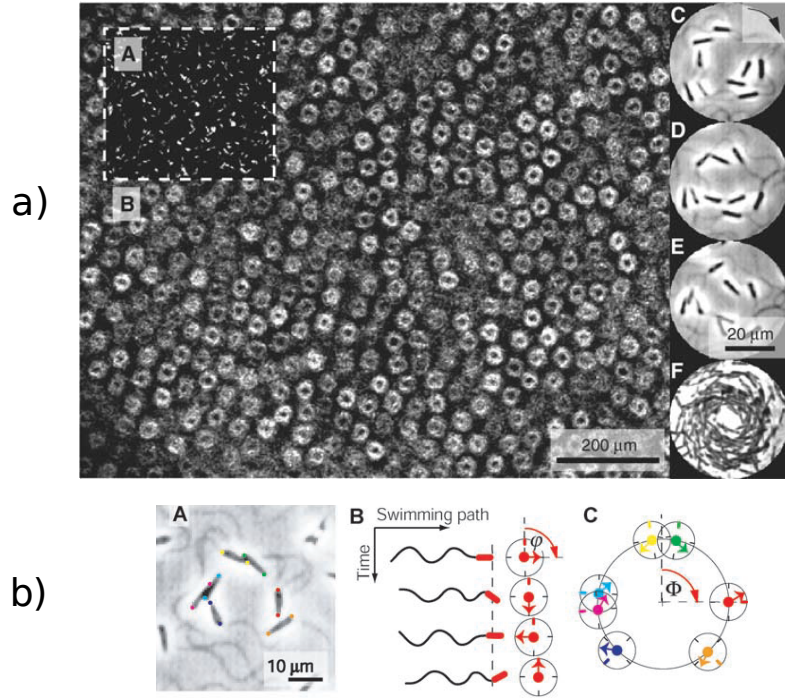
Figure 2.14: Spermatozoa swimming in vortices and the consequent hexagonal configuration of the vortices in 2D with a surface density of 6000 cells/ mm$^2$. **a)** Shows the hexagonal configuration of the vortices where **(A)** is the dark field-contrast image showing only the heads of the swimming cells; **(B)** shows an arrangement of vortices thanks to the average intensity of 25 consecutive frames; **(C to E)** are successive frames of nine spermatozoa swimming in a vortex, the arrow showing the direction of rotation, in this case clockwise; **(F)** Another 25 frames average showing a magnified view of the vortices. While **b)** shows the hydrodynamical coupling of sperm cells in a single vortex that leads to quantized rotating waves. **(A)** shows both the position an the orientation of seven sperm heads, labelled with coloured dots, present in a single vortex; **(B)** the circling pointers represent the different phases of the oscillation of the sperm's head. Finally, **(C)** shows the projection of the angular postion of the heads within the vortex onto a unit circle. Figures from [40].

We intend to report another interesting phenomenon that appears for a 2D system of concentrated sea urchin sperm cells [40]. When sperm density at the surface increases over 2000 cells/mm$^2$, the cells arrange into vortices, composed of several spermatozoa swimming in a vortex of diameter around 25 $\mu$m. On average 10 cells would swim in each vortex, circling clockwise around a common center. The vortices themselves organise in a fluid structure with local hexagonal order, see figure 2.14. The onset of this structure formation correspond to the the density at which, there is overlap density of circular trajectories, hence increasing the surface density increases the number of cells in each vortex.

In the experimental work [40], the sperm "trapped" inside the vortices have been noticed to have a peculiar form of beating pattern synchronisation. If every spermatozoon is defined by two variables: firstly, the phase of the oscillation its head, which, since it is driven

by the flagella oscillation, has its same frequency and secondly the angular position of the head while the sperm cells swims in the vortex. Both variables have been seen to not correlate is calculated between any two spermatozoa belonging to the same vortex, but their difference do correlate. Hence spermatozoa in the same vortex have different frequencies and velocities, but if for example a spermatozoon swims twice as fast, it will even beat twice as frequently. This implies that two sperm cells in the same vortex, although they swim with different frequency and velocity, they are locally beating in synchrony, with a trailing sperm cells following the leading one.

Moreover, given that the swimming path of the sperm cells is circular, only an integral number of wavelength exist. Hence it is possible to calculate the wave numbers in two ways: firstly by the ratio between head phase oscillation and head angular position and then by the ratio between vortex circumference and average beating frequency of sperm cells in the vortex. Both ways give a wave number around 4. This leads to the result that hydrodynamical coupling of the tail of sperm cells swimming inside the vortex give a quantized rotating wave with wave number around 4 [40].

A simulation of this 2D system have been recently performed by Yang et al. [123], where the sperm cells' flagella are confined in a surface plane and the flagella interactions are only excluded volume interactions and hydrodynamics is accounted through resistive-force theory or 2D mesoscale hydrodynamics approach, average simulated trajectories are shown in figure 2.15.

In both experimental work [40] and simulation [123], the correlation function $G_{f,c}(r)$ of the instantaneous center of the circular trajectories and the variance $\Delta$ of the spatial distribution of the centers have been calculated [40, 123]. Simulations with and without hydrodynamical interactions show that there is a weaker correlation for systems with the interactions. This is due to the fact that hydrodynamical interactions, as mentioned before in this section, lead to synchronisations and attraction of sperm cells, but they also disrupt the path of the sperm cells swimming in the opposite direction in the neighbouring vortices. Additionally, since the simulation results agree reasonably with the experimental data only when anisotropic friction is considered, it is possible to conclude [74] that the hydrodynamical interactions, in a 2D system, play a minor role in the process of vortex creation. Still no simulation has been carried for a 3D system where the hydrodynamical interactions would be stronger than in the 2D system. Finally, again in both simulation and experimental work [123, 40], it has been seen that the order parameter increases linearly with increasing surface cell density. This means that the characteristic vortex size does not vary, but with increasing number of sperm cells swimming inside the vortex, the vortex mass increases.
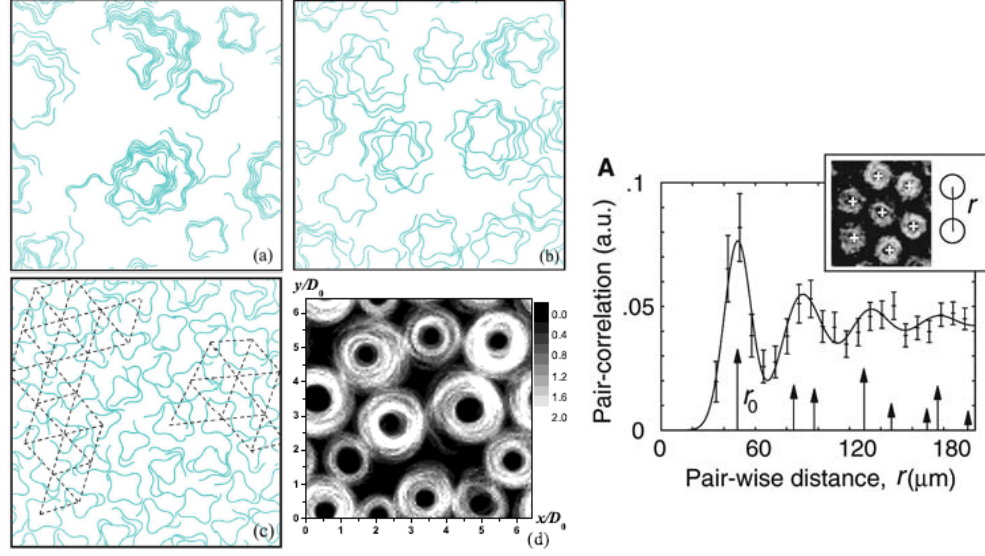
Figure 2.15: Snapshots of a simulated 2D system of flagella, that self-organise into vortices. **(a)** is the snapshot for flagella in a mesoscopic fluid; **(b)** case of anisotropic friction. **(c)** shows the system with anisotropic friction and lower surface density, where the dashed lines show the local hexagonal order. **(d)** is the average over 30 flagellar beats in the same system as **(b)**. Images from [123]. Finally, **A** shows the pair-wise correlation function of the vortex centers, while the insert demonstrate how the function was calculated. In order to compare to an ideal hexagonal lattice the arrows are used to show the positions and relative weights of the maxima for the ideal hexagonal lattice. Plot from [40].

### 2.2.3 Vicsek model

Collective motion of not only microswimmers but even of macro systems, like flocks of birds and schools of fish [124, 125, 92], can be modelled with a minimal model called Vicsek model [93, 92], where the moving bodies adjust their motion thanks to interactions with the neighbouring bodies, favouring alignment.

The Vicsek model was introduced by Tomas Vicsek at al. in 1995 [93, 92], and is a mathematical and physical method that tries to describe in a minimal way how cells interact, changing their direction of motion depending on the nearest neighbours.

Viscek at al. demonstrated that even considering just a very basic system of particles moving and interacting between each other it is possible to capture the generic collective properties of various systems of self-propelled particles. This simple model considers a number N of point particles that at $t = 0$ are randomly distributed and contained in a square of size L with periodic boundary conditions, each particle moves continuously in the plane,

they all have the same absolute velocity $v$ and their direction $\theta$ at time $t = 0$ is randomly distributed.

The system evolves following one simple rule: a given particle swimming at a constant absolute velocity, at each time step, will assume the average direction of motion of its neighbouring particles in a radius $r$ around it, plus some random perturbation [93] (see figure 2.16, **(e)**).

Let's consider N polar point particles randomly distributed in space, contained in a square of size L with periodic boundary conditions and moving with constant magnitude velocity $v_0$. In this system, every time step $\Delta t$, which for simplicity we consider equal to one, the particles update their velocity direction with the average direction of motion of their neighbouring particles. The dynamics of the position $\mathbf{r}_i$ of particle i, evolves as:

$$\mathbf{x}_i(t+1) = \mathbf{x}_i(t) + \mathbf{v}_i(t)\Delta t \tag{2.25}$$

The velocity $\mathbf{v}_i$ of the particle i at time $(t+1)$, is defined by the constant absolute velocity $v_0$, and the evolution of the angle $\theta$ between $\mathbf{v}_i$ and the x axis of the Cartesian coordinate system. The angle $\theta$ evolves with time as:

$$\theta(t+1) = \langle \theta(t) \rangle + \Delta\theta \tag{2.26}$$

where $\langle \theta(t) \rangle_r$ is the average direction of all the particle within the circle defined by the interacting radius $r$, including particle i, with center in particle i.

In eq. 2.26, $\Delta\theta$ is a random number picked from a uniform probability distribution between $[-\eta/2, \eta/2]$, where in this case $\eta$ is the noise intensity. $\Delta\theta$, can be considered akin to a temperature-like variable.

In this system there are three free parameters: the noise $\eta$, the density $\rho = N/L^2$ and the distance covered by a particle between two updates. The latter can be chosen such that the particles manage to interact with the neighbours and move fast enough that the system configuration changes after a few updates. The two extremes $v \to 0$ and $v \to \infty$ give respectively no particle movement at all and mean field behaviour, where in between updates the particles are fully mixed.

When the system starts at $t = 0$ the positions and the directions are randomly distributed in the space, as in figure 2.16 **(a)**, now looking at the evolving system for low densities and noise, figure 2.16 **(b)**, we see that after some time, groups of particles move in a coherently in a random direction. On the other hand, if both density and noise are high, figure 2.16 **(c)**, the motion is random but with some correlation. Finally, if the density is high and the noise is low, figure 2.16 **(d)**, the system shows ordered motion at a macroscopic scale, where particle move in the same selected direction.

The absolute average normalised velocity $v_a$ can be used as a order parameter and it is
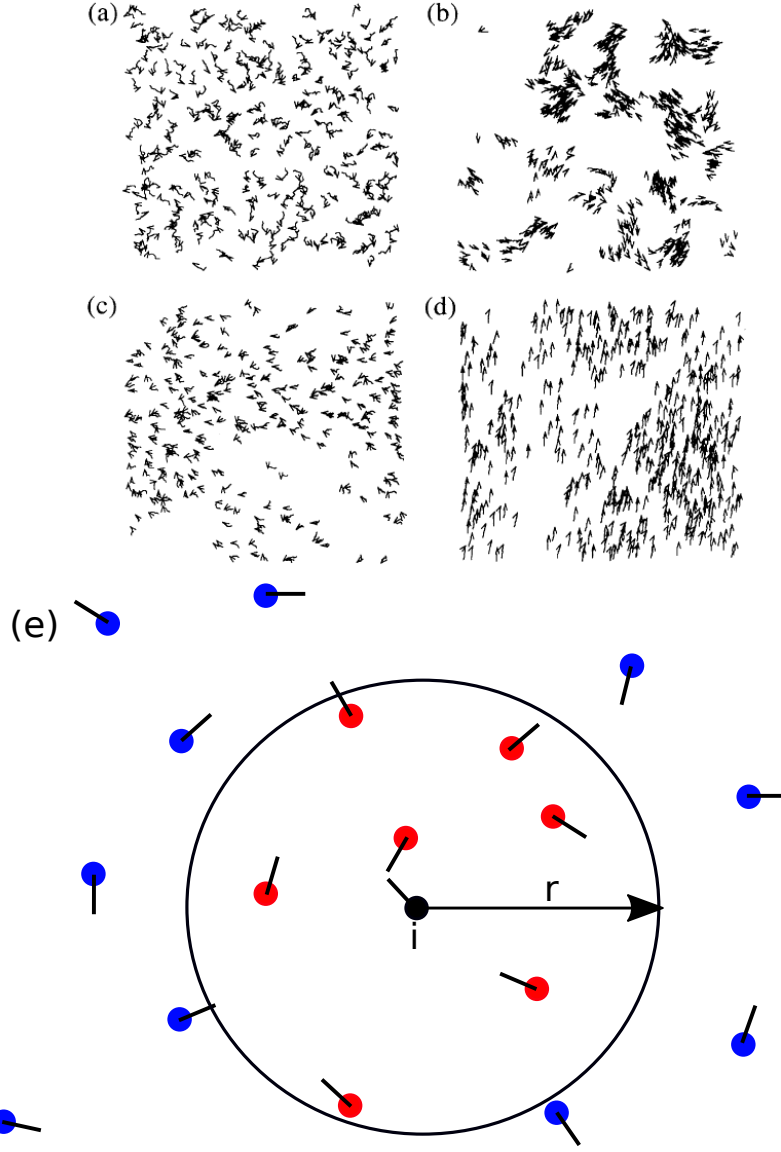
Figure 2.16: Velocity fields for a system of 300 self-propelled particles. **(a)** is the system at t=0, $\rho = 6.12$, $\eta = 2.0$, showing the initial conditions of the system. **(b)** is the evolved system, t 0, at low density $\rho = 0.48$ and low noise $\eta = 0.1$; **(c)** again an evolved system for high density $\rho = 6.12$ and high noise $\eta = 2.0$ while **(d)** is the evolved system for high density $\rho = 6.12$ and low noise $\eta = 0.1$, where a polar ordered phase arises. **(a)** to **(d)** are taken from [93]. Finally, **(e)** is the schematic of the set up of the alignment rule for the Vicsek model. The i-th particle reorients due to the influence of the particles present in the circle of radius r around itself. The red particles are the one that result in the circle at time t, the blue one are the external one and the black one is the reference particle i.

defined as:

$$v_a = \frac{1}{Nv} \left| \sum_{i=1}^{N} \mathbf{v}_i \right|.$$
(2.27)

As an order parameter, if each particle has a random direction, $v_a$ has a value equal or near

zero, while it grows to 1 if the particles are moving in a coherent way.

Variations in the values of noise and density create changes in the average normalised velocity $v_a$, as shown in figure 2.17 **(a)** and **(b)**, and in thermodynamic limit, where the system has a phase transition similar to a system in equilibrium, we can show that:

$$v_a \sim (\eta_c(\rho) - \eta)^\beta, \qquad v_a \sim (\rho - \rho_c(\eta))^\delta \qquad (2.28)$$

with $\beta$ and $\delta$ being the critical exponents and $\eta_c(\rho)$ and $\rho_c(\eta)$ being the critical values of noise and density for $L \to \infty$. For finite size system, the values of critical noise and density depend on the system size L. Dependency for fixed noise or density of the order parameter on $\eta$ and $\rho$ could be plotted, shown in figure 2.17 **(c)** and **(d)**.

Thus, this simple model shows the emergence of collective motion through a continuous transition. Many studies investigated the nature of this transition [126, 127, 128, 129, 130, 131, 132, 133, 134, 135, 136].

There are many possible variations of this model and the results depend mostly on the type of local interaction rules used for the alignment and on the chosen parameters of the system.

We will proceed to briefly describe three variations of this model: without or with alignment rule and the mean-field approaches.

### 2.2.3.1 Models without alignment rule

In many real systems, there is no explicit alignment rule [92, 137, 138, 139, 140, 141, 142] and nevertheless an ordered phase arises. We can model those system considering that the alignment is introduced with an interaction rule during collisions between particles. The simplest model states that particles, confined in a 2D system, try to maintain their absolute velocity and they are subject to repulsive force **F** when they are close. The repulsive force is the only interaction.

Hence the equations describing the evolution of the system is:

$$\frac{d\mathbf{v}_i}{dt} = \mathbf{v}_i \left( \frac{v}{|\mathbf{v}_i|} - 1 \right) + \mathbf{F}_i + \zeta_i \qquad (2.29)$$

where $\zeta_i$ is the white noise, and the only interaction between particles is through the pairwise central force $\mathbf{F}_i$.

In simulations of this minimal model, the system goes from disordered phase to coherent motion through a first order type of transition [143].

Other variations of this model or different boundary condition lead to a variety of results, showing for example ordered migration or vortex formation or subgroups moving in a chaotic way. In the considered model, when the isotropic particles collide inelastically,
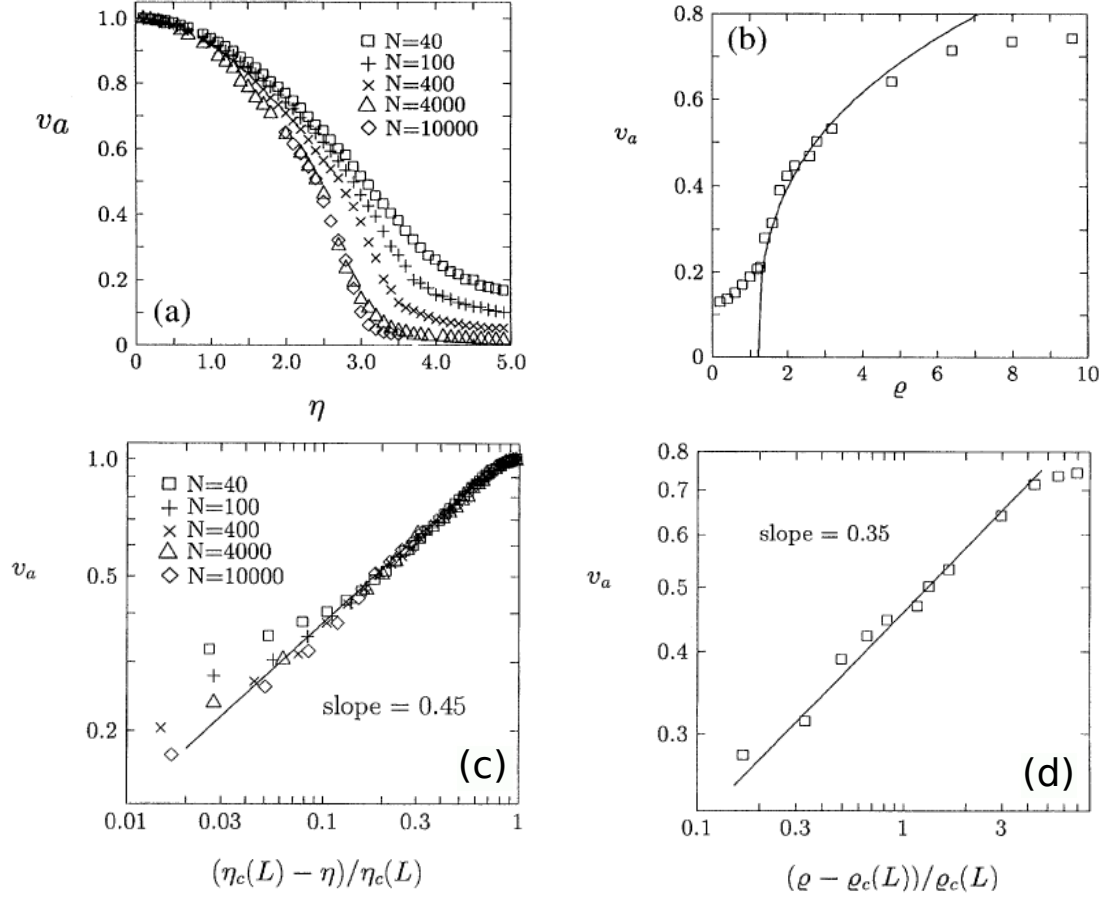
Figure 2.17: Variation of the vortex parameter $v_a$ depending on noise and density. **(a)** shows the order parameter for variation of noise keeping the density constant, $\rho = 4$; **(b)** is the order parameter for constant noise, $\eta = 2.0$, and varying density. Determination of the critial exponent through the behaviour of the critial variables: **(c)** shows the plot of the order parameter vs $ln[(\eta_c(L)-\eta)/\eta_c(L)]$ for different system sizes but constant density $\rho = 4$. **(d)** similarly shows the order parameter as function of the $ln[(\rho - \rho_c(L))/\rho_c(L)]$ for a fixed value of noise $\eta = 2$. All pictures taken from [93].

inducing alignment and leading to an increase of the overall velocity correlation that results in coherent collective motion in the system [144].

If the interactions considered are attractive instead of repulsive, many different patterns arise, like swarming, undirect mills and aligned groups moving coherently [145]. This attractive system is stable only when in the presence of noise.

Bacteria and other biological micro-organisms are asymmetric and can be modelled by rod-like particles moving in 2D with constant speed. They would interact through nematic collisions [140] and with the presence of noise. Nematic collisions are a specific type of collisions, where if the included angle between two rod-like particles entering collision

36

is smaller than 180°, then after collision, the two particles will align and continue their motion in the same direction in parallel. On the other hand, if the angle between the particles before collision was bigger than 180°, then after collision, they will travel in parallel, but moving in opposite directions. With these conditions the system shows a phase diagram divided in four parts: the first is spatially homogeneous and ordered, the second is similar to the first but has regions at low density that show a disordered phase, the third phase is similar to the previous one, but in this case the bands where the motion is disordered are not stable as in phase 2, but are thinner and more unstable. The segregation regions appear and reform, they separate and merge, displaying space-time chaos. Finally, the fourth phase is fully disordered, both locally and globally, it is chaotic in time and space, being homogeneous in space.

### 2.2.3.2 Models with alignment rule

The original model by Viscek already includes an alignment rule, but instead of considering the interaction radius *r*, we can look at a particle interacting with the *n* nearest neighbours. If the radius of interaction is changed it can lead to including the same amount of interacting neighbours, leading to a strict correlation between the metric and topological approaches. Even if at a first glance they can look equivalent, there is a very subtle difference that leads to a difference in the transition order. In the metric case the density can be prescribed, hence in the range of interaction the number of particles can vary. Ginelli and Chanté, [146, 147, 126], obtain a second order phase transition for the topological approach and a first order transition for the metric one.

It can be seen that the metric approach for low velocities gives a continuous transition that is similar to the topological approach, while becomes of first order with increasing velocities [136, 148].

### 2.2.3.3 Continuous media and mean-field approaches

A model considering a continuous media approach is quickly described here, where collective motion arises and it is possible to give a macroscopic description of a self-propelled particle system. The intention is to write hydrodynamic equations that allow to explain the macroscopic behaviour using general continuum equations for the particle motion. The final large scale behaviour depends mostly on symmetry terms and conservation laws. Toner and Tu [149, 150, 151], starting from a previous work [152], were the first one to describe a full non-linear higher dimensional dynamics, where they derived a continuum description, considering the most general equations of motion using velocity fields and density.

A single active self-propelled particle can be modelled as in figure 2.18 [153]. A swimmer
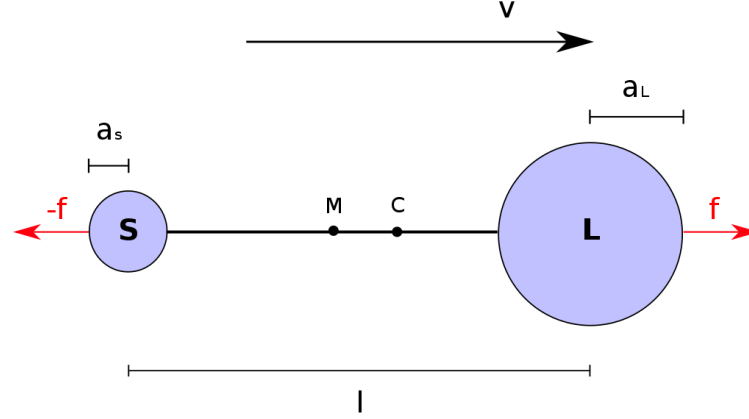
Figure 2.18: Simplified physical model of a self-propelled particle, described as asymmetrical rigid dumb bell.

is considered as a asymmetric dumbbell of length $l$ and orientation the unit vector $\boldsymbol{n}$. It creates on the fluid a force dipole. These swimmers are the one we looked at in the previous part of this chapter and can be pushers or pullers. Their velocity is $\mathbf{v}_p = v_0\mathbf{n}$ and the dynamics of a single particle $\alpha$ is described by the dynamic of the two spheres composing the swimmer (L and S) separately. The flow velocity at point $\mathbf{r}$ is $\mathbf{u}(\mathbf{r})$ and can be determined by solving the Stokes equation where both the active forces that the swimmer $\alpha$ exert on the fluid and the effect of the fluid fluctuations are accounted for [153, 154].

Mean field theories [155, 156, 137] for self-propelled particles can treat the system as a ferromagnetic or nematic system. Both approaches lead to a continuous phase transition with 1/2 exponent for the order parameter scaling [156]. The difference between these two mean field approximations is that the amplitude of the critical noise at which there is orientational order is lower when the cells alignment is nematic, instead it is higher for ferromagnetic-like systems [156, 155, 157].

It's possible to model the bacteria collective behaviour using a simple Vicsek model of rod-like particles with mean field approximation and periodic boundary conditions [98], it is possible through simulations to show that a rotational motion which is correlated in case of low noise and high density, in addition the directionality of the vortices present in the fluid are selected by symmetry breaking and are equally probable to appear, without a privileged rotation.

Looking at real bacterial systems, the hydrodynamical effects of the medium over the motion of cells are important and the regions with highly concentrated cells show a transient phase with patterns that are jet-like and they then evolve into vortices, which are stable

and the persistence time is around 1 second [116, 158]. The velocity measured in these collective patterns, jets and vortices, results to be higher than the velocity of the single bacteria. To explain this, a two-phase model [36] has been developed, where the bacteria and fluid are modelled as two independent but interpenetrating continuum phases.

## 2.3   Biology of Sperm Cells

After an overview on the Physics used to describe and model microswimmers system similar to the one we want to investigate in this work, we will proceed to describe as concisely as possible the morphology and the biology of the swimmer used in this work: the spermatozoon. We will look at the general anatomy of the mammalian spermatozoon and then trying to connect the biological composition of the sperm tail and its chemical interactions to its strategy of motion.

### 2.3.1   The Sperm Cell

Antonie Van Leeuwenhoek discovered in 1677 [159, 160], not only the "little animacules" living in the water, but also some little humans. At the time it was commonly believed that each sperm cell contained a little already formed human being.

The spermatozoon is an haploid cell that swims through the female tract and fertilises the female gamete, creating a new life. The spermatozoon is the carrier of the chromosome defining the sex of the foetus.

The size of a spermatozoa varies depending on the species [161], it could be as small as the hippopotamus sperm cell ($\sim 35\mu$m) or as long as the Chinese hamster which reaches $260\mu$m in length. Human spermatozoon is between 50 and $60\mu$m, similar to the ram and bull sperm cells which on average are $50-55\mu m$.

The spermatozoon can be divided into two major part: the head and the tail [162, 163, 164, 165, 166], see figure 2.21 .

#### 2.3.1.1   The Head

The head shape varies depending on the species, the majority of the mammals have a spherical or ellipsoidal head, while the rodents have a hook shaped head, but it is important to notice that even if shape and size of the head changes across species, the basic composition does not change at all, allowing us to have an accurate description of the spermatozoa itself.

The exterior of the head is divided into three major parts: the acrosomal cap, the postacrosomal region and the neck. The head contains the nucleus, which carries the DNA in the form or densely packed chromatin coil, see figure 2.19.

During spermatogenesis, the nucleus starts assuming its shape while disulfide bonds stabilise the chromatin and condense it, allowing it to be metabolically inert and highly resistant to digestion, this rigid shell is called perinuclar teca. These characteristics ensure that the chromatin can make it through the penetration of the zona pallucida of the egg, giving the spermatozoon the possibility to fulfil its purpose of fecundating the egg.

The condensed chromatin it is usually situated in the anterior half of the nucleus, the spermatogenesis process is a very precise one, the resulting spermatozoa are extremely uniform, with little abnormalities in both shape of the head and development [162]. The exception of this rule is the human spermatozoon, which has the higher percentage of irregularities in mammals [163]. Most importantly human sperm cells often have cavities in the condensed chromatin, which modify the head shape, this suggest that the condensation of chromatin in humans does not come to completion for all the sperm population in the same ejaculate [162, 165, 166, 163].

A very important part of the spermatozoon head is the acrosomal cap. This part of the external part of the head the one that penetrates the egg and dissolving its membrane, allowing the nucleus to enter the egg and fertilise it. The acrosome covers the majority of the head and its composed of multiple parts as shown in figure 2.21.

Looking from the outside towards the inside of the head, it is possible to distinguish the outer acrosomal membrane, right under the cell membrane. It continues till the bottom part of the cap, where it merges with the inner acrosomal membrane. In the cavity between the two membranes, there is the low electron density acrosomal content. The apical segment of the acrosome is often thick and in a specific shape dependent on the species, in case of rodents for example, this segment is very large. These parts compose the principal segment of the acrosomal cap, which covers the majority of the nucleus. Under the principal segment, there is the equatorial segment, where the inner and outer membranes fuse and there is a reduction in the thickness of the acrosome. Depending on the different species, the length of this segment changes, for example in boar sperm cells this segment is particularly long. The equatorial part of the acrosome is the only one that does not disintegrate during the acrosomal reaction with the egg during fertilization [162, 163, 164, 165, 166].

When the sperm cell arrives near the egg inside the fallopian tubes, in order to be able to fecundate the egg, it has to undergo capacitation where physical modifications occur. Bicarbonate ions enter the sperm cell and trigger capacitation, activating the soluble adenylyl cyclase enzyme in the cytosol which has been seen to correlate to different changes in the cell. First of all the plasma membrane of the spermatozoa loses the seminal plasma proteins and the glycoprotein coating and the membrane potential is hyperpolarised. Then the pathways for the acrosome reaction get activated, the flagellar motility increases to help penetration of the egg and more metabolic changes happen

[167, 168, 163].

Specifically, the apical and principal segment of the acrosome fuses with the external cell membrane in multiple sites, creating different openings for the acrosomal content to get released. This process of membrane fusion continues until the outer acrosomal membrane and the cell membrane are completely gone and the sperm nucleus is protected only by the inner acrosomal membrane. The content of the acrosome is rich of hydrolytic enzymes that allow the spermatozoon to penetrate the zona pallucida, helped by the beating of the spermatozoon that is enhanced and directed forward. Then it attaches to the oocyte plasma membrane, thanks to a transmembrane protein and then the genetic content enters the egg it fertilising it [167, 168, 163].

Behind the posterior part of the acrosomal cap, there is a region called postacrosmal region, which remains intact after the acrosme reaction. The plasma membrane in this region has a trilaminar appearance which lays over a thin dense layer called postacrosomal sheath. Between the sheath and the nucleus there is a narrow opening that closes by the posterior ring. Under the posterior ring, a portion of the nuclear envelope lies on the implantation fossa, which is the site where the tail attaches to the head. Specifically, this part of the nuclear envelope is covered by a thick layer of dense material called basal plate. The basal plate lined the fossa and allow a large number of fine filaments to attach to the head and they anchor the fossa and the connecting piece[162, 163, 164, 165, 166].

#### 2.3.1.2 The Tail

#### 2.3.1.2.1 The connecting piece

The connecting piece, as the name suggests, is the part of the sperm tail that connects the flagellum to the sperm head, see figure 2.20. The capitulum is the part that lies just underneath the implantation fossa, conforming in shape with the basal plate and attaching to it thanks to thin filaments, that are probably dissolved when the tail gets detached from the head during fertilisation. The capitulum is mainly composed of proteins and the bottom part of it appears to be associated with the segmented structures in the connecting piece. Looking at the connecting piece from the capitulum downwards we have a thin and continuous density area that caps the segmented structures that then separate into the nine segmented columns long one or two microns, which overlap in their caudal part with the nine outer dense fibers. The segmented columns of the connecting piece are composed of alternating bands.

In the connecting piece can be distinguished three parts:

- Left part: it expands into a large segmented area that is the origin of the outer dense fibers number four to seven.
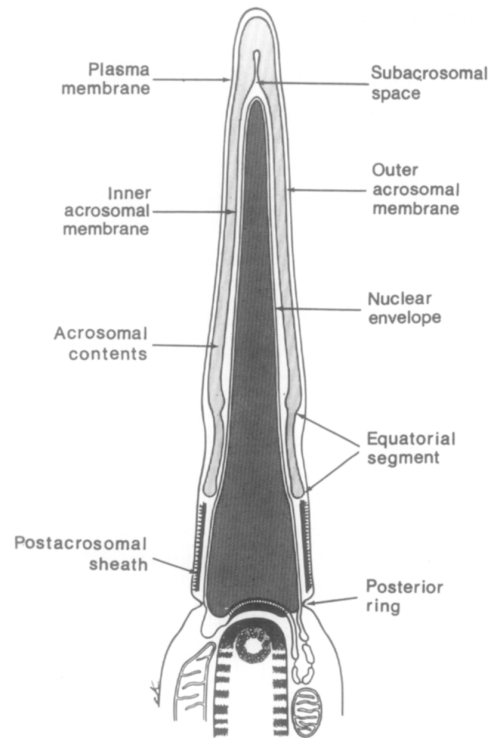
Figure 2.19: Drawing of the principal components a primate sperm head seen in a sagittal section. The junction between the head and the neck is marked by the posterior ring. Figure adapted from [162].

- Right part: the top of segmented columns in this part are folded, forming the proximal centriole vault. In addition, these columns are the origin of a set of three outer dense fibers, namely the fibers nine, one and two.

- Central part: this is where the distal centriole is during maturation of the spermatozoon. The two remaining outer dense fibers start from here (number three and eight).

The proximal centriole is a in a niche obliquely oriented in the dense part of the connecting piece under the capitulum. This centriole is the only one that survives the maturation of the spermatozoon. In fact, the distal centriole during growth of the sperm cell, is attached to the base of the axoneme, and during the development of the connecting piece it disintegrates, but at times the remnants of the nine triplets of microtubules can be found in the mature sperm cells.
The neck region does not really have organelles apart from one or two mitochondria that are oriented longitudinally and connect with the mitochondrial sheet of the middle piece [162, 163, 164, 165, 166].

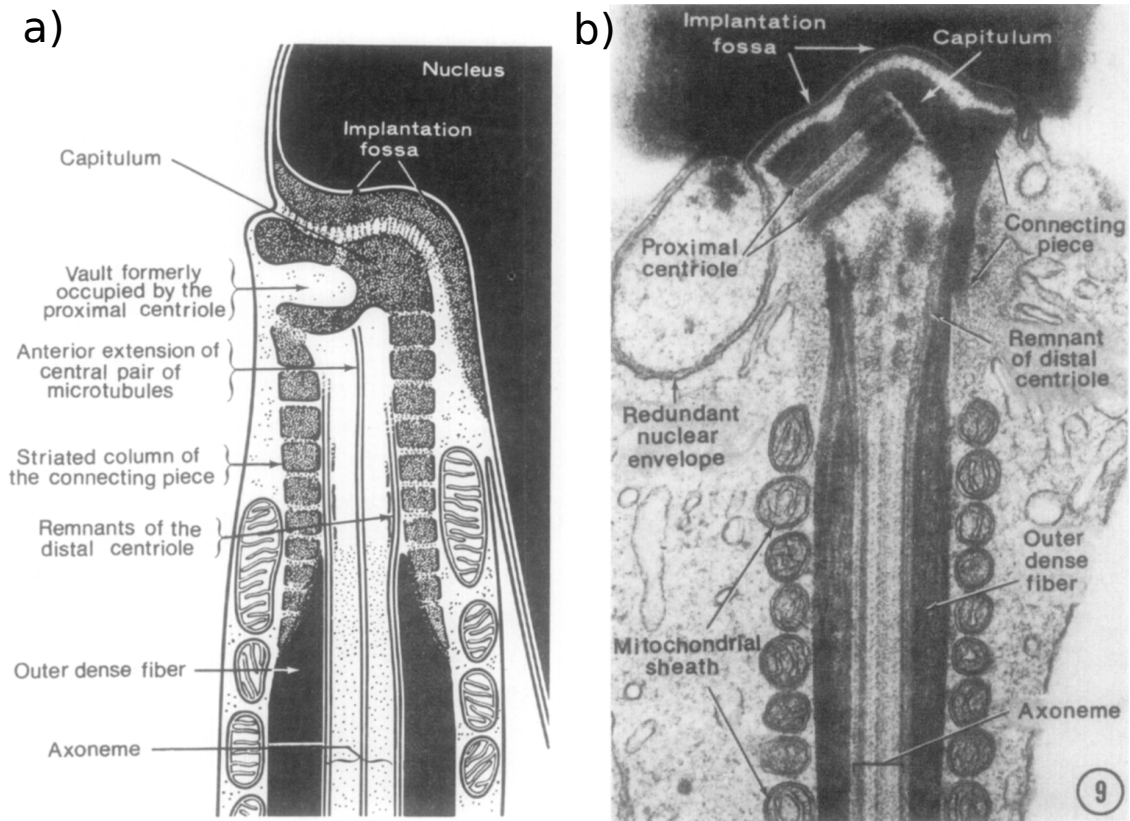Figure 2.20: Both **a)** and **b)** show the composition of the connecting piece between the head and the tail of the spermatozoa. **b)** is the image EM image of the neck part of a boar spermatozoon. Figure adapted from [162].

#### 2.3.1.2.2 The axoneme

The axoneme is the central part of the flagellum and it is its motor apparatus. It is composed by two central microtubules surrounded by nine of equally spaced doublets of microtubules arranged concentrically around the central pair, known as the 9+2 structure, as shown in figure 2.21.

Each doublet is composed by two subunits. The subunit A is a complete microtubules, with a circular cross section of diameter equal of around 26 nm. The subunit A cylinder consist in 13 protofilaments made by tubulin protein in dimers, which are associated end-to-end. The other subunit (subunit B) is not a full circular cylinder, but it is a C-shaped tube and attached to subunit A. It is composed of 10 protofilaments. Each subunit A has a two diverging nexin bridges connecting it with the subunit B of the adjacent doublet. Two arms, inner and outer arms, elongate from the the subunit A and the dynein motors present on the arms engage with the subunit B of the adjacent pair, exerting a sliding force between doublets that leads to a bend in the flagellum. The dynein is a protein with ATPase activity. In addition to the arms, every subunit A has a radial link that connect them to the central pair through the helical sheet that covers it. The center tubules are made of two

subunits A, which are joined by cross-bridges equally spaced in the tubules length and a sheath is wrapped around them [162, 163, 164, 165, 166].

### 2.3.1.2.3    The outer dense fibers

The outer dense fibers surround the axoneme creating a 9+9+2 structure. This structure is present in the internally fertilizing mammalians, while for marine species that fertilize in seawater, the fibers attached to the 9+2 structure is missing (figure 2.21).

The outer dense fibers come from the segmented columns in the connecting piece and they stretch for all the tail length, running parallel to the respective 9 doublets of the axoneme. Each fiber has a different size, shape and cross-section. Three of the nine fibers, number 1,5,6, are usually larger. The termination of the outer dense fibers is species dependent, but at their distal point each one of them is attached to the corresponding doublet.

Two sets of doublets (9,1,2 and 4-7) drive the alternating phases of the sliding to provide bending of the tail and hence movement of the sperm cell. The outer dense fibers are characterised by different density, creating a structure that limit the ability of the fibers to move with respect to each other. The outer fibers reinforce the structure and regulate the movement of the axoneme in the midpiece and principal piece of the sperm tail.

The other pair of outer dense fibers (3 and 8) are positioned parallel to the insider pair of microtubules, defining the plane microtubules plane. In addition, they control relative motion, restricting the bending of the tail within the plane defined by the head orientation. These two fibers terminates at the midpiece.

The mechanism to create the flagellar beating pattern by the sliding forced induced by the dynein motors coupled with the flagellum structure has been studied extensively mostly through modelling and simulations [169, 170, 171, 172, 173, 174, 175, 176, 177, 178, 179, 180, 181, 182, 183, 184, 185, 186, 187]. The most noteworthy of all for mammalian sperm is Lindemann's bull sperm model [181], where he describes the importance of the outer dense fibers for the mechanics of the flagellum beating.

### 2.3.1.2.4    The mitochondrial and fibrous sheath

The mitochondria in the sperm cell is arranged end-to-end in the midpiece, creating an helical structure that surrounds the outer dense fibers, see figure 2.21 c) and f).

The fibrous sheath is located in the principal piece of the spermatozoon and it is specific of mammalian cells. It run from the caudal limit of the midpiece (the annulus) until the end of the principal piece. It consists of two longitudinal columns connected by horizontal ribs. The initial part of the sheath is fixed to the outer dense fibers number 3 and 8, but these fibers then end with the end of the midpiece, while the other seven fibers continue

down the principal piece of the tail. The longitudinal columns of the fibrous sheath, after the termination of fiber 3 and 8, have the middle and inner part of the column itself becoming a thin edge that extend in the position of the two finished fibers.

Running down the principal piece of the tail, both the longitudinal columns and the ribs becomes slender, reducing the diameter of the tail. Finally, reaching the proximal part of the end piece, the fibrous sheath ends abruptly.
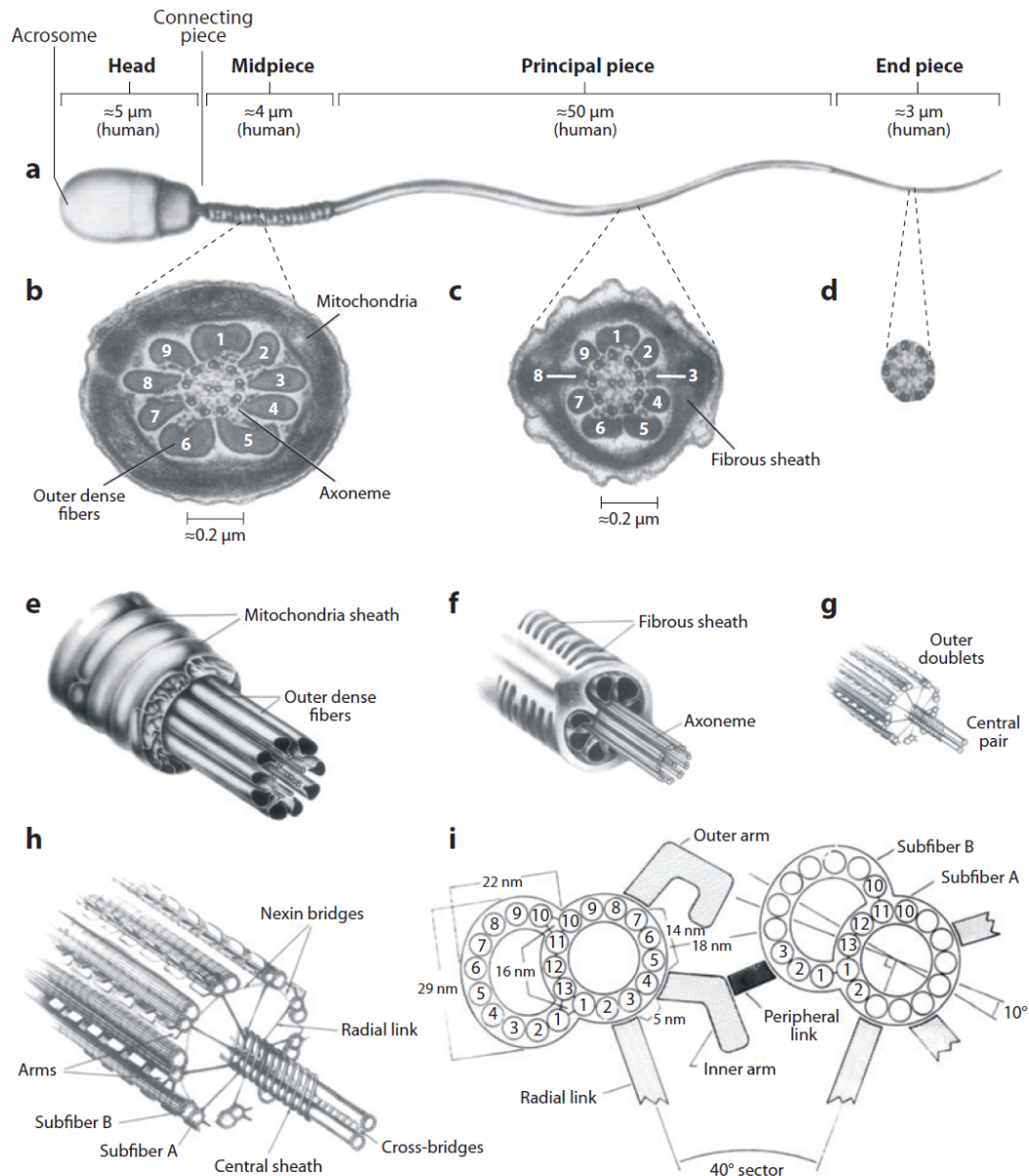
Figure 2.21: Sperm cell morphology. **a)** shows the sperm cell sections of head and tail with measures for human spermatozoon [161]; **b)** Cross section of the mid-piece of the flagellum looking from the sperm head. It shows the presence of the nine outer dense fibers right at the exterior of the concentric doublets, characteristic of sperm cells of "internal fertilisers". The fibers are labelled with the standard convention (clockwise from 1 to 9), where the first doublet (and hence fiber) is the one perpendicular to the centerline and to the separation of the two central microtubules. **e)** represents schematically the structure pictured in **b)**. **c)** is the cross section of the principal piece, while **f)** shows its schematic. It is possible to see the circumferential ribs of the fibrous sheath and the two longitudinal columns attached to fibers 3 and 8. Moving distally, the ribs of the fibrous sheath become thinner and the columns appear to be attached to doublets 3 and 8 distally. **g)** shows the end piece, where it persists only the axoneme structure. **h** and **i)** schematically illustrate the structure of the axoneme. **h)** shows the nexin bridges and the radial links while **i)** shows the inner and outer dynein arms that force bending into the flagellum, driving the waveform. Figure adapted from [164]

46

# Chapter 3

# Experiments at a microscale

In this chapter I would like to introduce the basic informations regarding the experimental part, talking about the samples used, the techniques to create the microfluidics devices used and finally the image analysis method.

## 3.1 Samples

The majority of the samples used for this work come from ram donors. We firstly started with frozen samples, which we store in the lab and hence result more accessible, but as explained below, the frozen samples had very low count of alive cells with reduced motility. Since the experiments with frozen semen gave unreproducible results, we moved to fresh samples, which are less accessible on a regular basis, but the samples have high sperm count and motility. The ram sperm samples, both frozen and fresh, are provided by the breeding company DC Fawcett Ltd.

### 3.1.1 Collection

The farm we obtain the ram samples from is a breeding company that, besides other services like embryo flushing, performs assisted insemination for the costumers' rams. For this procedure the samples have to collected and frozen into pellets and then introduced inside the female. Since it is a offered service, they do not own any ram, but only the animal needed for the extraction. For this, both the pellets of frozen sample and the fresh semen are not consistently from the same donor, but from a variety of different rams, for breed, age and most importantly semen quality.
The procedure for the sample collection is straightforward and carried through manual collection and a teaser ewe. The ewe is often a sterile specimen in order to avoid unwanted fertilisation. The ram is let free from his cage in an enclosed space where an ewe is stranded by a guillotine like device. When the ram is ready will jump on the female and

47

the worker of the farm will then redirect the penis inside a device and collect the ejaculate. This device is composed of a plastic tube that, in order to avoid a thermal shock for the ram during collection, has a pocket full of hot water. At the end a closed funnel shaped glass container is positioned, which collects the sample. The full container is left in a water-bath with temperature around 37 °C, the sample inside is then diluted, usually 1:1, and then its motility and concentration are assessed.

### 3.1.2 Frozen samples

The collected semen is mixed with the proper buffer and moved, in a glass of warm water, to the fridge where, in 4 hours circa, it cools down from 37 °C to 4 °C. The sample from the fridge is then frozen into pellets on a dry ice cube. These pellets are kept in a cryocontainer for two hours and then the concentration of progressive motile cells is evaluated. The evaluation is the same for fresh and frozen samples, with a 5 points scale for both motility and concentration, where 1 is the the lowest motility or concentration and 5 the highest. To thaw the pellets, there are different techniques, the one used by our group is to warm up the single pellets in a water bath. In case the sample needs to be diluted further, it is important to make sure that, independently form the type and brand of buffer used, at least 5% glycerol present, in order to avoid instantaneous osmotic imbalance that then destroys the cell membrane, increasing the agglutination episodes, where the sperm heads will glue to each other, and increasing the number of dead cells in the sample. According to our experience, after thawing between 50% and 70% of sperm cells do not survive the process, leaving only the $\sim 30\%$ alive and motile. If the glycerol is not present in the thawing buffer, the percentage of alive cells decrease to $\lesssim 20\%$. In this case the life span of the live cells is circa halved and the motility too, partially due to agglutination. Therefore, in experiments requiring high concentration and high motility, frozen samples are not suitable. Even if devices to concentrate cells are used, when high concentrations are required, cells do not live long enough to have the high concentration of alive cells necessary for our study. However, for tracking and low concentration experiments, frozen sperm works well.

### 3.1.3 Fresh samples

To work with fresh sample it has been necessary to travel and move the equipment to use to the farm. In case of ram sperm part of the lab equipment has been loaded on cars and drove to the Fawcett farm. This is possible only before lamb season, when the female are ovulating and there are rams present at the farm. This happens twice a year in the months of July-August and November-December. Hence the fresh semen experiments will be carried twice a year in a period of a couple of days. After collection, the semen is taken

into the water bath at 37 °C and diluted 1:1 with the buffer made in the farm, including egg yolk. The sample is then removed from the glass funnel and moved into a plastic tube and kept at room temperature for the rest of the day. Depending on the donor, the sample has a different live span, from a few hours to the whole day. It is often possible to obtain more samples during the day if needed, but not always from the same donor.

The fresh samples are visually evaluated by the farm workers on a scale from 1 to 5 for both motility and cell number. The sample used have a score of at least 4 in both fields.

The variability in the sample motility and life span is very high even in the same donor. Depending on the amount of samples given in that day, the number of days it already has been giving samples and finally the time of the day. Health of the specimen and its experience on donating samples can interfere with sample quality. Hence it is hard to obtain consistent samples, not only throughout the day but throughout the entire journey or in between journeys, even considering that the donors will change over different trips. For bull samples, the collection is pursue with an artificial vagina, but instead of using a teaser cow, a young bull will serve as a teaser, allowing the workers to control better the big animals and reducing the amount of hormones that otherwise would be present in the sample. The sample is then diluted 1:1 with a custom made buffer, whose composition is proprietary and has not been shared with us. the diluted specimen is then sent to our lab for experiments.

After describing the samples used in this work, I will proceed to describe the creation of the other essential object that allow us to carry on our experiments: the microfluidics device.

## 3.2 Creating Microfluidics Devices

To be able to study microorganisms in a controlled environment, the easiest and cheapest way is to use microfluidics devices. But microfluidics devices can be used for so many other purposes than just studying microswimmers [188, 189, 190, 191]. They helped automating DNA sequencing, protein crystallization and cell cultures, their design can be customised depending on the needs [192, 193, 194, 195, 196, 197]. They are very flexible structures they can be modified chemically, adding some sort of coating, the can be modified physically adding obstacles and barreirs or inserting agar structures for bacteria or inserting membranes.

Microfluidics devices are composed by channels, which are planar structures characterised by their cross section, length and height. The dimension of the channels can vary from a few microns to a few centimetres, but it has to be taken into account that the structures can collapse. For example, structures that are too wide and not high enough will collapse if not supported in the middle or alternatively pillars are added.

It is possible to have multiple channels on a single device. Those channels can be dis-
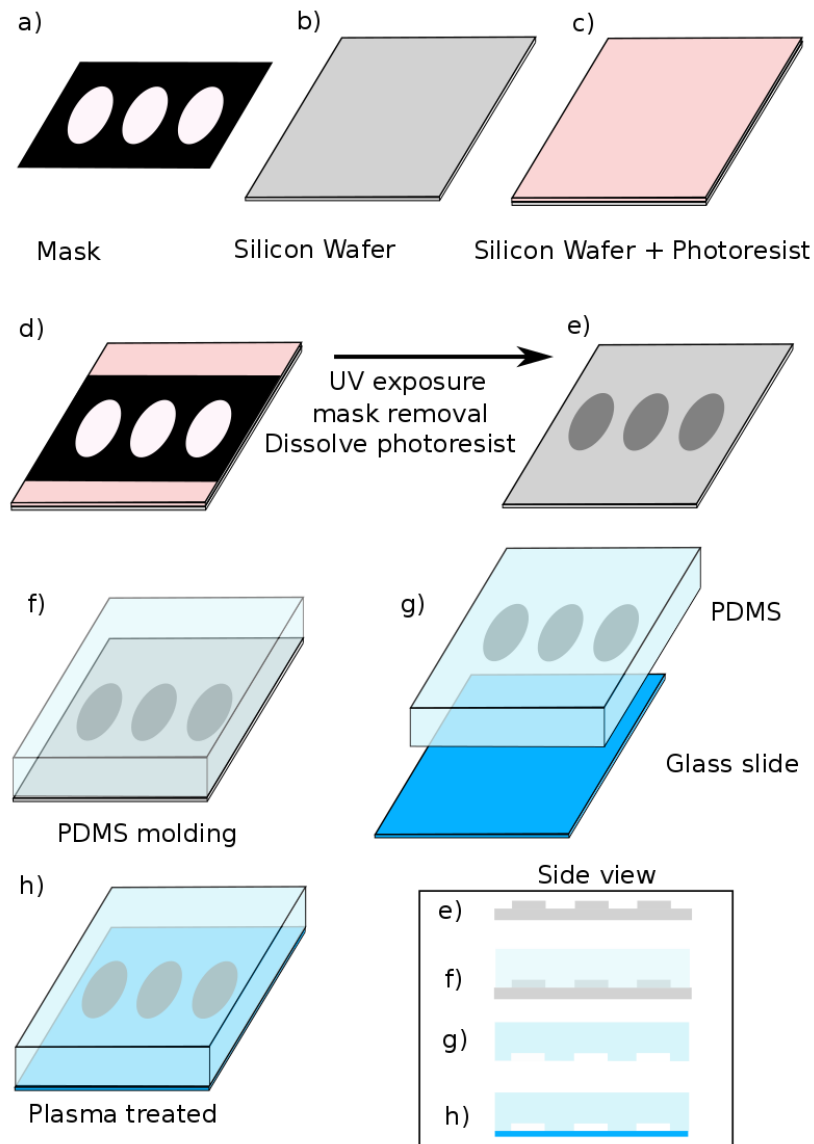
Figure 3.1: The figure tries to represent the major steps to create a microfluidic channel. First of all, **a)** the mask is printed and on the silicon wafer **b)** a layer of photoresist is poured **c)**, the thickness of the photoresist will define the final thickness of the device. **d)** The mask is then aligned over the photoresist and everything is exposed to UV light. The dark part of the mask will block the light, while the white part will let the light to pass through and to expose the photoresist, transferring the clear pattern from the mask to the photoresist. The mask is then removed and the photoresist not exposed is dissolved, leaving only the desired pattern embossed **e)**. The final wafer, with the pattern imprinted on it, is called master mould. **f)** On the master mould the PDMS is poured and let cure at high temperatures and then pealed off, **g)** leaving the PDMS hollow with the pattern. Finally, **h)** the PDMS is plasma treated and attached to a glass slide, creating a sealed channel with the desired pattern. The side views for step **e)** to **h)** are shown too.

connected and used independently or they can be connected, for example in parallel, and used at once as a single multichannel device.

### 3.2.1　How to make a channel

There are different methods that can be used to create a microfluidic channel. There are easy but not precise methods, in which the channel is written on a surface like glass or plastic through a scribe with a tip made of a very hard material like diamond [198, 199, 200, 201]; or another method is cutting from a soft material the desired design and inserting it in between glass slides [202]. These methods do not assure precision, the created surface is rough and difficult to reproduce systematically. A very reliable procedure that creates reproducible, reusable and precise channels is the soft lithography technique [203, 204, 205], shown in figure 3.1, which we will focus on.

#### 3.2.1.1　Wafer and photoresist

The first step in the soft lithograpy technique is to "print" the desired design on the silicon wafer [203, 204, 205, 206, 207, 208]. High quality crystalline silicon wafers are used, their dimensions vary from a few centimetres in diameter to around 50 centimetres. The surface used for the process has to be polished, hence it is very important to know if the wafers are single or double side polished. When a surface is polished it results shinier than the unpolished one, allowing by eye to distinguish the difference.
The process of printing the device on the silicon wafer, has to be done in a clean room, in order to allow the imperfections to be minimal, the roughness and the hight to be as controlled as possible.
The photoresist is a chemical sensitive to ultraviolet light. To coat the silicon wafer with photoresist, the chemical is deposited onto the wafer and then the wafer is spun at high speed and the photoresist spreads on the wafer. The speed of the rotation determines the hight of the photoresist layer and hence of the final channel. The photoresist then is exposed to UV light through a mask. The chemical reaction happening in the exposed region, called cross linking, changes the solubility of the photoresist in that region, leading to the possibility to dissolve some parts, while the others remain on the substrate creating the channel.
The solvent used to remove photoresist is called developer, and if positive resist is used the exposed part will be flushed away thanks to the developer, while in case of negative resist, the unexposed region will be removed. The latest is the technique used by our group, using a photoresist.
The photoresist needs to coat evenly the wafer, to achieve this, after pouring a few ml of photoresist onto the surface of the wafer, the wafer is spun at high velocity and the photoresist will spread onto the surface. This is called spin coating.
Even if the photoresist has been chemically optimised to ensure the surface adhesion, the UV absorbancy for the specific exposure system and the viscosity, there are still a few

things to consider when spin coating is preformed.

One of the biggest issues with spin coating is that both the rotational speed and the length of the time of rotation are important to define the final thickness of the photoresist layer. There are only simplified models of the system, but no fully comprehensive analytical solution, resulting in the empirical testing as the only way to have a connection between speed, time and thickness. Many manufacturers provide approximate spin curves, with the hight of the photoresist layer vs. the rotational speed. This can be used as a starting point to define what speed and time are needed for the desired height, but it has to be complemented with testing.

The final complication worth mentioning is at the edge of the wafer. The photoresist after spreading onto the entire wafer can create a thicker or thinner layer at the edge. This is due to the surface effects at the air-wafer-liquid boundary, that change the geometry of the liquid layer, creating an non uniform coating. These edge effects have to be taken into account when designing the channels, considering that the channel itself has to lay away enough from the thickness discontinuity to be able to have an uniform height.

### 3.2.1.2 Masks

A mask is a transparent substrate with a specific pattern on it, this is placed in contact with the spin coated wafer. When exposed to UV light, the UV light transmits through the transparent parts and expose the photoresist of the underlying wafer. This exposure allow the transfer of the pattern to the coated layer of the wafer. The transparency masks can create channels of height $\geqslant 15\mu$m. They are printed with a high quality laser printer, with a maximum resolution around 5 $\mu$m.

Two more types of masks exist, but their cost increases with their resolution. One is the chrome mask, which is suitable for smaller designs, of around a micron resolution. They have a coating of photoresist over a layer of chrome laying on a soda lime or quartz glass plate, the pattern is drawn over the photoresist layer by a laser. The photoresist is then developed and this etches the chrome layer, when all the photoresist is washed away, the design is engraved on the plate, creating the mask. Finally, for even smaller designs, the mask has to be created through e-beam lithography or other very specialised equipment. This is the most expensive method of the three.

In order to expose to UV light the wafer through the mask, a mask aligner is needed. The mask aligners are instruments with a vapor lamp, either mercury, xenon or deuterium lamp, that exposes the photoresist to UV light. The precision stages and the optics allow control of alignment. The vacuum is used to hold the mask in place over the wafer, securing it during the exposure process. There are two basic type of aligners, the contact devices, where the mask and the wafer touch each other when aligned, and the proximity

aligners, in which there is a small separation between the mask and the wafer, protecting the mask from any damage and ensuring that the mask can be reused. The disadvantage of the proximity aligners is that the separation reduces the resolution of the exposed pattern. After exposure, the pattern has to be developed and the not exposed photoresist will be washed away, leaving a raised pattern that will be then used to do soft lithography and create the microfluidic device, as shown in figure 3.1 e.

### 3.2.1.3 Soft lithography

In 1998, the Whitesider group [205], reported a method to mold some elastomer into the desired channel. Polydimethylsiloxane is a polymeric organosilicon, composed by dimehylsiloxy units with a trimethylsilyl end groups linearly bonded. Depending on the number of $Si(CH_3)_2 - O-$ units in the polymer, the PDMS change its viscosity, the longer the polymer the more viscous the material. PDMS elastomer is mixed 10:1 with a curing agent and degassed in a vacuum chamber, to avoid the presence of air bubbles in the final, solidified polymer [203, 204, 205, 206, 207, 208]. The polymer mix is then poured onto the master mold and cured at temperatures $\geq 65\,°C$ for at least one hour, until it solidifies (figure 3.1 f). When solid, PDMS is an elastic polymer that is optically transparent and non toxic for biological organisms.

PDMS can be used to create bio-compatible microfluidic channels, thanks to the property that it conforms to irregular surfaces, allowing the formation of devices from a master mold and when the PDMS is solid, it is easy to peal off the cast, not damaging the mold. This leads to the possibility to reproduce the same devices multiple times using a single master cast, increasing the consistency in the environment used in the experiments.

Every deformation of the device is reversible, allowing flexibility and the possibility to create valves and switches that are pressure dependent. The surface of the devices can be altered chemical, like coating with specific chemicals. Finally the PDMS can be bonded either permanently or temporarily to the desired surface.

After curing, the solid PDMS replica is pealed off the master mold and cut into a size possible to attach to the desired surface (glass, PDMS, etc.). Inlets and outlets are punched into the PDMS layer with a sharp biopsy puncher and then the PDMS surface is undusted. To attach permanently the PDMS replica onto a surface, in our case a glass slide, the surfaces are treated in a plasma cleaner (figure 3.1 g). At low pressure, an oxygen plasma is created which disrupts surface silicon-oxygen bonds on the PDMS. The treated surface of the PDMS is usually placed over the plasma-treated surface of a glass slide and once the activation wears off the silicon-oxygen bonds between surface atoms of glass and PDMS, permanently sealing the channel.

The attached device is then left for 30 minutes on a hot plate at around 100 °C, stabilising

the bond. This sealing allows the device to resist applied maximum pressures between 200 and 350 kPa. This is important because in order to eliminate the bubbles after filling the devices, high pressure is applied. Since PDMS is air permeable, the air bubbles get diffused out of the device when high water pressure is applied. The duration of pressurisation depends on the amount of bubbles, their size and the size of the device. It could range from a few minutes to overnight. Having air bubbles in the device alters flows inside it, affecting in the experiments.

## 3.3   Analysis method

The technique used to analyse the recorded images is the particle image velocimetry (PIV), where the motion of the particles in the fluid is evaluated in order to determine the local velocity vectors [209, 210, 211, 212, 213]. A final flow field matrix is created per each pair of images. Differently from the measuring technique that require a probe to be introduced in the fluid to measure the flow, the optical techniques like particle tracking or PIV do not disturb the flow and allow for flow visualisation without interfering with it. Particles are introduced in the fluid to be able to follow the flow and hence to image it and either the distance covered in a certain amount of time or the time necessary to cover a certain distance has to be found.
PIV techniques are used when the amount of particles present in the fluid does not allow for particle tracking, but their density is so high that paths are not recognisable and they overlap frequently enough to not allow identification of motion of individual tracers.

### 3.3.1   Principles of PIV

A PIV experimental set-up needs to take into account of [214, 213, 215]:

- **Tracers**: In order to visualise the fluid, tracers have to be used. They need to be right in size, compatible with the flow aimed to measure and compatible with the recording method used. Their size needs to be small enough so they can be transported by the fluid, but big enough to be recorded by the imaging method [216, 217, 218].

- **Recording**: the tracers will scatter a light that then has to be picked up by a recording system, either recording two separate frames or a sequence of frames from a camera. The recording parameters have to be set at the optimal rate in between images in order to allow the best outcome for the displacement determination [218, 219].

- **Evaluation**: PIV recordings have to be evaluated in order to determine the particle displacements between two consequent images [220, 221, 222, 223, 224].

- **Post-processing**: it allows to remove invalid measurements and aberrations and to extract the flow quantities of interest [225, 226, 227, 228].

In order to evaluate the velocity fields for the image pair, the images are divided into sub-areas that are called interrogation windows [229, 225]. The determination local displacement vectors for the tracers in the two consequent images is done through a statistical method, specifically cross-correlation [220, 230].

The general aspects for a PIV analysis that have to be accounted for will be briefly outlined below. It has to considered that the mistakes made during the recording phase of the experiment, cannot be remedied during later evaluation, analysis and post-processing.

**Non-intrusive velocity measurements.** The ability of measuring velocities in a flow without interfering with the flow itself adding probes, wires or tubes, allows PIV to be applied to high-speed flows, laminar boundary layers flows and micro-systems.

**Whole field techniques.** Another advantage of measuring the flow with an optical method is the be able to record and analyse the field of view imaged, without the local restrictions you encounter using a probe. The only necessary thing for PIV to work properly is that tracers are present in the media. On the other hand, the temporal resolution is limited by technology, in particular by the rate of recording of the images. These restrictions have to be kept in mind when comparing tracking techniques with PIV.

**Distribution and density of tracers in the fluid.** A more qualitative approach for flow visualisation can be used, locating the seeding device in the specific and desired area of analysis. Giving to the tracers origin a specific location, the temporal evolution of the structures in the flow can be studied in a more effective way, highlighting only the part of the fluid of interest. Unfortunately, in order to have an optimal quantitative evaluation of the velocities, high quality PIV recordings are needed and this is possible only when the distribution of particles is homogeneous in the media [216, 217, 218, 231].

While considering the tracers distribution, three general types of density distributions can be distinguished: low, medium and high. In images with low density concentration of particles, single tracers can be located and their temporal evolution and movement can be traced throughout consecutive images. Hence a single particle tracking method can be used, like Particle Tracking Velocimetry (PTV). This single particle techniques doesn't work in two cases. Firstly, when small details of the flow have to be resolved, reduced amount of tracers doesn't allow full flow visualisation. On the other hand, when large structures are present in a fluid a wider field of view is needed to resolve them. In both these cases, the amount of tracers in the image is increased, where single particles in every instantaneous can be detected, but from consecutive images is not possible to uniquely detect the path taken by them. Those densities are optimal for statistical evaluations of velocities like PIV techniques, because in each interrogation window, the number of tracers (more than three

particles per window) present allow the algorithm to define the position of the tracers in the window and correlate it with the position of the tracers in the same window in the consequent image, evaluating the average direction and velocity of the flow shown by the particle in the interrogation window. Finally, for high density, particle recognition does not work, making it impossible to detect tracers and their spatial path and hence compute the flow velocities. A specific type of PIV called Laser Speckle Velocimetry can work when tracers form speckles in the fluid [232, 233, 234, 235].

**Velocity lags.** It is important to find the appropriate balance between particle size, detection and flow visualisation. Tracers have to be small enough to follow the motion of the fluid faithfully, but they have to be detectable by the camera for the desired observational field. For example, in the case of weak and strong velocity fields are present in the system, small particles are needed to image the flow. In case of a desired large observation field, near the strong gradients area, the velocities can not be resolved with small tracers, bigger particles are needed.

**Optimization.** Parameters such as size of particle images, interrogation windows size, density of tracers, number of interrogating areas, etc. need to be optimised to obtain optimal working of evaluating algorithms, desired accuracy and determination of appropriate number of vectors [212, 215, 229, 230, 231].

Objects present in the flow can affect the recordings, modifying the light reflection and hence images will results over exposed, with traces turning undetectable. The experimental set up has to be optimised too, in order to achieve the best image quality possible [211, 212, 236].

### 3.3.2 Micro-scale tracers

When we move to micro-PIV [237], the tracers size reduces to less than a micrometer. In these scale, the collisions between particles and fluid molecules create a collective effect (Brownian motion) that prevent the tracers to follow to some extent the flow. It can cause a measurement error in either the particle location or in the calculated velocity. The Brownian motion can be defined as the random motion of tracers due to collisions between the thermally excited fluid molecules and the particles suspended in a fluid [238, 239]. Usually this effect is modelled as the Gaussian white noise. The mean square distance covered by the particle diffusing in a time $\Delta t$ is proportional to the diffusion coefficient D of the tracer particles and the time interval [240, 241]. The diffusion coefficient has been defined by Einstein as:

$$D = \frac{k_B T}{3\pi\mu d_p}$$

with $k_B$ being the Boltzmann constant, T being the absolute temperature of the fluid, $\mu$ the

fluid dynamic viscosity and $d_p$ the particle diameter. The error introduced by Brownian motion on the local displacement of the tracer is in one dimension of the order:

$$\epsilon = \frac{1}{|\mathbf{U}|}\sqrt{\frac{2D}{\Delta t}}$$

From the Brownian error it is possible to establish the lower limit regarding the measurements of the time interval $\Delta t$. Indeed, at short times, the Brownian motion dominates the overall measurements for the particle movement and it has to be considered when tracing small particles.

### 3.3.3   Recording techniques

The recording modes for PIV can be divided into two macro categories: the first one is called single-frame/multi-exposure PIV, and it images the particles evolution, recording it at multiple times but in one single frame, while the second method, multi-frame/single-exposure PIV, records the particles into single images for every time step.
The major difference between the two methods is that when the evolution is recorded in one single frame, the temporal order informations are not retained, leading to an ambiguity when the displacement vector is recovered. Additional schemes have to be introduced in order to account for this ambiguity, mostly if the direction of the flow is not previously known. On the other hand, the multi-frame/single-exposure method preserves the temporal order and the final velocity evaluation is more reliable results. Indeed, with this method, detecting the correlation peak maximum is possible for both very small displacements of the particles and for displacements larger than the interrogation window, which is the method we used in this work. This latter recording technique is the one used in this work.

### 3.3.4   Statistical PIV evaluation

Historically, the first mathematical description of the statistical method to evaluate PIV velocities is given by Adrian 1988 [242, 233, 243, 244], who focused on the auto-correlation based methods that have subsequently been expanded to the cross-correlation method commonly used nowadays. We will proceed to briefly present a simplified mathematical model and the statistical evaluation, trying to focus mostly on the method used during our own velocity evaluation.

### 3.3.4.1 Particles location

In the PIV evaluation process, the image is subdivided into interrogation windows, where the tracers are white dots on a dark background. When considering a single exposure recording, as in our case, the image shows a random distribution of particle, which correspond to the pattern of N tracers inside the flow. If we look at the projection of the tracers distribution in the window onto the image plane, we obtain an image which is the superimposition of the images of individual particles. In order to evaluate the velocities in the PIV grid, the local cross correlations between the particle ensembles in the same interrogation windows of two consecutive images.

### 3.3.4.2 Fast Fourier Transform method for evaluating cross correlation

The local cross correlation is calculated for each pair of interrogation windows composing the two frames. Off-setting the windows sampling according to the mean displacement of tracer in between frames is advantageous, reducing the in-plane loss of correlation and increasing the peak strength [227, 221, 226, 225, 220, 228, 222]. For a faster computation of the cross correlation function the Fast Fourier Transform algorithm is used. The final evaluation process can be displayed schematically as in figure 3.2.
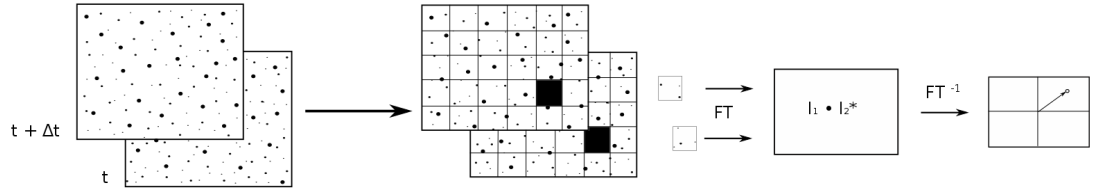


Figure 3.2: Flow chart for the double frame/single exposure recordings with the digital cross correlation method evaluated through Fast Fourier Transform.

This algorithm takes advantages of the correlation theorem, stating that the cross correlation of two functions is equivalent to a complex conjugate multiplication of their Fourier transforms. The computation of the FFT is an easy implementation of the discrete data, reducing the computational operations from $\mathcal{O}(N^2)$ to $\mathcal{O}(N\log_2 N)$. Hence, calculating the cross correlation is reduced to computing two 2D FFT, on equal sized samples of the image and then multiplying the complex conjugate of the resulting Fourier coefficients. The inverse Fourier transform is then calculated and it produces the actual cross correlation plane, which results to be with the same spatial dimensions as the two input samples. While using a 2D FFT to compute the cross correlation plane, we have to take into account the properties of this approach:

- **Fixed sample sizes:** The efficiency of the FFT algorithm comes from recursively implement the symmetry property between the even and odd coefficients of the Discrete Fourier Transform.

- **Periodicity of the data:** If we assume data periodicity, then the FFT can be computed over finite domains. Many methods for the estimation of the spectrum can be used each one with its the associated artifacts, that can lead to bias, systematic errors or even to no cross correlation signal at all, given the noise overpowering the signal itself. For example changing the window size sampling, according with data periodicity, two or three times the spatial periodicity, the bias and the systematic error can be significantly reduced.

- **Aliasing:** The previously mentions data periodicity, gives periodic correlation. When the tracer displacement is over the half-length of the interrogation window, the frequency signal will be misidentified and distortion will be introduced. To reduce the distortion, a wider interrogation window needs to be used. Showing the importance of the choice of the sampling.

- **Displacement range limitation:** The sample size, N, limiting up to N/2 the maximum recoverable displacement. Practically, the strength of the correlation peak is linked to the displacements, indeed, it will decrease with increasing displacements since the possible particle matches decrease proportionally. Using window shifting techniques the limit is applicable only for the first iteration of the evaluation.

- **Bias error:** As explained before, the periodicity of the data can give biased correlations. This error in estimation decreases with a balance for the interrogation window size, large enough to include a couple of the periodicity and smaller than half-length of the interrogation window.

### 3.3.4.3   Digital interrogation techniques

Being able to transition from photographic recording to digital imaging allows to improve the interrogation algorithms. In the following paragraphs we will concentrate on the two we used in our work: the multiple pass and the grid refining interrogation techniques. We used a customised MATLAB code downloaded from the MATLAB website called PIVLab - Time-Resolved Digital Particle Image Velocimetry Tool for MATLAB [214]. They have been modified to satisfy the requirements of our analysis and recoded so to not use the GUI, which used to slow down the analysis.

### 3.3.4.3.1 Multiple pass

In this process the interrogation windows are shifted with an integer offset in the second interrogation pass. Adjusting the offset accordingly to the mean displacement, the ratio of matched to unmatched particles is increased, which itself increases the signal-to-noise ration of the correlation peak [229, 226].

An example of working procedure for this type of technique is composed of four steps:

1. Standard digital interrogation, with windows offset close to data mean displacement.

2. Scan the data in search of outliers and replace them by interpolation of the neighbouring values.

3. Move the interrogation window accordingly to a previously defined offset that should be larger than the average local displacement of the particles.

4. Repeat the interrogation process and linearly interpolate the flow fields created from the overlapping portion of the windows. Continue until the entire image is completed.

### 3.3.4.3.2 Grid refining

Refining the sampling grid is a technique that can be used to improve the multiple pass interrogation algorithm. It is a hierarchical approach where the sampling grid is refined while at the same time the interrogation window size is reduced. This technique allows one to use interrogation windows that are smaller than the particle image displacement, which is helpful when the particle density is the image and their displacements are very high. In those cases the classical evaluation schemes are not successful, because it is not possible to use small interrogation windows without losing the large displacement correlation [226, 211, 213].

The main steps to refine the sampling grid are:

1. Large interrogation sample, capturing the full dynamics of the displacements accordingly to sampling rules.

2. Perform a standard interrogation with large interrogation windows.

3. Scan for outliers and interpolate with the neighbours to replace them. The displacement calculated at this point will be used as an estimate for the next iteration.

4. Offset the interrogation windows between each other using the previously estimated displacements.

5. Repeat steps 1 to 4 after reducing the size of the interrogation windows until the desired resolution is reached.

6. Linearly interpolate the flow fields from the different sizes of the interrogation windows, which are arranged in grids with increasingly more points as the windows reduce in size.

The final velocity field will be the linear interpolation of increasingly more defined matrices, including both the large and smaller scale effect. In this case, for example, if light Brownian motion is present, it will be picked up by smaller windows, but on the wider interrogation windows, the averaging over the many tracers will almost exclude the Brownian effects. In the final flow field, being the interpolation of the two fields, the effect of the Brownian motion will be reduced.

#### 3.3.4.4 Cross correlation peak detection

A very important feature of the digital PIV process is the estimation of the correlation peaks can be up to subpixel accuracy [230, 225, 227].

The correlation values derive from integral shift for the discretised input data, hence the displacements determined from the highest correlation value have a half a pixel uncertainty. However, interesting informations can be extracted from the correlation values since the cross correlation functions are statistical measures of best match. The extracted informations can be used to have an estimation on the mean shift of the particle image in the interrogation window.

The big challenge in order to estimate the position of the correlation peak is to separate the signal from the background noise. Many different methods can be used, but one of the more robust is to fit the correlation data with a function. Mostly when dealing with narrow correlation peaks, it is common to estimate the displacement using only three adjoining values, usually with a Gaussian peak fit. The choice of a Gaussian fit is that if the particles are properly focused, they are represented by Airy intensity functions, which can be approximated as Gaussian intensity distributions, finally the correlation between two Gaussian is itself a Gaussian function.

In case of larger correlation peaks a different approach should work better. For example, when the particles are larger, the noise level becomes more significant while there is a decrease in the difference between close correlation values. Thus a centroiding approach can work better, since ir uses more than three values around the peak. On the other hand, when the particle image is too small, then both the centroid and the three-point estimators will not work in a proper way. Hence it is important to have similar size particles and mostly find the best approach to detect the correlation peak.

### 3.3.4.5   PIV uncertainties

Errors in PIV derive from multiple sources and are a combination of a variety of aspects [227]. We will proceed to name the most important here following.

**System components errors.** Optical aberrations can distort the shape of the particle image and when not Gaussian, it will affect the peak detection error. In addition, those distortions can cause a small direction error, affecting the measure of the flow direction and its magnitude.

**Flow errors.** The flow itself can affect the final results of PIV. For example when the flow gradients or the velocity fluctuations are large, measurement errors are more likely to appear. Additionally, the measurement error can be due to variations in the density of tracers in the flow.

**Evaluation errors.** During the digital analysis, as already mentioned, many errors and bias can arise and influence the final results. The major error contribution derives from the estimation of the cross correlation function. The best approach to measure this uncertainty is to calculate it in the cross correlation function of a uniform flow, where the flow will be biased if the estimation of the correlation function is not optimal. This gives a realistic estimation of the measurement uncertainty, but does not allow to find the dependence of the error from the specific parameters, like the particle image size, its density and its intensity, the background noise, the precision of the measurements, turbulent fluctuations and velocity gradients.

Another approach is to estimate the error by using numerical simulations, where only one parameter at the time would be modified and the PIV estimations will be carried, its errors computed and then the results would be compared to the known results of the experimental data. Even though this approach gives full control over the parameters of the system, since many real system are very complex and not easily described by physical laws, the model can results very simplistic. Hence these approximations and assumptions lead to a underestimation of the true values of the real system uncertainties.

In our case, we calculated the PIV fields of both tracers and swimming cells at low concentration of swimmers and compared it with a tracking algorithm. If they the vectors of the two flows are comparable then we assumed that the PIV estimation is a valid representation of the flow fields recorded. Additionally, the program used, calculates the distributions of velocities, from which it is possible to validate and filters the outlier vectors with values over three times the standard deviation of the overall data distribution, which are more likely to be due to errors in the function estimation.

### 3.3.4.6 PIV post-processing

After the raw PIV analysis, the data should be processed further [220, 227, 230, 225]. Needing to inspect a large number of data, a fast, reliable and automated post-processing techniques is essential. The basic steps of PIV post-processing are quickly outlined below.

**Validation of raw data.** PIV evaluations are not perfect, resulting in a certain number of outliers in the final results of the automatic evaluation process. The incorrectly determined velocity vectors can be recognised during visual inspection of the raw data, but for large data, automation is needed. Special algorithms have been developed in order to validate the flow field data.

Outliers can be identified by their magnitude and direction because they considerably differ from the magnitude and directionality of their surrounding neighbouring vectors. Another very common characteristic is that they can look like isolated spurious vectors. Alternatively, They can appear as a cluster of vectors with the same direction and finally, it is often possible to find them at the boundaries of obstacles in the fluid and the edges of the image. After finding the outliers, they are removed from the velocity matrix and replaced by vector calculated through interpolation or extrapolation.

**Replacement of incorrect data.** In order to calculate different quantities from the PIV vector fields, the vector fields themselves should not have gaps in the Cartesian mesh. Hence, to fill the gaps in the mash the vector have to substitute with estimated values of the velocity. Usually in order to replace the vectors, the bilinear interpolation of the fourth nearest neighbours is calculated and the result replaced in the mesh.

**Data reduction.** Simple techniques to extrapolate quantities from the vector fields can be used, like averaging the flow field in order to infer the fluctuations and the mean flow. Conditional sampling techniques can used, for example it is possible to differentiate between the non periodic and periodic parts of the flow fluctuations through phase averaging. Additionally, vorticity, divergence and other vector field operators can be calculated. They are all considered under the data reduction post-processing and they all help evaluating the structures that dominate the dynamics of the flow. Moreover, the decomposition into modes is required in order to describe the behaviour of unsteady flows.

# Chapter 4

# Transition to collective motion in bulk environments

## 4.1    Introduction

The idea for the work shown in this chapter comes mostly from two main works, the first one, experimental on sperm turbulence at high concentration of swimmers [103, 104] and the second one, a simulation on bacterial collective motion depending on aspect ratio and concentration of swimmers [108].

As already said in section 2.2.2.2, there are studies that focus on sperm turbulence at high concentration of swimmers [103, 104]. In these experimental works the undiluted fresh ram semen is introduced in glass chambers of different heights. Whirlpool structures, made of sperm cells locally aligned, are present in these systems. Analysing the flow fields, an integral length scale $L^*$ is present, which depends on the square root of the ratio between energy and enstrophy. This length scale is similar to the detected size of the whirlpool structures and $L^*$ defines the typical correlation length of the system. Additionally, doing a Fourier analysis of the flow fields, the energy power spectrum shows three different regimes: for small wavelengths, there is a saturation to a white noise plateau; above the critical wavelength, where there is a $k^{-3}$ power law dependency as in quasi-2D turbulent flows; for large wavelengths, there is again a saturation, but in this case consistent with the single cell motion. From these three regimes from the Fourier analysis, it is possible to deduce that the velocity correlations increase from the individual swimmer to a collective length scale similar to $L^*$. In these works, a few dilutions of the samples have been analysed, showing that the dilution affects mostly the smaller scales, decreasing the velocity correlations. The large scales are not affected by the dilution, since in the flow the whirlpool structures are still present.

On the other side a simulation study [108], shown in section 2.2.2.1, simulates self-propelled

rods without noise. Variations in the aspect ratio of the considered particles and volume fraction of swimmers in the system, creates phase diagram, where six different motion states are present, as shown in figure 2.11. Looking at probability density functions, velocity correlation functions and fluctuations it is possible to characterise the flow of the different phases, making it possible, for the turbulent phase, to define a typical vortex size. Looking again at the Fourier analysis, the power spectrum of the turbulent phase shows two regimes: a $k^{5/3}$ decay for small wavelengths and a $k^{-8/3}$ for large wavelengths. This points that self-sustained bacterial turbulence has some properties in common with the classic turbulence for small scales, while at large scales they differ.

The aim of this chapter is to combine these two works in the field of sperm motion. We increase progressively the concentration of sperm cells in a channel and we study the changes in the flow with the increase of swimmers in a confined, yet large, volume, through the main flow characteristics, like the correlations, power spectra and turbulent fractions. We saw the arise of collective motion depending only on the concentration of active cells.

## 4.2 Experimental Methods

### 4.2.1 Samples

Ram samples were collected in loco, fresh in the morning from healthy animals. Experiments started right after collection and got carried on for a couple of hours, until cells were dead or enough data were taken. Only good quality semen was used for these experiments, using high concentration and high motility samples (between 4 and 5 value in the usual scale of evaluation). Usually the second donation of the day, half an hour after the first collection, was used. The samples were kept at room temperature, which was around 20°C at any time. Usually the original sample was kept undiluted or diluted at a ratio 1:1 with a specific solution (tetradyl, egg yolk and DI water).

The bull samples are collected from healthy bulls in a dedicated facility. The sample is diluted with a ratio 1:1 with specific solution custom made by the sample providing company. The sample is then transported to the laboratory keeping it at low temperature with dry ice. Transport usually takes 2 hours. Then motility and concentration are assessed before starting any experiments and only the samples with highest values of motility and number of alive cells are used to carry on the experiments.

### 4.2.2 Experimental set-up

The PDMS chambers are pre-filled with buffer solution. The samples are introduced in the external ring of the PDMS channel, in such a way the only part full of sample is the
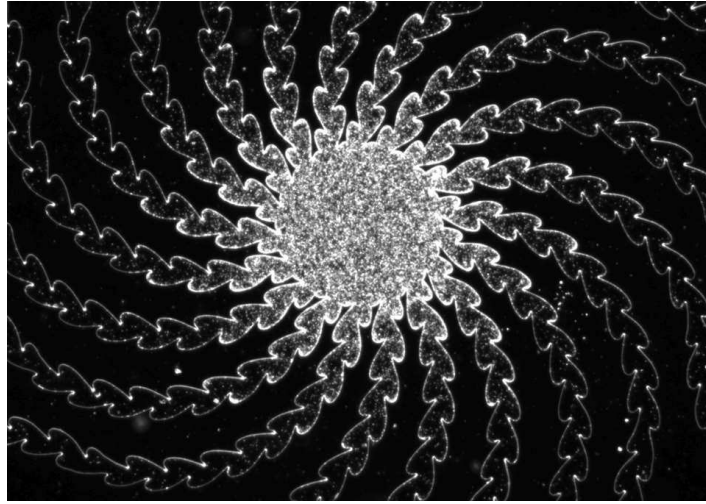
Figure 4.1: The PDMS device used has a structure of channels made of clove-leaf like structures that direct and "trap" the sperm cells in the central chamber of the device where the experiments are carried and the data recorded. This method allow the progressive increase of the number of cells in the central chamber, autonomously increasing the concentration, without need for progressive manual dilutions or concentrations.

external one, giving motile cells the possibility to swim their way to the central chamber of the device, increasing the concentration in loco with time (as shown in 4.1). The motile cells progressively arrive to the central chamber, increasing the concentration of active particles in the chamber in time. The spermatozoa will be trapped in the central chamber thanks to the channels connecting the loading ring to the recording chamber. Those channels will redirect towards the centre the swimming sperm cells that try to escape.

The ram data have been recorded in dark field microscopy. The dataset consists in multiple concentrations recorded in the same chamber, during a span of around five hours. The distance between recordings was not uniform, as it depended on the increase of cells in the recording area. Each record is long 10 s at 100 fps.

The bull data is a recorded in bright field. The light intensity has been kept constant throughout the length of the experiment, which took around 4 hours. Using constant lighting it has been possible to estimate the number of cells at each concentration. The acquisition timing technique has been kept the same as the ram experiment, not having regular linear time intervals, but visually assessing the concentration increase to select a new recording time. The frame rate used for recoding is 33 frames per second on a total of 10 seconds of recording.

Finally, the camber used is 100 $\mu$m thick and the recordings were performed at 30 $\mu$m from the bottom surface. The experiments were performed at ambient temperature, approximately 20 °C.

| Sample | Camera | Method | Magnification | fps | sec |
|--------|--------|--------|---------------|-----|-----|
| Ram | Edgetronic | Dark Field | 10x | 100 | 10 |
| Bull | Point Grey | Bright Field | 6x | 33 | 10 sec |

Table 4.1: Image acquisition details for the two sets of experiments.

### 4.2.3 Analysis

#### 4.2.3.1 Concentrations

The concentration of sperm cells has been estimated by correlating the light intensity in the images with the number of cells calculated at low concentration. When this correlation has been fitted by a function, it is only necessary to assess the light intensity of the images for the concentration and then deduce the number of cells. In this way, even in a very dense suspension it is possible to calculate the number of sperm cells present in the fluid. We convert the concentration from number of cells per millilitre to the percentage of volume fraction in order to compare it in an easier way to the previous works, for both sperm and bacteria. This latter have a very different size to sperm cells, usually a bacteria is 10 times smaller than a mammalian spermatozoon. On the other hand, since the ram and bull samples have very different starting concentrations and critical concentrations, to collapse the two curves we decided to normalise by the critical concentration at which the phase transition occurs.

So, the final concentration $\phi_n$ used in this work for the comparison between ram and bull is:

$$\phi_n = \frac{\phi - \phi_C}{\phi_C}$$

where $\phi_C$ is the concentration at which the properties of the fluid has been seen changing. For the bull experiments $\phi_C \sim 0.6 \cdot 10^8$ cells/ml, while for the ram experiments the critical concentration is $\phi_C \sim 7 \cdot 10^8$ cells/ml. To convert the concentrations from number of cells per millilitre to volume fraction, we use an estimate of the volume occupied by the single sperm cell $A_p$:

$$A_p = 50 \cdot 5 \cdot 5 \cdot 10^{-12} \text{cm}^3 = 1.25 \cdot 10^{-9} \text{cm}^3;$$

So, for the sake of completeness, the volume fractions are calculated as:

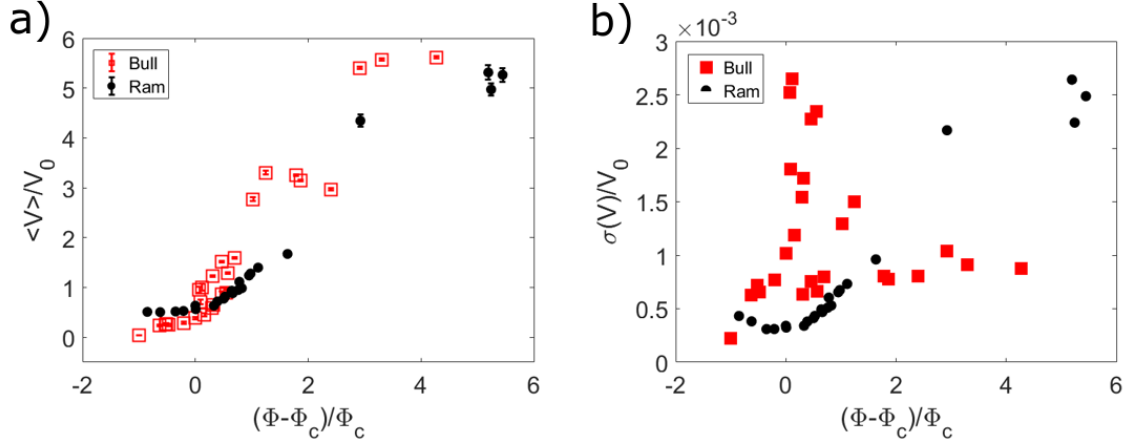$\phi = (\# \quad \text{cells/ml}) \cdot A_p \cdot 100.$

Figure 4.2: Velocities for ram and bull and their standard deviation. The velocities are averaged in both time and space and they are then normalised by the single sperm swimming velocity calculated from the tracking algorithm for the lower concentration data. Both datasets after the critical concentration show an increase in average fluid velocity, up to 6 times the single cell velocity.

#### 4.2.3.2 PIV velocity fields

The velocity fields are calculated through PIV analysis thanks to both costume made and provided programs from MATLAB (Mathworks Inc. USA), specifically the PIVlab package [214]. The PIV velocity fields are the used to compute the other quantities for the analysis of the flow, which are normalised by the following constants: single cell, low concentration velocity $V_0 = 50\mu m/s$ and the ratio between single cell and its length $\omega_0 = \frac{V_0}{l_0} \sim \frac{50\mu m/s}{50\mu m} \sim 1s^{-1}$.

## 4.3 Variation of Basic Parameters

### 4.3.1 Velocity

Two different vector fields are created by the PIV analysis for each single couple of images, $V_x$ and $V_y$, of size depending on the interrogation window size chosen.

From the two vector fields, we calculate the average speed in space at each time step, which can be plotted as a function of time per each concentration.

We desire to additionally average over time, in order to study the variation of the velocities with respect of the concentration. We plotted the velocity evolution in time for all concentrations and given that the average value remains fairly constant in time for each separate recording, we can feel confident in averaging the velocities over time without loosing any important information.

After proving that the average velocity in the image is constant in recording time, it is pos-
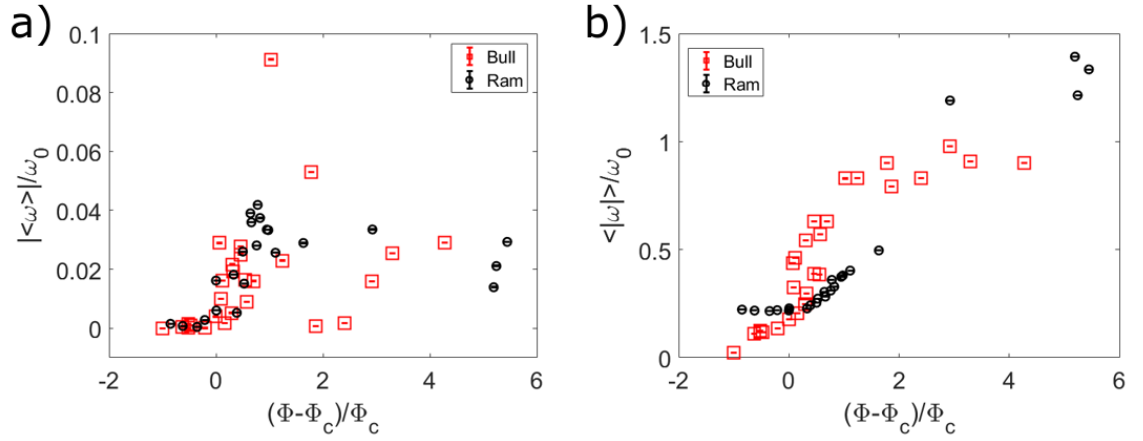
Figure 4.3: Both the average vorticity and absolute vorticity are normalised and plotted as a function of concentration. They both show a sharp increase after critical concentration, meaning that more structures like jets ans swirls appear in the fluid, with local swimmer alignment.

sible to average the velocity in time, resulting in $\overline{\langle V(\phi_n) \rangle}_{x,y}$, where the over-line is the average in time. The velocity at each concentration is normalised by the velocity of a single cell $V_0$, which has been calculated through particle tracking at lowest concentration and its value is $50\mu m/s$.

The resulting plots of the average velocity per normalised concentration $\phi_n$ are shown in figure 4.2 a), where both samples are shown together. In figure 4.2 b), it is possible to see the normalised standard deviation always as a function of the normalised concentration. This standard deviation is calculated from the probability distribution functions of the velocity per each concentration. The standard deviations shown in figure 4.2 b), do not appear to have a coherent behaviour between the two species.

### 4.3.2 Vorticity

The vorticity was analysed similarly to the velocity fields in the previous section. First of all the average per frame of both vorticity and its absolute value have been computed. Both quantities have been plotted as a function of the recording time, showing that they both stay fairly constant during the time, justifying the possibility of averaging in time at each concentration, without losing important information.

After confirming the constant behaviour of the vorticity during the time of the recording, the average in time is computed of both space averages of vorticity and its absolute value. Since the average vorticity has a chirality, depending on the rotations of the vortices and jets present, we decided to loose the chirality information plotting the absolute value of the time and space average. Finally, both values are normalised by $\omega_0$.
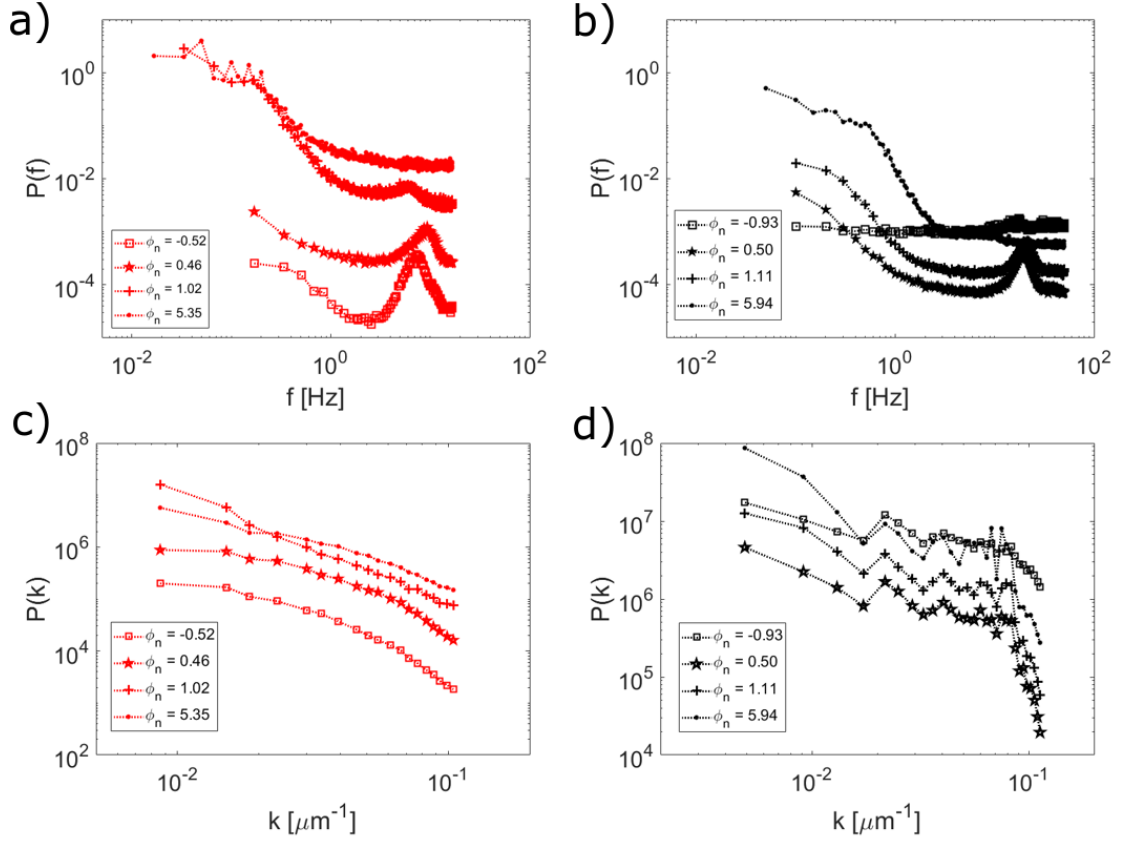
69

Figure 4.4: Power spectra in time and space are shown, where in the first one is possible to recognise the frequency peak of the flagellar beating for low sperm concentrations, which disappear at higher concentrations. On the space power spectra longer range of interactions can be seen appearing with increase of concentration.

### 4.3.3 Power Spectra

In this chapter we calculate two types of power spectra: frequency and spatial. The frequency power spectrum is calculated from the Fourier transform of the time signal of each point in the vector field. We define the 1D Fourier transform of the time signal $A(x, y, t)$ as:

$$X(x, y, f) = \int_{-\infty}^{+\infty} A(x, y, t) e^{-2\pi i f t} dt \tag{4.1}$$

For each point of the vector fields we obtain a Fourier transform that then we multiply by its complex conjugate to create the frequency power spectrum: P(x,y,f). Averaging then over space, we obtain the frequency power spectrum of each specific concentration, that then we plotted as shown in figure 4.4 a).

The sampling is important to avoid aliasing, the generation of a false frequency in addition to the right frequencies detected from the Fourier analysis. Aliasing is a phenomenon that appears in the discrete Fourier transforms. The sampling frequency is defined as $F_s = 1/T_s$

70

where $T_s$ is the sampling time, which in our case depends on the number of frames per second used to record the images $T_s = 1/\text{fps}$. But then a band limit has to be set for the sampling frequency while working with discrete signals. The sampling has to follow the Nyquist theorem of sampling, which stated that the sampling frequency has to include at least all the bandwidth of the signal in frequency, B. In other words, the best reconstruction of the signal is guaranteed in a band B such that $B \leq F_s/2$. Therefore, the upper threshold of the frequency range is the Nyquist frequency $F_N = Fs/2$.

Figure 4.4 a) shows the frequency power spectra averaged over space for both ram and bull samples. Only few concentrations are shown, in order to ease visualisation of the different behaviours of the power spectra at the various points of the transition from random to turbulent motion.

The second power spectrum calculated is the spatial one, in which we Fourier transform the 2D signal of the space for each time step of the vector field. We define the 2D Fourier transform of the signal $B(x, y, t)$ as:

$$X(k_x, k_y, t) = \int_{-\infty}^{+\infty} \int_{-\infty}^{+\infty} B(x, y, t) e^{-2\pi i (x k_x + y k_y)} dx dy \qquad (4.2)$$

We again multiply by the complex conjugate to create the spatial power spectrum and for each spectrum grid point the values are averaged over time. Then the wave vectors k have been computed as: $k_n = \frac{2\pi}{\delta} \frac{n}{N}$, where $\delta$ is the distance between all the N points in space and n is the considered point. After computing the wave vector k, the values of the same k have been averaged and then plotted as function of the wave vector. Figure 4.4 b) shows the spatial power spectra for few concentrations, so that it is possible to represent the different stages of the transition without crowding too much the plot.

## 4.4 Correlations

We desire to study the correlations of the data in both time and space, as we did with the power spectra. We then start with the autocorrelations, where we consider the time signal of each grid point in the vector fields. The autocorrelation is defined as the correlation between the signal A at time t, with the same signal at a subsequent time $t + \delta$, where $\delta$ goes from zero to the length of the signal T. Hence, the autocorrelation for the time lag $\delta$ is defined as:

$$r_\delta = \frac{c_\delta}{c_0} \qquad (4.3)$$

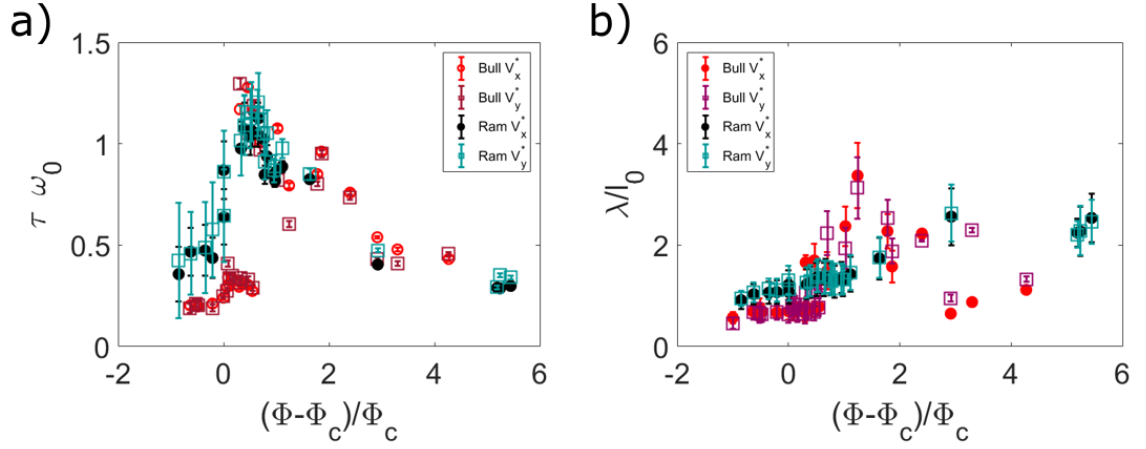where $c_0$ is the sample variance of the time series and $c_\delta$ is:

Figure 4.5: Correlation time and length are here plotted as function of concentration, with time correlation peaking just after transition and then decay, while space interactions increase with concentration.

$$c_\delta = \frac{1}{T} \sum_{t=1}^{T-\delta} (A(t) - \overline{A})(A(t+\delta) - \overline{A}) \tag{4.4}$$

The autocorrelation for all lags is calculated as stated in eq. (4.3) for all the points in space of the vector fields. The autocorrelation is then averaged in space per each time lag. To extrapolate the time scale $\tau$ of the interactions the curve has been fitted with a simple exponential function A: $A(\tau) = e^{-t\tau}$. The different correlation times $\tau$ have been normalised by the constant $\omega_0$ and then plotted as a function of the concentration, as shown in picture 4.5 a). The errorbars are calculated from the 75% confidence bounds of the exponential fit.

To calculate the correlation in space at each time step we use the cross-correlation function $c(\mathbf{r}, t)$ between two different points in the vector fields.

$$c(\mathbf{r}, t) = \frac{\langle V(\mathbf{x} + \mathbf{r}, t) \cdot V(\mathbf{x}, t) \rangle - \langle V(\mathbf{x}, t) \rangle^2}{\langle V^2(\mathbf{x}, t) \rangle - \langle V(\mathbf{x}, t) \rangle^2} \tag{4.5}$$

where $\langle \cdot \rangle$ is the average in space. For each distance $|\mathbf{r}|$ we average in time and then we an exponential function $C(|\mathbf{r}|)$ to extrapolate the correlation length $\lambda$: $C(|\mathbf{r}|) = e^{-r\lambda}$. The various correlation length $\lambda$ is firstly normalised by the typical single cell length $l_0$ and then plotted as a function of the concentration, see figure 4.5 b). As in the autocorrelation case, the errorbars are calculated from the 75% confidence bounds of the exponential fit.

## 4.5 Turbulent Fraction

After analysing the basic parameters, we decide to use a similar approach as explained in the simulation work [245], where they calculate the fraction of turbulent states in a channel filled with swarming bacteria. The aim is to calculate the activity of all the different space-time states and look how they evolve with the increase of concentration and mostly with the appearance of the turbulent state. In order to calculate the turbulent fraction (TF) quantity we need to start by computing the enstrophy field $\Omega(x, y, t) = |\omega(x, y, t)|^2$ from the vorticity fields. In the simulation work [245], since the system is asymmetric the enstrophy field is averaged over the short dimension of the channel. In this simulation the intention is to learn if in the long direction of the channel there are stable turbulent state that create vortices occupying the channel. In our case, the system is symmetric and circular, so we do not have a preferred direction, but similarly, we want to learn if there are turbulent structures in the system. Hence, we average the enstrophy field in both directions (x and y). If in the enstrophy fields there are local active turbulence domains, then the average fields will exhibit periodic oscillations in time. So, to localise those turbulence domains we study the average fields. We divide the time into n intervals of identical duration and the space is divided into the L points from the enstrophy field. We calculate the autocorrelation function, eq. (4.4), of the averaged enstrophy field for each point in space and each temporal interval. We are interested in the presence of periodicity in the autocorrelation function. We considered the autocorrelation in the time interval to be periodic if it has more than three peak that exceed a threshold set by the 95% autocorrelation function confidence bounds. In simulation work like [245] the size of the windows is chosen to be long enough to have at least five oscillations, to reduce the possibility to include both periodic and aperiodic intervals but long enough to be sure to detect periodicity of the autocorrelation. In our experiments, the recording time has been divided in enough windows to have enough statistic and in windows long enough to have two oscillations over the 95% confidence bounds, to assure the detection of periodicity, considered that our intervals are very shorts. The time intervals do not overlap, to avoid detecting the same oscillation multiple times. It is important to highlight that the ram experiment was conduced with a high speed camera recording at 100 frames per second, with a duration of 1000 images (except the last couple of concentration which were recorded for double the time). This allows us to have a signal long enough to detect the oscillations in a 1 second window, for a total of n=10 windows, which are enough to study the behaviour in the system. In the other dataset the frame rate is less than half, 33 frames per second, not favouring the choice of a 1 second length window. Therefore, the time window is chosen to be 2.3 seconds (75 images), giving enough points to compute the periodicity of the autocorrelation. In both datasets, the first concentrations have a shorter recording time, leading to not very
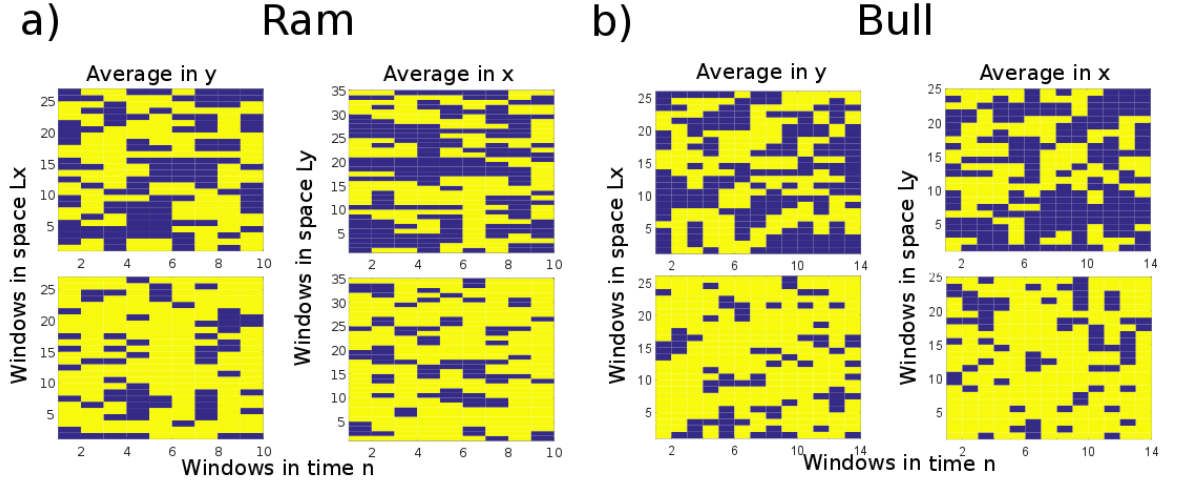
a) Ram  b) Bull

Figure 4.6: Kymographs of the turbulent fraction in x or y in time. The acrive states are shown in yellow and the inactive states, with value zero are shown in purple. In **a)** we are showing the ram turbulent fraction, the two top kymographs are for concentration $\phi_n \sim 0.33$ while the bottom two for $\phi_n \sim 1.63$. It is possible to see the increase of active states, in yellow, with increasing concentration. Similarly, in **b)**, we recognise the same behaviour in the bull sample. The top kymographs are at concentration $\phi_n \sim 0.31$ and the two bottom one for $\phi_n \sim 1.24$.

reliable statistics justifying the exclusion of those concentrations from the analysis.

So, after calculating the autocorrelation and checking if, in that space-time state, the auto-correlation is periodic, we assign a value, one or zero, to the space-time state s. To define an active turbulent state, said state has not only to be periodic in autocorrelation, but even have at least one neighbouring state, space or time, periodic. In case it is a single isolated state, it is rejected and set to zero. The resulting space-time kymographs are the plotted, as shown in figure 4.6, where yellow represents the active turbulent states with value one and the purple are the zero states.

From the kymographs, the turbulent fraction (TF) is computed as follow:

$$TF(\phi_n) = \frac{\sum s = 1}{L \cdot n} \cdot 100 \tag{4.6}$$

When the percentage of active states in the space-time kymograph is calculated, it is then plotted as a function of normalised concentration, as in figure 4.7.

The active state can be considered as to have the presence of an active turbulent vortex, which can either split, creating new vortices, or decay into a non-turbulent state. In fig-ure 4.7, for very small concentrations we have excluded the data from both bull and ram, since the recording times were short not providing enough data for a reliable statistics for the turbulent fraction computation. While reaching the critical concentration, the turbu-lent vortices appear and instead of having a balance between the turbulent vortices that
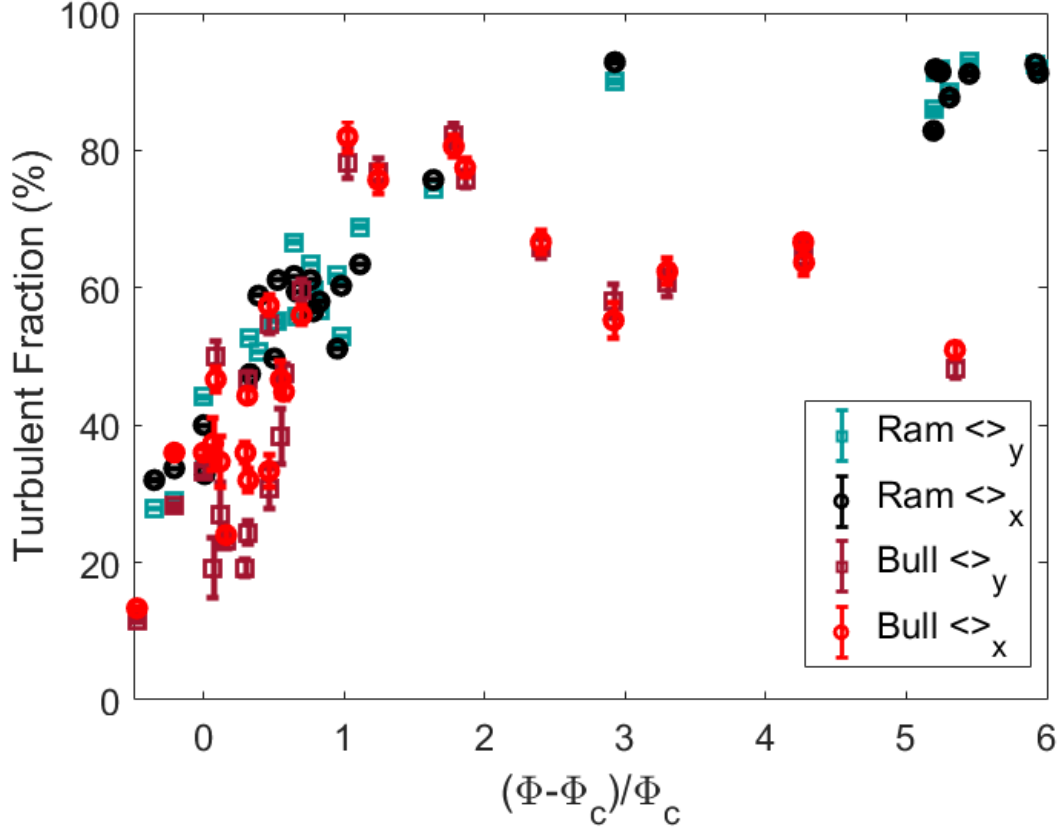
Figure 4.7: After the critical concentration the turbulent fraction appears to increase. The turbulent fraction is defined as the number of active states in the system. The increase of this quantity represents the appearance and persistence of active structures, like vortices, in the system.

split and decay, they do not decay quickly, but the vortices reach a steady state and split into two vortices, increasing the number of turbulent states. Further increase in concentration leads to a well-defined turbulent fraction, where the competition between division and decay of the vortices, creating a system with the majority of the system, up to 80 %, occupied by turbulent states. At high concentrations, the bull and ram datasets differ in behaviour. While the ram turbulent fraction increases and reaches a plateau, with turbulent values between 80% and 90%, the bull turbulent fraction decreases to values of 50%. From figure 4.6, but mostly from the values of the turbulent fraction in figure 4.7, we can see that our system is symmetric. In fact, the values of the turbulent fraction for both averaging cases, over x or y dimension, are very close between each other. For example, in case of the bull data we have: $TF_x(0.31) = 49\%$, $TF_y(0.31) = 47\%$, $TF_x(1.24) = 75\%$ and $TF_y(1.24) = 78\%$. For the ram dataset the turbulent fraction values are: $TF_x(\phi_n = 0.33) = 53\%$, $TF_y(\phi_n = 0.33) = 47\%$, $TF_x(\phi_n = 1.63) = 74\%$ and $TF_y(\phi_n = 1.63) = 76\%$.

## 4.6 Discussion

We have presented above the analysed quantities that we believe can describe the transition to collective motion. As shown in figure 4.2 a), for low concentrations, the velocities are low, of the order of the single cell swimming speed, while when the critical concentration is reached, the average normalised velocity increases rapidly, almost linearly for both datasets, up to 6 times the single cell velocity. This increase in velocity is considered to be due to the cell to cell interactions that create local alignment [104, 246, 247, 248, 101, 102, 39]. At high concentrations, the linear increase seems to stop and plateau. It is not sure if at a further increase in concentration, the normalised velocities would decrease. But since our system has been evolving autonomously, with the number of cells increasing in time without any interaction, we assume that the number of cells will saturate after a long enough time. In case of the ram samples, we can see this saturation more clearly. Indeed, the last three high concentration points in figure 4.2 a), have a $\phi_n \sim 5$, but those three points have been taken 30 minutes apart. This suggests that the concentration did not increase in over an hour and a half and the average velocities of the cells remain similar over time. Of course, if the times are too long, the cells will start dying and consequently the velocities, independently of the system concentration, will start decreasing.

Since sperm cells are pusher-like swimmers, we know that the fluid viscosity would decrease with increasing number of spermatozoa present [104, 246, 247, 248]. Moreover, some previous works on the motion of single sperm cells and clusters of cells [101, 102, 39], show an increase of the velocity in the system with increasing number of cells that would cluster and locally swim together. In case of wood mouse spermatozoa [101], the sperm cells clumps in trains from hundreds to several thousands cells. These trains have an average path velocity almost double than the single cell velocity. While the fishfly sperm move in clusters of hundreds of cells attached by the head [39]. In this work [39] it is shown that the velocity of the clusters increases with the size of the cluster itself: the larger the cluster, the faster it moves. Given these examples in the literature, we were expecting the sperm velocities to increase with concentrations, but we could not find previous works on sperm with velocity increasing as much as 6 times the single cell velocity and not with a linear increase of the concentration. Below the critical concentration, cells do not interact between each other and the resulting average velocity is close to the single cell velocity. At the critical concentration, the cells are in a number such that they have to interact between each other locally. With increasing concentration, the number of cells interacting should increase, increase the number of spermatozoa in the local cluster moving. Thanks to what stated in previous works [104, 246, 247, 248, 101, 102, 39] we can say that the higher the number of cells in the fluid, the higher is the number of cells interacting and the number of clusters increases the overall velocity of the cluster and hence of the detected velocities.

We then proceeded to look at the vorticity. The values of the vorticity shown in figure 4.3 a) are near zero up to the critical concentration $\phi_c$, after which the vorticity assumes non zero values. This quantity increases with concentration after the critical one, showing that more turbulent flows arise with the increase of concentration. After a first increase, the ram vorticity values in figure 4.3 a) show a rapid decrease that plateaus right away. Those vorticity values will remain fairly constant up to the highest concentration. While the bull data, will decrease further and drop to zero for a few concentrations after which they will plateau again at similar values as the ram data.

On the other hand, the values of the absolute vorticity in figure 4.3 b) show non zero values for concentrations lower that $\phi_c$, which implies that there are local alignments and inter-actions for low concentrations, at least at short times. These vorticity values increase with concentration, but the increase of the vorticity is faster after the critical concentration. No decrease in absolute vorticity can be seen after the critical concentrations as, on the other hand, is possible to see in figure 4.3 a). The ram absolute vorticity, in figure 4.3 b) seems to increase linearly and not plateau, as the bull data does. Indeed, the bull absolute vorticity data shows three different regimes, the first one before the critical concentration, where it increases linearly, the second is a rapid increase after the critical concentration, where the absolute vorticity seems to increase as a square root and the last regime is when the absolute vorticity seems to plateau after $\phi_n \sim 1$.

We interpreted these two vorticity plots as follows. For values below the critical concentration, the vorticity in figure 4.3 a) has zero values for both ram and bull while for the absolute vorticity in figure 4.3 b) the values are non zero. Hence, the non zero values below the critical concentration are due to summation of small but all positive values of vorticity that, as shown in 4.3 a) when their chirality is taken into account, disappear because they are random and cancel each other. After the critical concentration, the vorticity in both plots increases, since the motion is locally organised with the appearance of vortices and jets. In this case, the absolute vorticity plot (figure 4.3 b)) shows that for ram the local organisation increases linearly in concentration, summing up all the contributes of the structures independently of the chirality. When, on the other hand, we take into account the sign of the vorticity (figure 4.3 a)), we see that there is a peak at a concentration around $\phi_n \sim 1$, after which the vorticity values plateau, meaning that the structures present in the fluid that are summed up in the absolute vorticity, here cancel each other at least partially, but maintaining a constant temporary preferred sign of the vorticity. For the bull data, the increase in the absolute vorticity (figure 4.3 b)) is steeper and at the concentration of $\phi_n \sim 1$ it plateaus, while the vorticity (figure 4.3 a)) after the peak drops at values close to zero and then increases again. In this case, we interpreted that the fluid vortices and jets increases with concentration, but then since the sum of all the contributes without sign remain constant, when considering the sign of the vorticity, the smallest variation would

create a bigger fluctuation of the vorticity, as we can see in figure 4.3 a).

We then investigated the frequency power spectra, shown in figure 4.4 a). This plot shows a peak at high frequencies f ~ 10 − 20Hz, that are comparable to the beating frequencies of bull and ram sperm from other works [249, 250]. The contribution of the oscillating heads of the single sperm cells is present only for low concentrations, where the high frequencies peak is present. These high frequencies are lost for high concentration, were the long distance interactions are present and overtake the single cell contribution we can find for lower concentrations. In addition, we can notice that the power spectra in frequency has higher values for low frequencies, with a decay steeper for high concentration. This means that with increasing concentrations, the velocity signal has a longer interaction over time on the order of a few seconds, instead of having instantaneous interactions as in the case of low concentrations.

The second type of power spectra calculated is the spatial one, where the Fourier Transform is made over the 2D image for each time. The power spectra, figure 4.4 b), show a difference in slopes for low $k$ depending on the concentration, which suggest a long range interactions arising with concentrations that are not present for lower concentrations. While the slope for higher $k$ decreases slightly with increasing concentrations, suggesting vice versa, that the short range interactions reduce in power with increasing number of cells in the environment.

Realising that the power spectra were not giving us many quantitative informations on the space and time correlation length, we decided to compute the autocorrelations and cross correlations for each concentrations, resulting in the plots in figure 4.5 a) and b).

From the autocorrelation results, figure 4.5 a), we can see that the velocity signal for both ram and bull correlates weakly in time until the critical concentration. After the critical concentration is reached the system starts to correlate in time. There is a sharp increase in the correlation times, up to $\tau$ of around 1.2 s and then it decays smoothly. This correlation time variation can be interpreted as the system aligning and creating vortices and flow structures lasting in space for long times, while with increasing concentration the system results more active, reducing the length of the interactions in time. In this last case, the turbulent flow structures will be lasting for a short amount of time, continuously changing and creating and destroying the vortices.

On the other hand, results for the correlation length $\lambda$ are more complex, with very different dependence with $\phi_n$ for the two species. In the bull experiments, the correlation length sharply increases after the critical concentration and then again smoothly decreases, while the ram dataset has a continuous increase of the correlation length. Both dataset have the highest value of the spatial correlation at around 150 $\mu$m, 3 times the cell length.

Finally, we looked at the turbulent fraction. This quantity increases with concentration reaching a plateau for the ram experiment, similarly to the results from [245], while de-

creasing for high concentrations for the bull experiment. The turbulent fractions shows that the system has active states that are organised in space and time and that they increase with the concentration. The space is populated by an increasing number of vortices that finally populate almost all the space analysed and persist in space for longer times.

## 4.7 Conclusions

We performed a similar analysis as the one carried on for many bacterial systems with the aim of investigating the transition from random motion of highly diluted sperm samples to a collective motion behaviour, with turbulent flow, for high density sperm environment. The results of the analysed quantities allow us to say that a transition between random and turbulent motion appear with increasing concentration. The transition is smooth with concentration, but get triggered after a critical concentration is reached $\phi_C$.

We looked at samples from two mammalian species, ram and bull, that have in nature a different concentration, being higher in the ram samples, to the point that by the naked eye it is possible to see the swirls, jets and vortices just after collection. We investigated the correlation between cell density and the motion in bulk environment, where boundary conditions can be neglected. For very low concentration we saw just uncorrelated random motion, without clear spatial structures, aligned clusters or specific density aggregations. This random motion continued for increasing concentration up to a threshold. When the critical concentration is reached, the major flow variables increased sharply. The correlation lengths and time acquired non zero values and showed that the flow correlates for long times and for long range. These long range interactions created the macroscale structures we saw and result similar to the one seen for bacterial turbulence, with vortices and jets.

From all the informations discussed previously, we can conclude, that as expected the bulk environment a phase transition can be seen solenly by modifying the cell concentration and the turbulent state has many characteristics of the bacterial turbulence.

# Chapter 5

# Collective motion in confined environment – circles, rings, channels

## 5.1   Introduction

The aim of our following work is to assess how different types of confinement can influence the cell motion and the collective behaviour of a system of sperm cells. Studying the confinement conditions is very important when talking about sperm samples, given the characteristic of spermatozoa to swim sliding onto a wall [73]. They indeed use the same strategy when travelling through the female tract, with the risk of being trapped at a boundary of lost in a cavity of the tract. As it will be shown in this chapter, confinement helps the transport towards a final destination, but when the confinement is circular or ring-like, the system will stop moving forward and the resulting motion will be a circulation or oscillation inside the confinement. Hence, very tortuous tracts could result detrimental for fertility and forward motion.

The literature on confined sperm suspensions is not vast. One of the only and most recent works is by Creppy et al. [103], where manually diluted suspensions of active sperm cells have been introduced into a annulus-like structure and the motion under confinement evaluated. In this work a phase transition in the rotational motion appears with increase concentrations and a oscillatory dynamical rotations has been seen to arise for high volume fractions. Two oscillations have been found for high concentrations: a larger spinning period along the annulus of period 15 s circa and a superimposed typical secondary oscillation of period 3 s. For the diluted samples, the secondary oscillation is transient and after a few periods it decays.

As already said, the literature on sperm cells is very scarce, in fact, no other experimental works on spermatozoa in confinement have been found. Hence, the rest of the literature we will take into account for the confinement experiments is based on bacterial motion.

Confined bacterial suspensions have been seen to organise in single vortices inside a water drop in oil with diameter between 10 and 150 $\mu$m, leading to the consideration that spatial ordering of active vortices can be stabilised by the size of the system [251, 252, 253]. As shown in the previous works on bacteria under confinement [251, 253], when looking at drops with low concentration, the few cells present in the drop will swim along the boundary, circulating around with little interaction in between the cells. With increasing the concentration, the cells form clusters that will slide along the interface of the drop, with increasing the concentration further, the clusters merge and the boundary layer is created. This layer is formed of cells swimming along the boundary of the drop, the interactions between cells, make it possible to reorient the cells that are swimming in an opposite direction from the bigger clusters and after a transient all cells in the boundary layer are swimming in the same direction. This cells layer creates a flow going in the direction opposite to the swimming direction, since the swimmers are pushers. When the bacteria concentration is high enough that the all the cells in the drop can not be at the boundary, some more layers appear. The direction of these layers is defined by the steric interactions between cells. The final arrangement for a dense suspension is a spiral alignment, with all cells pointing in the same direction, namely pointing outwards, creating a strong flow that at the centre of the drop is strong enough to counterbalance the swimming speed. So that even if aligned as the boundary layer, the final direction of the bulk flow is opposite to the direction of the flow at the boundary.

A highly concentrated suspension of bacteria confined in a drop of diameter between 30 and 70 $\mu$m arranges as a single vortex occupying the entire space in the drop. This bacterial rotating system does not appear to have a preferred rotation: clockwise and counterclockwise vortices appear with equal probability [251]. For drops with diameter larger than 70 $\mu$m and smaller than 100 $\mu$m, the flow is still rotational near the boundary but moving towards the center the vortex order decreases [251]. Finally, for drop diameters larger than 100 $\mu$m, the flow inside the confinement is fully turbulent as in bulk suspensions [33, 117, 35, 36].

From those works we can consider that long range hydrodynamical interactions are at the basis of the stable circulations of a confined bacteria suspension. Moreover, the local cell to cell interaction makes the cells align locally, but the large scale behaviour under confinement appears when there is coupling between cell motion and the dynamics of the fluid.

In the work presented in this chapter we try to replicate these study, aiming to find the confinement limit for sperm cells at which single vortex circulation appears, remain stable and finally, at which diameter size, the motion of the sperm cells in confinement transitions from circulation to turbulence.

Additionally, from a recent work [252], it has been shown that for highly concentrated

bacteria suspensions confined in two connected circles, the relative distance between the centres of the two circles define the phase of circulation. A transition between two stable configurations appear: one configuration is defined by the vortices in the circles rotating both in the same direction, while the other circle has the vortices rotating in opposite direction. This phase transition, depends only on the geometrical conditions of the system, specifically in the relative position of the circles, corroborating the idea that geometrical conditions define the active ordering of confined bacterial suspensions.

## 5.2 Experimental Methods

### 5.2.1 Sample

The samples used for this analysis are ram samples treated as described in the previous chapter 4.2.1. Specifically, the ram samples are collected in loco, fresh in the morning from healthy animals. Experiments started right after collection and were carried on for a couple of hours, until cells were dead or enough data were taken. Only good quality semen was used for these experiments, using high concentration and high motility samples (between 4 and 5 value in the usual scale of evaluation). Usually the second donation of the day, half an hour after the first collection, was used. The samples were kept at room temperature, which was around 20 degrees Celsius at any time. Usually the original sample was kept undiluted or diluted at a ratio 1:1 with a specific solution composed of tetradyl, egg yolk and DI water.

### 5.2.2 Experiments set-up

The PDMS chambers are pre-filled with buffer solution. Pictures of the different devices are shown in figure 5.1, where it is possible to see the different size circles, the connected circles, the rings and finally the straight channels connecting two large pools.
All the devices in this chapter have a height h ~ 150$\mu$m. The circles shown in figure 5.1 a) have radii between 50 and 500 $\mu$m, all the connected circles in figure 5.1 b) have a radius of 200 $\mu$m and the rings (figure 5.1 c)) have a variable width, but their outer radius is 250 $\mu$m. The channels shown in figure 5.1 d), have a total length of 1.5 cm reservoir to reservoir and a variable width. The recordings are made with a CCD camera, in the circles experiment the frame rate was set to 33 fps for a maximum of 10 seconds, while for the rest of the experiments, low speed recordings were carried, in this case, the frame rate was set to 10 fps for a maximum of 2000 seconds. All the experiments were performed with a 4x magnification, with the exclusion of the channels and transport experiments, for which a 2x lens has been used. Bight field imaging has been used for circles, rings and transport
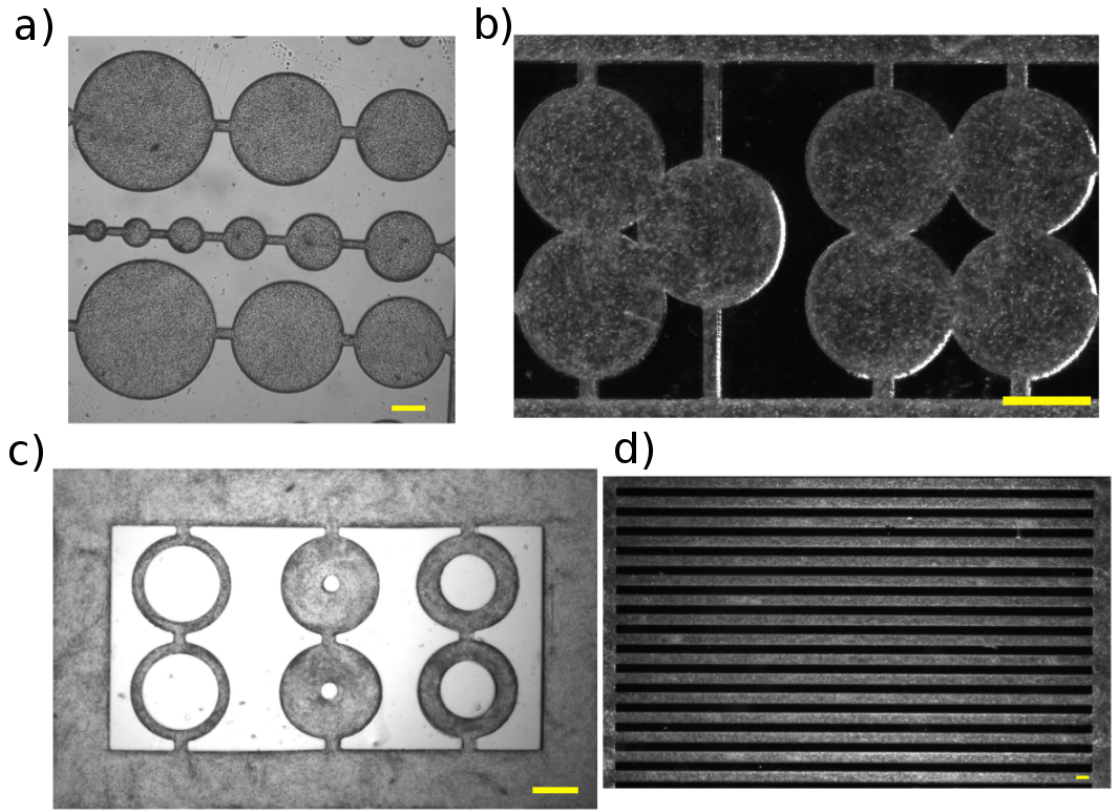
Figure 5.1: Pictures of the four devices used in this chapter. Firstly the central part of the circle device, showing the range of radii considered. Secondly, the center of the device with the two type of connected circles: and asymmetric design, with three circles and a symmetric one with four. Thirdly, the rings or doughnut shape devices and finally the straight channels connecting the two reservoirs. The scale bars are 250 $\mu$m in all panels.

data acquisition, while dark field for the connected circles and the oscillatory channels has been used. All experiments have been carried at ambient temperature ($\sim$ 20 °C).

The samples are introduced in the external ring of the PDMS channel, for the first three devices, in such a way the only section with cells is the external one, giving motile cells the possibility to swim into the central channels of the device, increasing the concentration in loco with time. The cells arrive in the central chambers with time, depending on their starting position in the outer ring, their direction and their speed. The spermatozoa will be trapped in the central channels thanks to the channels connecting the loading ring to the central part. Those channels will redirect towards the centre the swimming sperm cells that try to escape. This technique is used for the rings, the circles and the connected circles but not for the straight channels, which only have two big pools from which the swimming cells will go to narrow channels.

### 5.2.3 Analysis

As in the previous chapter 4.2.3.2, the velocity fields are calculated through PIV analysis thanks to both costume made and provided programs from MATLAB (Mathworks Inc. USA), specifically the PIVlab package [214].

## 5.3 Circles Experiments

This experiments and analysis have been inspired by previous work on bacteria under confinement [251], where experiments and simulations have been combined to explain the behaviour of bacteria, hence pusher like cells, in a confined environment, a water drop in oil.

We aim to investigate the system of sperm cells, confined in circular chambers with radii that vary from 50 $\mu$m to 500 $\mu$m in which the concentration increases in time, using a spermatron-like device, as in the device shown in figure 4.1, that directs progressively motile sperm cells towards the centre of the device. This will allow us to study the change in various quantities as: velocity, vorticity and vortex order parameter (see section 5.3.2.1) for increasing concentrations and radii at the same time and with the same sample.

### 5.3.1 Device and analysis

Figure 5.1 a), shows the device used for this experiment. The concentrations are numbered from 1 to 17 and they are assessed by counting cells in a reference chamber. Our estimation of the initial concentration $C_{\#1} \sim 3 \cdot 10^3$ cell/ml, for then having a linear increase in the concentration from $C_{\#2} \sim 5 \cdot 10^6$ cell/ml to $C_{\#17} \sim 7 \cdot 10^{12}$ cell/ml.

### 5.3.2 Results

The quantities analysed are the angular velocity, the vorticity and the vortex order parameter. All of these quantities are calculated from the PIV velocity fields.

#### 5.3.2.1 Vortex Order Parameter

In order to quantify the spatial ordering inside the circles and specifically to distinguish if the motion in the circles is a single vortex rotating or a turbulent motion the vortex order parameter, VOP, is calculated:

$$VOP = \frac{1}{1 - 2/\pi} \cdot \left( \frac{\sum_i |\mathbf{v}_i \cdot \mathbf{t}_i|}{\sum_j |\mathbf{v}_j|} - \frac{2}{\pi} \right) \tag{5.1}$$
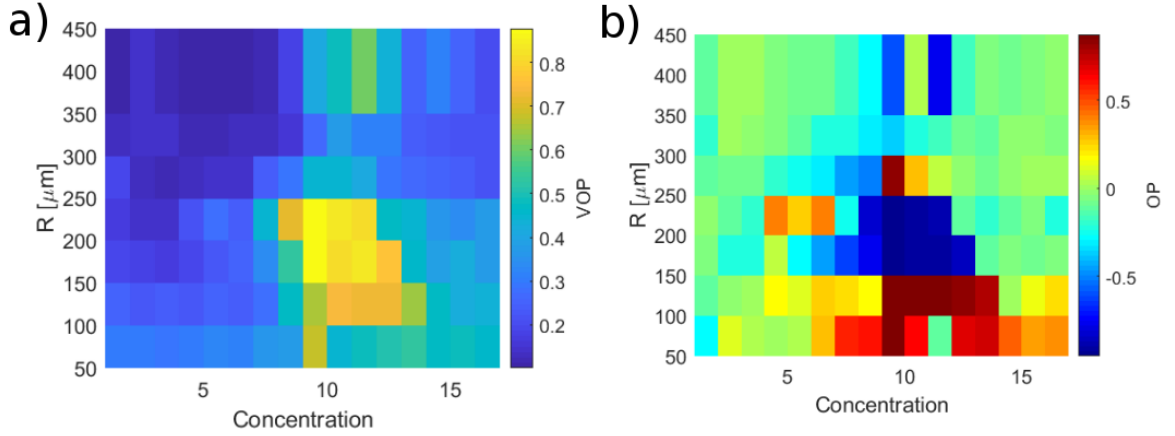
Figure 5.2: Plots of the vortex order parameter. **a)** Shows the color map of the vortex order parameter (VOP) variation with concentration and radius of the confinement. While **b)** is the color map of the order parameter (OP) with respect with radii and concentration.

where $\mathbf{v}_i$ are the velocities and i the points in time and space calculated from the PIV analysis and $\mathbf{t}_i$ is the azimuthal vector calculated for each velocity point in time and space. The vortex order parameter will acquire the value 0 if the motion inside the circle is chaotic and will be 1 if the motion is an azimuthal rotation, hence a single vortex rotating. In case of negative values of the order parameter, the motion will be a radial flow inside the circle. This order parameter, does not distinguish between clockwise and counter-clockwise rotation of the vortex. To account for the direction of the rotation, the order parameter, OP, is calculated as:

$$OP = \frac{\sum_i \mathbf{v}_i \cdot \mathbf{t}_i}{\sum_j |\mathbf{v}_j|} \tag{5.2}$$

Using the order parameter it is possible to look at what type of motion is present in the different circles at different times and define if the circulation is clockwise (+1) or counterclockwise (-1). The OP shown here in figure 5.2 is the representation of a single set of concentrations and radii, while the VOP, figure 5.1, is the result of 4 different repetitions of concentration and radii.

In figure 5.2 a) it is possible to see that for concentrations lower than $C_{\#6} \sim 10^8$ cell/ml and radii smaller than 150 $\mu$m, the VOP values are between 0.3 and 0.4, which we interpret as the number of cells in each circle is enough to populate the entire boundary layer and create a locally coordinated motion, rotating altogether. For largest radii, the sperm population at the boundary is not enough to have any overall coordinated rotational motion. With an increase in concentration, the cells start filling the smaller chambers, reaching a concentration where the orientation and motion of the cells is organised and the confinement is small enough to allow the circulation to be coordinated in the whole chamber,

creating a single vortex that rotates stably.

From figure 5.2 a), we can see that for the smaller radius, $50\mu m$, the VOP does not exceeds 0.6. If we consider that the radius of the chamber is comparable with the length of the sperm cell, then we can assume that the cells will be result close enough to interact strongly. Physically their head will hit each other, leading to cells scattering, but since the environment is so small, they will interact and scatter almost constantly. Additionally, their tails could interact by touching and disrupting they beating of neighbouring or opposite cells. All these physical interactions will disrupt instantaneously the circulation. Moreover, in case they are not close enough to touch, but still close enough to interact by the flow the pusher swimmers create. As explained in Chapter 1, the pusher swimmers create a dipole flow field around them, pushing the fluid behind them. This flow interacts with the neighbouring cells and in case of such a strict confinement, the flows interact in a destructive way for the alignment. Hence, it is possible to see how the cells are able to align locally and swim for short amount of time at the boundary, but then the alignment is broken, not allowing a single vortex to be created, not even in case of higher concentrations. Even if slightly higher values of vortex order parameter are present when the concentration is between 10 and 14.

At radii between $80 - 250\mu m \sim 1.6 - 5l$, where l is the length of the sperm cell, the low concentration values for vortex order parameter are decreasing from the values of the $50 - 80\mu m$ circles, reaching a vortex order parameter of value lower than 0.2. This means that there is no alignment in the circle. In the same way, the order parameter does not show any directionality for the rotation, having a value around 0 and never exceeding 0.2. The reason why there is no organisation at low concentrations is simply that the cells are not enough to interact and create at least a boundary layer with coherent circulation. With increasing concentration the circles with radii between $80\mu m \sim 1.6l$ and $250\mu m \sim 5l$ have the highest increase in vortex order parameter. They reach maximum values between 0.75 and 0.85, between concentrations 8 and 14, showing that in these ranges of sizes and concentrations, the environmental conditions allow a stable circulation of the swimmers inside the circles. The rotation of the circles in this range of radii and concentrations is either clockwise or counter-clockwise without any preferred direction, as shown in figure 5.2 b). If we look at the average rotation per radius in the showed data (figure 5.2 b)), there is a bias for the area with high values of vortex order parameter and order parameter, either clockwise or counter-clockwise, showing that circles with similar radii tend to keep the direction of the circulation, in average, with increasing concentration. For example, the order parameter for radii between $100\mu m$ and $150\mu m$ and all concentrations, the average rotation is clockwise, while in the next radii range, between $150\mu m$ and $200\mu m$, the rotations for all concentrations are mostly counter-clockwise. On the other hand, looking at the distributions of all rotational directions, it is possible to see that there is a bias, mean-

ing that a higher number of circles are either rotating clockwise or not, but there are circles in the same range of radii that are rotating in both directions. Indeed, for values of radii between $80 - 150\mu$m the order parameter values at high concentrations are either higher than 0.5 or lower than -0.5, showing that there is no preferred rotation. For higher radii, between $15 - 250\mu$m, there is a slight bias towards counter-clockwise rotation, even if the order parameter values still reach 0.5. With increasing concentration over 14, the vortex order parameter decreases to values around 0.5, showing that when the number of cells is high, the interactions between swimmers, specifically at the boundary, disrupt the circulation and have for the highest concentrations, a turbulent motion without a single vortex present in the circle.

Increasing further the circle size, there is no stable vortex circulation at any specific concentration. The highest value for the vortex order parameter is around 0.5 for concentration 11-12 for the largest radius size. With increasing concentration the active cells create a turbulent flow, where no overall vortex is present, but little vortices and local alignment are present.

#### 5.3.2.2 Velocity

The speed is calculated as in Chapter 4, using the x and y components of the velocity at each point of the circle, the average speed per radius has been computed in addition to the radial velocity at the boundary.

The speed increases with both concentration and radii of the chamber, without any clear correlation between the increase in speed and the increase of the measure of order in the system. Specifically, the presence of a single circulating vortex, as shown in fig. 5.2 a), does not influence the increase of the cell velocity. The increase depends only on the circle radii and the concentration, without correlating with the orientational order. Looking more closely at the dependences, we can see that the velocities lower bound per radius is defined by the velocity at lower concentration, which is understandable, but this lower bound depends on the radii. Indeed, it increases with increasing radius of the circular chamber, see figure 5.3 a). If we then concentrate on the same radius and we look how the velocity increases with concentration, we can notice that the jump between the velocities at the lowest and highest concentration, depends on the radius, fig. 5.3 c). For small radii, the jump is very small, while for the highest one the jump between the velocity in the circle at low and high cell concentration is more than double of the jump for the lower radii values.

For every single radius the velocity increase after a concentration higher than 7, which is consistent with what we have seen in a bulk condition in chapter 3. After the transition point at concentration 7, the increase of the velocity is a power law depending on the
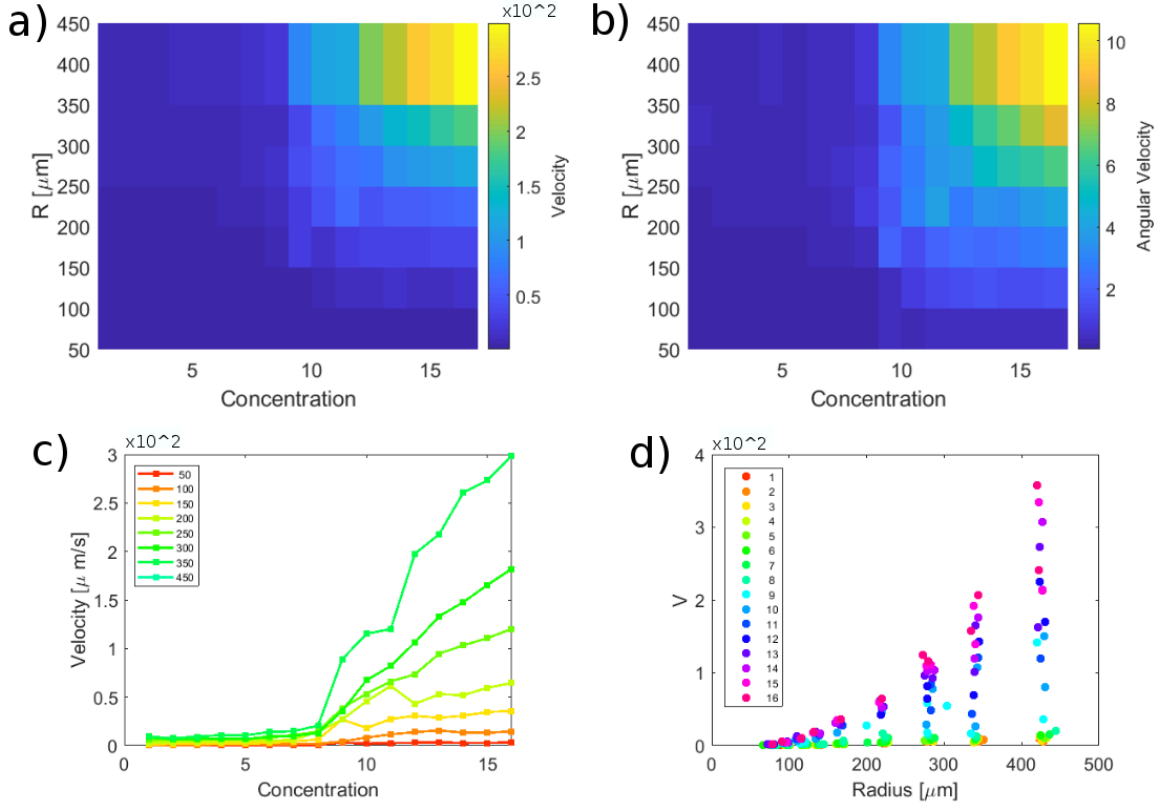
Figure 5.3: Velocity and angular velocity are here plotted as function of both confinement size and the concentration of cells. **a)** shows the average linear velocities recorded in the circle at different concentrations and in different circles. It increase with the same trend as the angular velocity, shown in **b)**. We then show in **c)** the relation between velocity and concentration per radius only for the average linear velocity, considering that the angular velocity will behave similarly. Finally we have **d)**, where the velocities are plotted as function of the radii at different concentrations.

radius of the circle. On the other hand, the increase of the velocity, depending on the radius for each concentration is a simple power law, without any transition point at any radius.

Finally, the angular velocity behaves similar to the flow speed inside the circles.

### 5.3.2.3 Vorticity

The vorticity measures the local spinning motion, which is conceptually different from the vortex order parameter. The absolute vorticity of the system is very different from the vortex order parameter. The absolute vorticity does not distinguish the direction of the rotation, only if there is local spinning near the point. As shown in figure 5.4 a), the absolute vorticity $|\omega|$, has a transition point at concentration higher than $C_{\#7} \sim 5 \cdot 10^9$ cell/ml, as for the velocities, but instead of steadily increase, there is a peak and a reduction of vorticity after concentration 12, and the increase depends on the circle size. The highest values
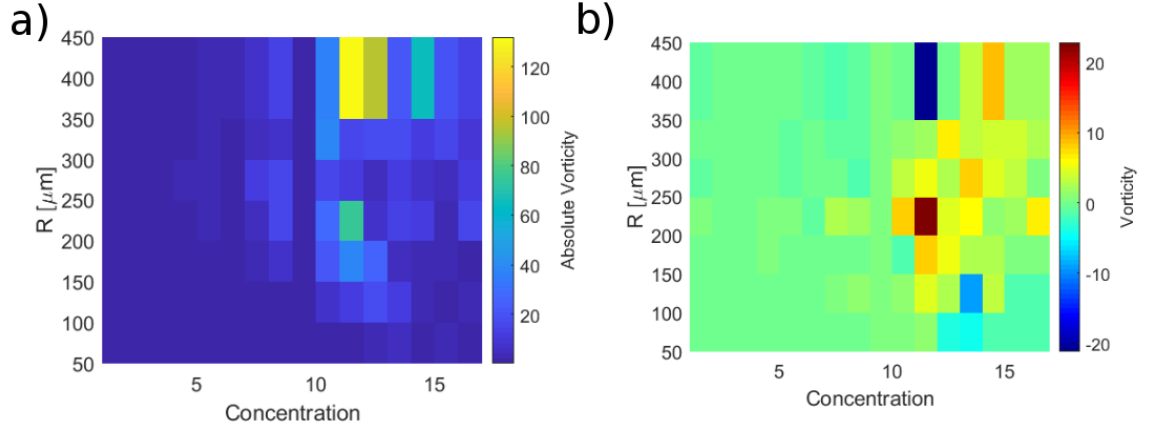
Figure 5.4: **a)** shows the color plot of the absolute vorticity with respect of both radii and concentration. While **b)** is the color plot of the vorticity variation with respect of both radius and concentration.

are for the largest circle size (R ~ 430$\mu$m), where the absolute vorticity reaches its maximum at concentration 13. On the other hand, looking at the dependence on the radius, at fixed concentration, there is a slow increase, with a peak for a range of concentrations in two radii regions, the 100 − 250$\mu$m and the 300 − 450$\mu$m circles. Hence, two regions in the radii-concentration plane appear, one at 100 − 250$\mu$m radii and 10 to 14 concentrations, which correspond to the golden area of the vortex order parameter, and the second one is at high radii, 350 − 450$\mu$m and concentrations from 10 over, which corresponds with the high velocity values. It is possible to interpret the first range as the region with stable vortex, while the second one correspond to high velocities and high local organisations, where turbulence is present assuring local swirling and organisation, but not long range alignment and hence no single vortex rotating.

The vorticity $\omega$, distinguishes between the two possible directions of rotation. It is difficult to recognise a specific pattern in the color-plot in figure 5.4 b), hence looking at the single distributions of the vorticity at fixed concentrations or radii is quite important. First of all, looking at the fixed radii situations, the vorticity start increasing after concentration 6 and then peaks around concentration 10. The vorticity changes the preferred local directionality with concentration and time. Hence at high concentration it is easier to distinguish what direction the local swirling is taking, while for low concentration the motion is on average not locally organised even for small circles. The distribution of the vorticity values with radii is more complex. The low concentrations the vorticity has values around zero, but for medium-high concentrations the small circle, R ~ 50 − 150$\mu$m, have values for the vorticity that are mostly negative, leading us to assume it is a clockwise preferred local rotation, which relates to the order parameter values, while increasing radii, R ~ 150 − 350$\mu$m, the preferred local rotation seams to be counter-clockwise, with a small

decrease with increasing size of the circles. The largest size circle, has high values of the vorticity, spread around positive and negative values, allowing us to say that for the highest velocities, the turbulent motion at high velocity is locally aligned and spinning, but only locally, which is seen comparing the order parameter values at that radius and concentrations.

## 5.4 Oscillations in Systems: Circles, Rings and Channels

### 5.4.1 Connected Circles

After looking at single circle behaviour, we decided to investigate how sperm cells behave in a more complex environment at high concentration, with three or four circles connected to each other. Regarding the device their preparation and the method of usage are the same as in the previous experiments. Moreover, the PIV analysis is again the same as for the previous experiments.

As in some of the bacteria work, multiple stable modes for the rotation of four connected circles have been found [252], depending on the distance between the centres of the connected circles. In our case, we do not change the distance between the centre of the circles, but we maintain that constant and change their positioning, the device used is shown in figure 5.1 b). The symmetrical system has four connected circles, which centres are positioned at the corners of a square, while the asymmetrical one has three connected circles which centres are positioned at the corners of an equilateral triangle (see figure 5.1 b)).

Let's consider first the symmetrical system. In previous work [252], there are multiple stable configurations for a symmetrical system of highly concentrated bacteria, quite the opposite in our symmetrical system. Indeed, for a dense suspension of sperm cells, we found that the stable configuration of the symmetrical four circles system, is the one with a same direction of rotation for the circles which centres are positioned on the diagonals of the square, hence top right-bottom left and top left-bottom right (see figure 5.1 b)). Here, the vorticity has similar values, but most of all has same sign and same direction.

As shown in figure 5.5 c), an important feature we observed is that this system oscillates, the connected circles do not stably rotate in the same direction, but they change direction of rotation and the system returns to the stable configuration very quickly. This oscillation happens naturally without any external input, showing a very stable and self-adjusting system. The diagonally connected circles have very similar values of vorticity (see figure 5.5 c)) and they pair up quite consistently with the other diagonally connected one. Looking at the velocity in figure 5.5 b), when the inversions of motion appeared, we can see that the flow slows down at the time of the inversion, from second ~ 800, dropping at the first perturbation and then slowly regaining speed with the increase of stability, resuming
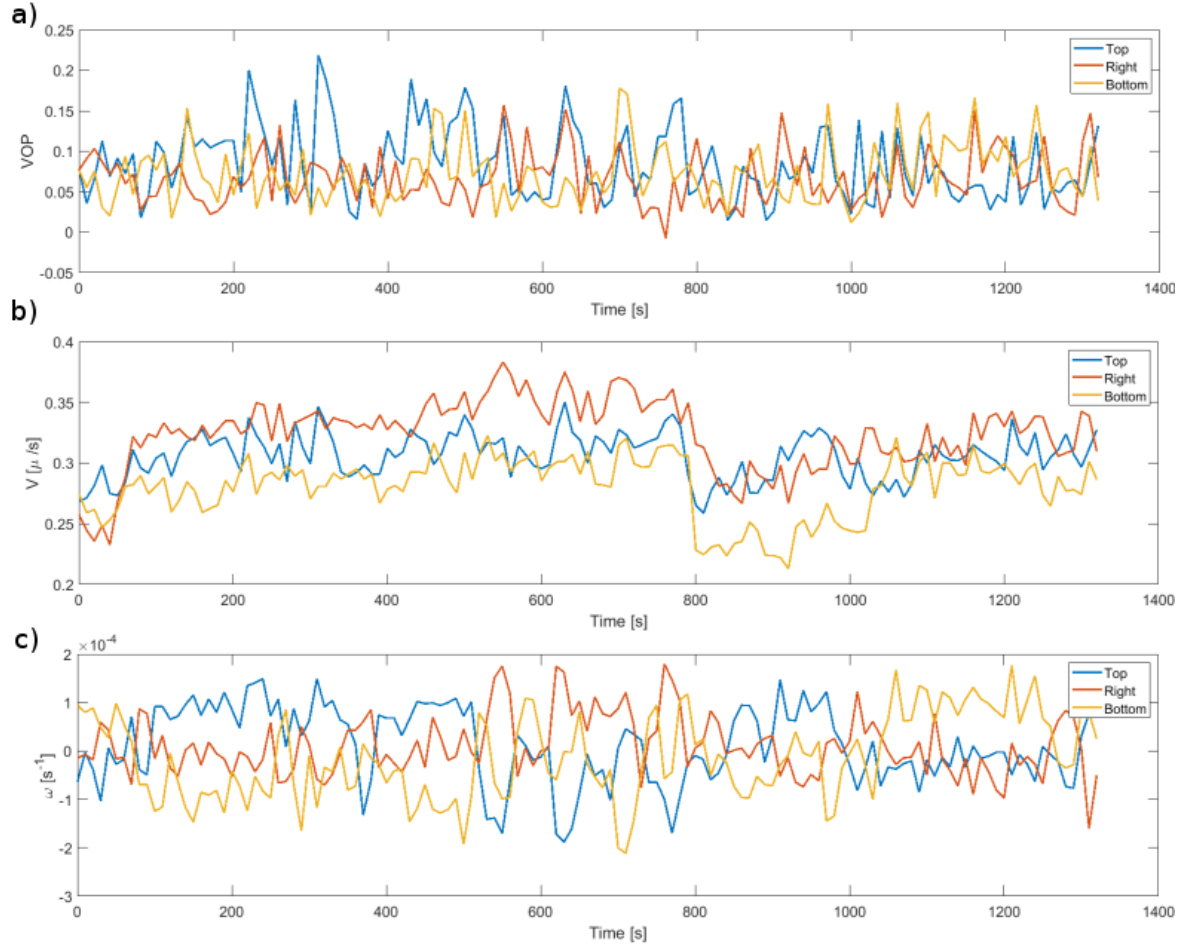
Figure 5.5: Plot of **a)** vortex order parameter, **b)** angular velocity and **c)** vorticity in case of four connected circles. Here the symmetry of the system allows the circles to rotate in a specific direction and when perturbations lead to changes in the rotation of one or more circles, the system adapts going back to an organised circulation. The organisation at stable condition is coordinated diagonal rotation and counter-rotation for perpendicularly and in parallel.

similar values after second ~ 990.

Finally, looking at an asymmetric design, with three circles connected to each other. In this case, as we can see in figure 5.6, few temporary correlations occur, but the asymmetry of the system disrupts these correlation quite fast. From figure 5.6 c), we notice that two of the three circles rotate in opposite direction with the third one oscillating between the two modes. No specific pattern can be seen in this system.

Figure 5.6: Plot of **a)** vortex order parameter, **b)** angular velocity and **c)** vorticity in case of three connected circles. The asymmetry in the system reflects on the unequal oscillations between of the parameters with respect to the other circles of the system.

### 5.4.2  Rings

Intrigued by this oscillating systems, we looked at doughnuts or ring shaped devices. Maintaining the outer radius the same, $R_{out} = 250$ $\mu$m, we looked at three different variation of the ring size, changing the inner radius $R_{in}$ = 195, 130, 35 $\mu$m, giving a final rings width of 55, 120 and 215 $\mu$m. We again looked at the average angular vorticity in time, figure 5.7 b), which shows very short time oscillations, which are consistent and stable throughout all the time of the experiment. We calculated the time power spectra of the system, as shown in figure 5.8 extrapolated the oscillation frequencies for the different width of the doughnuts. Here we can see that the thinnest rings do not show a clear peak in the power spectra (figure 5.8 a)), but the $\sim 120\mu m$ and $\sim 215\mu$m rings show two distinct peaks (figure 5.8 b) and c)), in the first case at frequency $\sim 0.05$ Hz which corresponds to around 20 seconds, while the larger rings show a peak for frequencies around $\sim 0.09$ Hz corresponding to 11
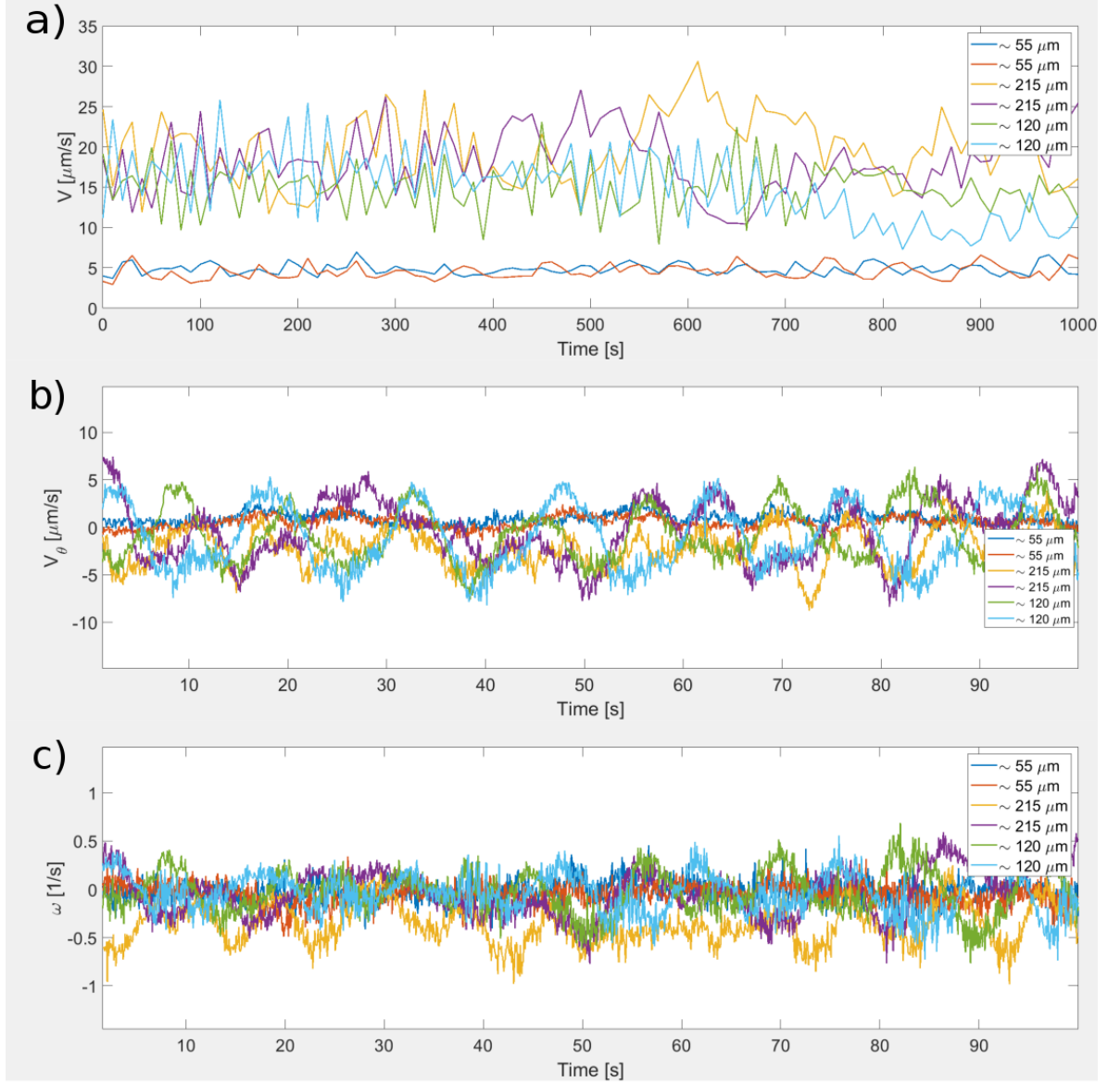
Figure 5.7: Firstly, **a)** shows the average over 10 seconds of the values of the velocity for a long time (1000 seconds), while in **b)** and **c)**, the non modified signal in a shorted amount of time are plotted, with the aim of showing the natural oscillations of the system.

seconds.

We can hence see that the velocities in figure 5.7 a), for the $\sim 55\mu m$ width rings have very low values, while for the thicker doughnuts the velocities are remarkably higher. The same can be said for the angular velocity (figure 5.7 b)) that is considerably smaller for the thinnest rings. On the other hand the oscillations of the angular velocity are easily noticeable, some perturbations disturb the regular oscillation but the system quickly recover the oscillation and the frequency of oscillation, that looks like to be around 15 seconds peak to peak. More difficult to interpret is the vorticity, which shows oscillations but they are
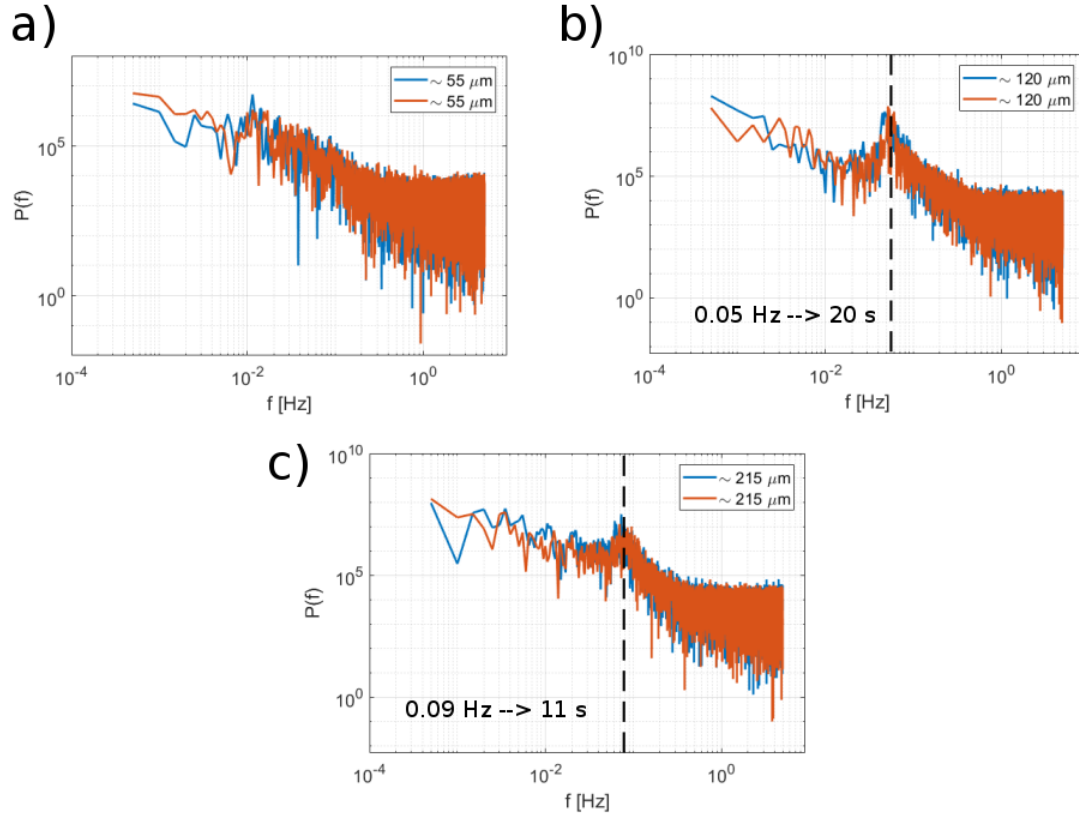
Figure 5.8: From the angular velocity the frequency power spectrum is calculated. **a)** Shows the power spectra of the rings with width ~ 55$\mu$m where no clear peak appears. While in **b)** the power spectra of the rings with width ~ 120$\mu$m show a peak for frequencies around 0.05 Hz, which gives a period of around 20 seconds. Finally **c)** shows the power spectra for the ~ 215$\mu$m thick doughnuts, where the peak is at frequencies of around 0.09 Hz, corresponding to a period of ~ 11 seconds.

not as well defines as the one for the angular velocity. This is probably due to the fact in the real system no proper vortex arises, but there is in the thickest doughnut some turbulent characteristics in the bulk, while the overall system at the boundaries is rotating. Similarly the vortex order parameter for the rings shows oscillations, see figure 5.9. When the system is about to invert the rotation, then the motion inside the device is not unidirectionally rotating, but the motion is more turbulent and chaotic, reducing drastically the values of the order parameter. It can be noticed that the oscillations of $V_\theta$ and OP are not fully matching. This can be explained by the fact that the system does not instantaneously change from circulation to chaos, but will transition, with reduction of velocities but still rotating, which result in the reduction of angular velocity but not on order parameter. Consequently, when the system is in the process of changing the direction, its order parameter is not zero, but the velocities have drastically reduced.

Finally, these oscillations looks very robust with time, persisting for long times, over 1000 seconds.
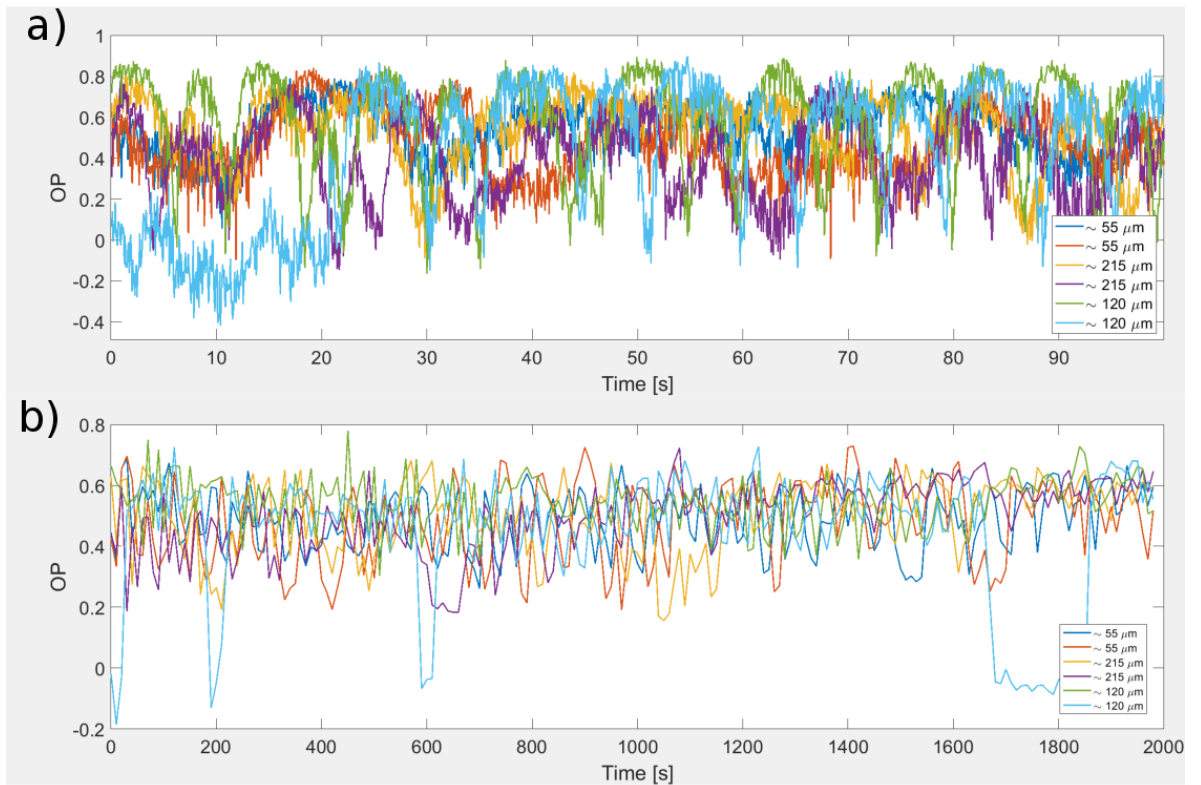
Figure 5.9: The order parameter for the different size doughnuts. **a)** shows only the first 100 second for the not averaged data over time. While **b)**, is from the full dataset order parameter values, but averaged over 100 frames (10 seconds).
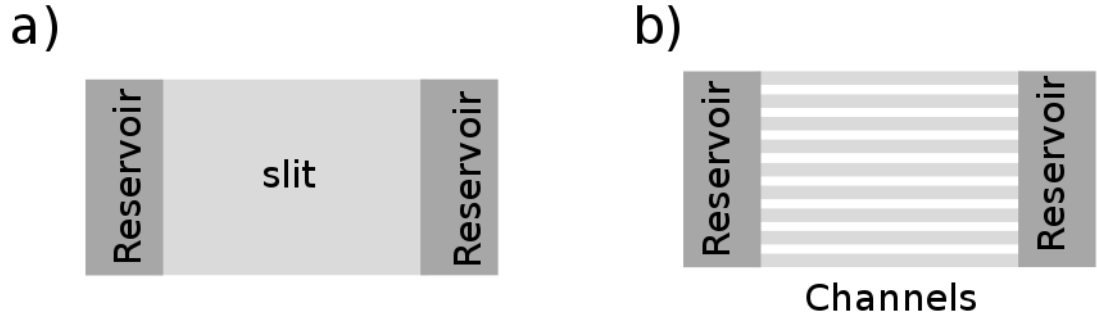
Figure 5.10: Schematic of the two types of devices used in this experiment. **a)**is a channel as wide as the pools that we can call "slit". In both devices the distance between the reservoirs is 1.5 cm, the reservoirs are 200 $\mu m$ thick while the channels are 100 $\mu m$ thick, while **b)** shows the device with multiple channels that can have different width.

### 5.4.3 Channels

Interested by these oscillatory motions, we designed a system shown in figure 5.10 b). This system is composed of multiple straight channels of variable width connected between each other by two big pools at the two extremes. The channel widths used are 100, 150 and 200 $\mu$m, while their length is maintained constant at 1 cm.

We did not only look at the undiluted sample regime, with concentration $\sim 5 \cdot 10^9$ cells/ml, but we progressively diluted the samples up to 16:1, which is the lower concentration and is equal to $\sim 3.2 \cdot 10^8$ cells/ml.

Looking at the velocities in the different channels, we saw that the direction of the velocity in the channels will reverse in time with a periodicity that varied with width of the channel and concentration of cells. In figure 5.11 a) and b) we show different examples of colour plots, where it is possible to see the reversal of the velocity direction. The signals of each single channel, can be analysed separately in time, calculating the wavelength and the amplitude of the oscillatory signal in time. The average of the wavelength and amplitude for width of the channel and concentration are shown in figure 5.11 c) and d).

We noticed changes in the frequency and amplitude depending on the width of the channels and the dilution of the sample. Unfortunately the data do not seem to follow a very understandable relation. The amplitude of the oscillations looks to increase with width of the channel for the high concentrations, but we can not distinguish any particular pattern or relation. Looking at the wavelength of the channel signals, we can see that almost all the dilutions, except dilution 8 and dilution 2, have a higher value on the 150 $\mu$m channel, while dilution 2 has the maximum for the wider channel, 200 $\mu$m. The amplitude seems to reduce with width of the channel only for dilution 1, while for all the other concentrations the amplitude increases with channel widths. Dilution 2 has the highest amplitude values overall concentrations, reaching the maximum for the 200 $\mu$m channel.
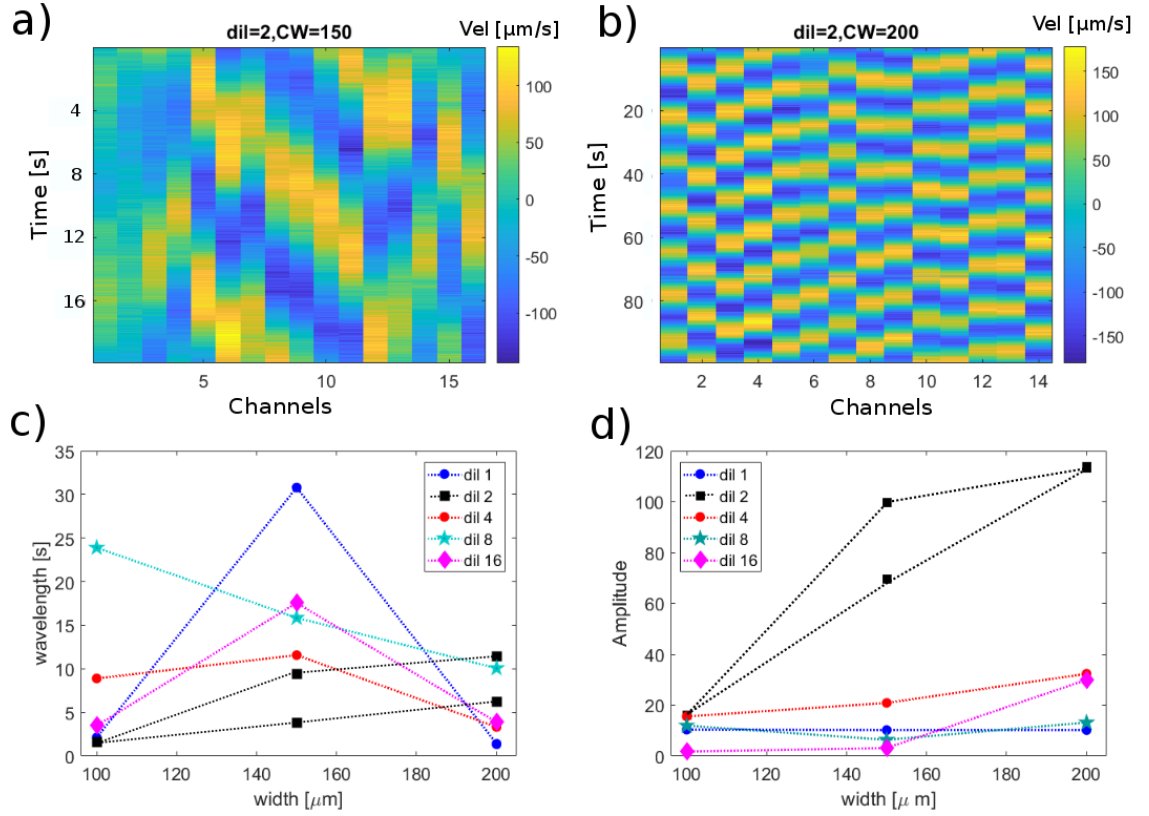
Figure 5.11: Two examples of the velocities colour plots. **a)** is for a dilution 2 and channel width 200 $\mu$m, while **b)** is for dilution 2 again, but the channels of width 200 $\mu$m. Wave length **c)** and amplitude **d)** of the oscillations in channels of different width and for different concentrations.

### 5.4.4 Transport

Using the devices shown in figure 5.10 we tried to investigate how fast the sperm cells will travel across a fixed length in different conditions. We investigates three different conditions: undiluted sample and channels, figure 5.10 b), undiluted sample and "slit", figure 5.10 a) and diluted sample and channels, figure 5.10 b). The devices used are shown in figure 5.10, both of them have two reservoirs, but only one of them will be filled with sample, while the other one will be left only with clear buffer. The central part of both channel is 1 cm long, but the device shown in figure 5.10 b) is made of 150 $\mu$m wide channels, while the other device in figure 5.10 a), called "slit", has only one channel which is wide as the entire reservoir. We want to see what is the most efficient environment for transport of spermatozoa from one reservoir to the the other. We decided to calculate how many cells will travel and populate the empty reservoir in 40 minutes. In order to define the amount of cells travelling across the device, we considered that the light intensity of an area in each frame of the video depends on the amount of cells present in the considered area. So, considering the maximum number of cells that can to travel to the empty reservoir as
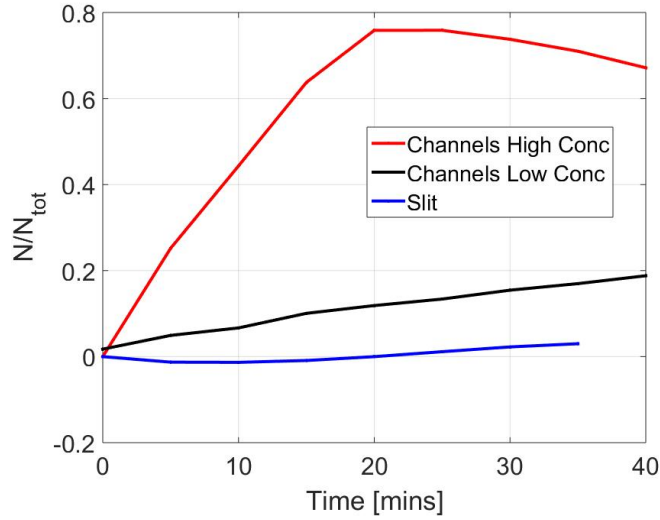
Figure 5.12: The number of cells arrived on the second reservoir is normalised with the total number of initial cells from the first pool, then plotted with respect of the time. For both high and low concentrations the best method of populating a far away zone is to have multiple channels instead of a flat open surface.

the number of cells present in the loading reservoir, we calibrated the total number of cells in the volume, $N_{tot}$ from the loading reservoir light intensity. We then pictured the empty reservoir and, in the same area, calculated the light intensity, which will be $N \leq N_{tot}$. When $N = N_{tot}$ it means that the light intensity of the area is the same as the loading one, which is the representation that all the cells travelled to the other side of the device. We plotted the ratio between the cells present in the empty reservoir over the total number of cells loaded against the time passed since we loaded the chamber.

Looking at the results in figure 5.12, we saw that for the slit device, the number of cells travelling to the empty reservoir is almost null, even if the loaded sample is the same high concentrations used for the channels high concentration (red line in figure 5.12). For low concentrations and channels in the device, we see that the increase in number of cells travelling to the other reservoir is small, but increases linearly. On the other hand, in the same device, if the concentration is high, the number of cells reaching the initially empty reservoir is almost total after only 20 minutes. After those first 20 minutes, the ratio decreases from $N/N_{tot} \sim 0.8$ to $N/N_{tot\sim} 0.6$ in the next 20 minutes. In this case, after the majority of the cells travel across the device very fast and populate the initially empty reservoir, the cells start travelling back to the loading reservoir, trying to equalising the number of cells in both reservoirs.

## 5.5   Discussion

We described here in this chapter a variety of systems that have been let evolve in time, without any external input. The aim was to look at how confinement influences cell motion and the arising of collective motion when the concentration of swimmers increases too. Firstly, we looked at a system with increasing concentration and increasing radius of circular confinement and we tried to see in which range of concentration and radius the motion was a single rotating vortex. As in bacterial works [251, 253] we found a range of radii where for a high concentration of swimmers the motion is collectively organised as a single vortex rotating in the whole volume. Additionally, we investigated the range for concentration to influence the single vortex collective motion in confinement. We found that this concentration range changes with radius of confinement. For small radii, $r < 150\mu$m, the vortex order parameter, shown in 5.2 a), has values between 0.3 and 0.4 for small concentration. We interpreted this as the number of cells in each circle is sufficient to populate the entire boundary layer and create a locally coordinated motion, rotating altogether. For larger radii, the sperm population at the boundary is not enough to have any overall coordinated rotational motion at low concentrations, but when the concentration is increase, the boundary get populated allowing for a coordinated motion. Radii larger than 250$\mu$m and smaller than 80$\mu$m, we did not have stable circulation. In the first case the confinement was not enough to drive a single vortex rotation and even if the motion on the boundary layer was a single circulation, the bulk showed a turbulent motion. In the second case, we hypothesised that the interactions between cells confined in a disk of size smaller than double the cell length, become so strong that they disrupt the possibility of cell organisation. For radii between 80 $\mu$m and 250 $\mu$m, the vortex order parameter increases with concentration, up to high values of 0.9, showing that the system of more than $10^8$ cells/ml organise in a single rotating vortex. On the other hand, when looking at the velocities in figure 5.3, we didn't find a variation in the velocity values for the range of radii and concentrations we have a stable rotation. Indeed, we found that the velocities increase in value similarly to the bulk experiments shown in the previous chapter, 4. Looking at the single radii separately, we saw that the velocities increase after a critical concentration, which is the same for all radii. The increase is linear, but the slope of the increase depends on the radius of confinement: for larger radii, the slope is higher than for smaller one. On the other hand, the increase of the velocity values per each concentration at increasing radius is a power law. With this analysis we showed that the confinement can drive the spatial organisation and collective motion of the system, with the arising of single stable vortices rotating for a specific range of radii and concentrations. This spatial organisation, does not influence the velocity increase, which is dependent only on the overall concentration and confinement size.

We then tried different types of confinement, building from the different size circles, we created two systems: one symmetrical and one asymmetrical. We used a single radius in the range where a single vortex arise and we connected three or four circles, in the first case the centres of the circles were positioned at the corners of a equilateral triangle, in the symmetric case they were positioned at the corners of a square. We used high concentrated sample, so to be sure to have the collective motion inside the devices. As expected, the asymmetric system did not show any long term organisation, but had motion organised for very short period of times, as shown in figure 5.6. The symmetrical system showed more interesting results. In previous bacterial works [252], many distinct stable configurations for the direction of the vortices inside the circles have been found. These configurations vary depending on the distance between the centres of the circles. For the distance we used in our sperm cells experiments, the bacterial stable configurations are two, but we saw that only one stable configurations is present in our system. The stable configuration is when the circles which centres are on the diagonal of the square rotate in the same direction, hence top-right has a vortex rotating in the same directions as bottom-left and they rotate in the opposite direction of top-left and bottom-right circles. The system is not perturbed externally, but after some time of rotation the fluctuations of the system created an internal perturbation strong enough to change and invert the rotation of one circle, which then drives the change in rotation of the entire system. It is important to re-iterate that the system is not touched or perturbed externally, but only the fluctuations of velocity and directionality of the cells in the system lead to this change in motion.

Another confinement investigated is a ring device, in which the outer radius remained constant while the internal radii changed. We looked at three different width of the rings: a very thin one, an intermediate one and a very wide one. Previous works on various diluted sperm suspensions confined in rings [103], showed a phase transition in the rotational motion that appears with increasing concentration. While for high volume fractions, two oscillatory dynamics appear: one long term oscillation of around 15 s and a short period oscillation of 3 s circa. In our system we saw that the oscillations arising are dependent on the size of the annulus, but the rings with the intermediate widths, $\sim 120\mu$m, appear to be the most stable one, with a stable circulation in the ring. In this case the frequency of the oscillations in the system, were similar to previous works. This 15 seconds oscillations looks very robust in time around the $\sim 120\mu$m wide ring. On the other hand, for very thin rings, the rotation didn't appear to arise and the velocities in the rings are very small with respect to the other rings. While on the very wide rings, $\sim 215\mu$m, the motion appears to be organised on the boundary layers, but the middle part of the rings is behaving mostly turbulent, without sustaining a single circulation in the ring itself.

We then notice these oscillations for a system of dense suspension of sperm cells in narrow channels. The direction of the motion inside the narrow channels inverted with fixed

frequency that varied depending on the width of the channel itself. Even if we could not find a specific pattern in the frequency of reversal and in the amplitude of the reversal oscillations, we saw that these oscillations in the direction of motion are very robust and consistent in time.

Finally, used two different devices and two different concentrations in order to study how confinement drives efficient cell transport. We saw that the device with multiple channels has the majority of cells moving towards the second pool and populating it, even when the concentration of the sample used is reduced drastically, around 1000 times. While a system without multiple boundaries on which the cells can slide on has a very low number of cells arriving to the other side. We then deduced that the confinement helps transport the cells and it can be related to the tortuousness of the female tract.

## 5.6   Conclusions

After the analysis of the bulk environments for sperm cells, the system size was drastically reduced and we explored how the different type of confinement we could think of would influence the collective behaviour of the system. We found that circular chambers induce a single vortex rotation at specific concentrations and circle sizes, creating a "golden region" where the circulation inside the circle is unified and results into a single vortex occupying the entire environment. Allowing us to conclude that the size of the confinement plays a significant role in the type of motion.

We then looked at many different systems: connected circles, rings and channels. The denominator of all these experiments has been the arising of oscillations in the system. For the connected circles, when the system is symmetric it self organise and has a stable configuration that persist along the entire experimental time. Even if intrinsic fluctuations in the system create a perturbation strong enough to invert the directionality of the motion, the system rearrange to the stable configuration. This symmetric system results very robust.

We saw these oscillations in the doughnuts shaped devices, where mostly angular velocity and vortex order parameter result oscillating in time. Meaning that the rotation of the system oscillates between clockwise and counter-clockwise almost periodically with the same frequency for rings of width $\sim 120\mu$m.

Finally, looking at straight channels the oscillations can be seen, but unfortunately, no simple dependence between the concentrations and the widths investigated with the reversal frequency can be seen. On the other hand, using these devices compared with a single slide connection between the two reservoirs, can be used to study the transport efficiency of the cells with or without multiple boundaries. Resulting in a stunning difference, not only for high concentration samples. But even for low concentrations, the presence of

multiple confining boundaries makes the transport of sperm cells more efficient. More experiments should be carried on with channels, investigating more in depth the frequency of flow direction reversing depending on the width of the channel, its length and the sample concentration.

# Chapter 6

# Waves

## 6.1 Introduction

In this chapter we aim to describe and analyse a phenomenon we have witnessed during the experiments. With the intention to increase the speed and the activity of the sperm cells in the system we tried to increase the temperature. This temperature increase, instead of making more frantic the spermatozoa motion, created a wave motion in the 3D bulk system and a system of ring-like structures when the sperm cells were confined in 2D. We will present in this chapter the preliminary work on 2D and 3D system of spermatozoa when the temperature is raising from 25 °C to 37 °C. Researching in the literature, only two works correlate strongly with what we saw.

The first one is by Chen et al. [96], where swarming E. Coli bacteria are confined in a quasi-2D environment on top of an agar plate. For high concentration of bacteria, after a transient time, collective oscillatory motion arise. This oscillation is characterised by a spacial homogeneous velocity field oscillating in time, it persists for a minimum of half an hour and it is steady in period. The period depends on the colony, ranging between 4 and 12 seconds. Some silicon-oil droplets are added on the surface of the swarming cells. The trajectory of those tracers is tracked and they follow an elliptical trajectory whose chirality has equal probability to be clockwise or counter-clockwise. The collective oscillations are correlated over long distances, with identical period but with phase that varies linearly in space. Finally, they investigated the behaviour of the individual cells swarming on the substrate and creating these oscillations. Surprisingly, individual cells do not behave as oscillators, leading to the assumption that a weak synchronization at the population level is responsible for the emergence of the collective oscillations. When the system is stopped by reducing the temperature, forcing the cells to stop moving, the cell speed decreases as the amplitude of the oscillations. After warming up the system again, the oscillations emerge again. This shows that the oscillations are a stable configuration for the system.

If interfaces between two oscillations of opposite chirality are present after restarting the system, local chirality switching and gradual orientational change of the ellipses arise.

We found a similar appearance of oscillatory motion of sperm cells swimming in a 3D system at increasing temperature, which will be described in the first part of this chapter. In the second part, we will restrict the system where sperm cells move to a 2D system, confining them in a think layer. In this system, we found that, with increasing temperature, the sperm cells arrange into an array of vortices. This phenomena has been previously described by Riedel [40] in 2005, with sea urchin sperm. Indeed, as shown in chapter 4, sperm cells are found to have a swarming behaviour when at high concentrations [102, 101, 40, 100]. As shown from section 2.2.1, hydrodynamic interactions attract sperm cells to aggregate and to synchronise the beating frequency, collective behaviour of finite concentration sperm cells has been studied numerically [82, 254]. Experimentally, when swarming sperm cells are confined in a 2D system two different pattern arise: the aggregation trains in the wood-mouse sperm, seen by Moore and Immeler [101, 100] and the vortex arrays of sea urchin sperm described by Riedel [40]. As already shown in chapter 2, section 2.2.2.2, when sea urchin sperm surface density $\rho_0$ is increased over a certain threshold, the spermatozoa start arranging into ring-like structures with diameter around $d_0 \sim 25 \mu m$. These vortices are themselves arranged in a fluid like manner, forming structures with hexagonal order. The structures started forming when $\rho_0 d_0^2 \simeq 1$, this dimensionless density is the overlap density of circular trajectories. Each single vortex is seen to not change in size and to contain between 8 to 12 cells, in addition the circulation inside the vortices has been observed to be clockwise. The vortices occasionally fused or divided and at times cells will hop between them, but overall it is a stable configuration. These vortices are not anchored on the surface and they have seen to be moving with an apparent diffusion coefficient of around $D \sim 6.2 \mu m^2/s$, which results to be higher than the diffusion coefficient calculated for disks of a similar diameter as the rings ($D \sim 0.06 \mu m^2/s$). Hence, the cells active propulsion takes the array of vortices out of thermal equilibrium.

The packing of the vortices is an hexagonal pattern of average spacing of $r \sim 49 \mu m$ and since there is no long range correlation, the array behaves liquid-like instead of as crystal. While looking at the cells behaviour inside each vortex, Reidel at al. [40] found that there is a peculiar form of beating synchronization. Indeed, the correlation is not between cells phase oscillations or angular position of their heads. Instead, the correlation is between the difference in phase and angular position of each sperm pair in the vortex. Hence overall they swim at different velocities and have different beating frequencies, but locally, they are swimming and oscillating synchronously, as represented in figure 2.14 b).

Considering the model by Yang et al. [254], where cells are considered to have a planar beat and they are confined in a 2D system, and comparing this model to the experimental results from Reidel, we can draw three points: first, the diameter of the vortices does

not change with density of cells; secondly, the hydrodynamic interactions create weaker correlations in simulations, leading to the hypothesis that the interactions, not only they attract cells and help their synchronisation, but they also interact with the neighbouring rings disrupting their circulation paths; finally, when considering the fluid above the surface too, then the hydrodynamic interactions contribute to the stabilization of the arrays of vortices.

The above phenomena resemble what we observed in our experiments explained in this chapter. In fact, we observe both ring formation and oscillations over all the population in the channel. In our case the ring formation does not depend on the density of swimmers but on the temperature, while the oscillations arise when the system moves form a 2D confinement to a 3D.

## 6.2   Experimental Methods

### 6.2.1   Sample

The samples used for this analysis are ram samples treated as described in the previous chapter 4.2.1. Specifically, the ram samples are collected in loco, fresh in the morning from healthy animals. Experiments started right after collection and were carried on for a couple of hours, until cells were dead or enough data were taken. Only good quality semen was used for these experiments, using high concentration and high motility samples (between 4 and 5 value in the usual scale of evaluation). Usually the second donation of the day, half an hour after the first collection, was used. The samples were kept at room temperature, which was around 20 degrees Celsius at any time. Usually the original sample was kept undiluted and when diluted a buffer solution.

### 6.2.2   Experimental set-up

This chapter describes two major experiments. Firstly, we used a pre-filled PDMS chamber is filled completely with sample, with similar modalities as the previous experiments. This chamber, shown in figure 6.1, is a step design with six different heights: $H_1 \sim 7\mu$m, $H_2 \sim 15\mu$m, $H_3 \sim 25\mu$m, $H_4 \sim 40\mu$m, $H_5 \sim 70\mu$m and $H_6 \sim 130\mu$m. The total length of the device is 4 cm, and the width is 0.5 cm.

For the single cells tracking experiment, we simply introduced the sample in between two glass slides: a drop of semen is deposited on one glass and another slide is slowly placed on top.

The videos have been recorded with an Edgetronic camera set at 50 frames per seconds, while the single cell tracking has been recorded with the same camera, but at a frame rate
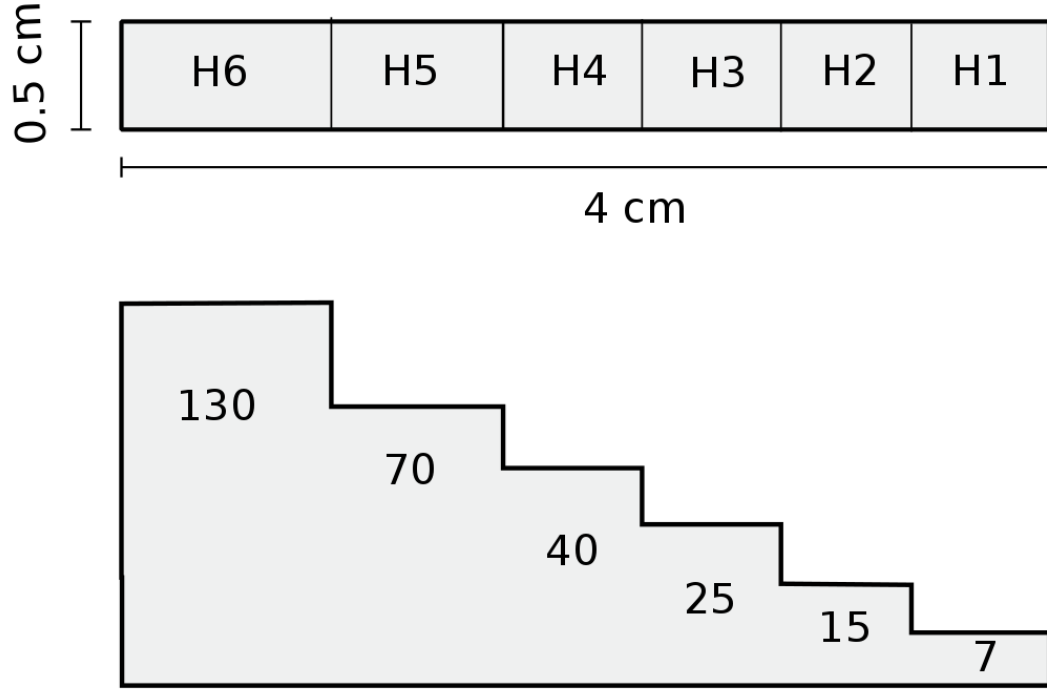
Figure 6.1: We used a PDMS device composed of six steps of different height, which are shown in the schematic: $H_1 \sim 7\mu m$, $H_2 \sim 15\mu m$, $H_3 \sim 25\mu m$, $H_4 \sim 40\mu m$, $H_5 \sim 70\mu m$ and $H_6 \sim 130\mu m$. The total length of the device is 4 cm, and the width is 0.5 cm.

of 300 fps. For the first part of the data, where height and temperature are varied, the data are collected with bright field microscopy and 15× magnification. While looking at the wave analysis, the aim was to look only at the wide range behaviour, so we changed to dark field imaging with 4x magnification. Same set up was considered for the circular pattern imaging.

In the final part, where the single trajectories are followed, the speed camera was recording phase contrast images with 40x magnification, in order to recognise more easily the single cells.

### 6.2.2.1   The heated stage

As shown in figure 6.2, the heated stage system is composed of five major units: the PC that controls the system through a LabView program; the power supply that gives enough voltage to reach the desired temperature; the ITO (Indium Tin Oxide) covered glass; the probe that samples the temperature on the surface of the glass and the Arduino Uno REV3, which is used by the computer to control all the other components of the system. Specifically, the computer runs a LabView custom made program that regulates the volt-
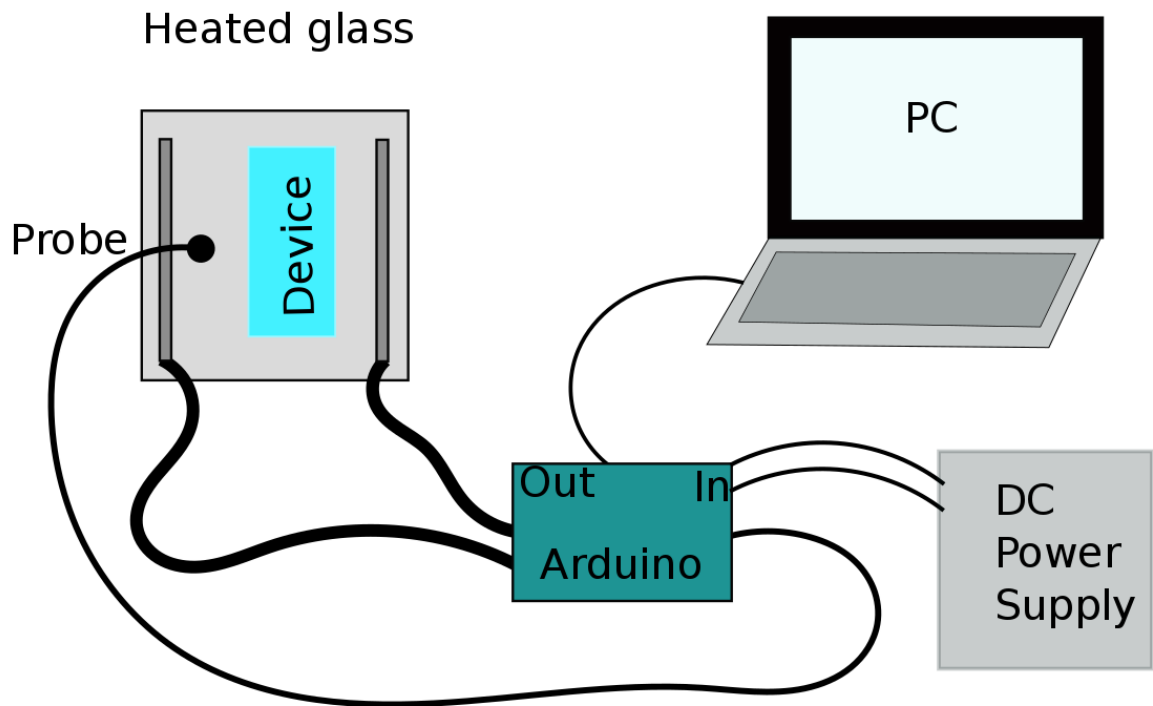
Figure 6.2: Schematic of the heated stage set up. The computer runs a LabView custom made program to regulate the temperature on the heated glass through Arduino. The Arduino device receives the information about the temperature on the glass from the probe and adjust the voltage in order to reach and maintain the desired temperature.

age across the ITO covered glass to match the temperature that was set up. The probe glued on the glass gives the information on the surface temperature to the computer, which will turn on or off the supply of voltage through the Arduino to the glass. If the temperature measured by the probe does not match the desired temperature, the Arduino will let more and more voltage through to the glass, so that it could raise the temperature. When the temperature is reached a alternation of on and off moments will keep the temperature as stable as possible. If the temperature is too high, the Arduino will stop supply of voltage to the glass, slowly reducing its temperature.

## 6.3 Emergence of waves and vortices

We used a PDMS device with a step scale pattern, figure 6.1, with thickness ranging from 7 to 130 $\mu m$, with overall size of around 4x0.5 cm in size. We varied the temperature between 25 °C and 35 °C. Increasing temperature we saw that in the thinnest part of the device, at high temperatures, ring-like structure arise and stably circulate until cells die. In the rest
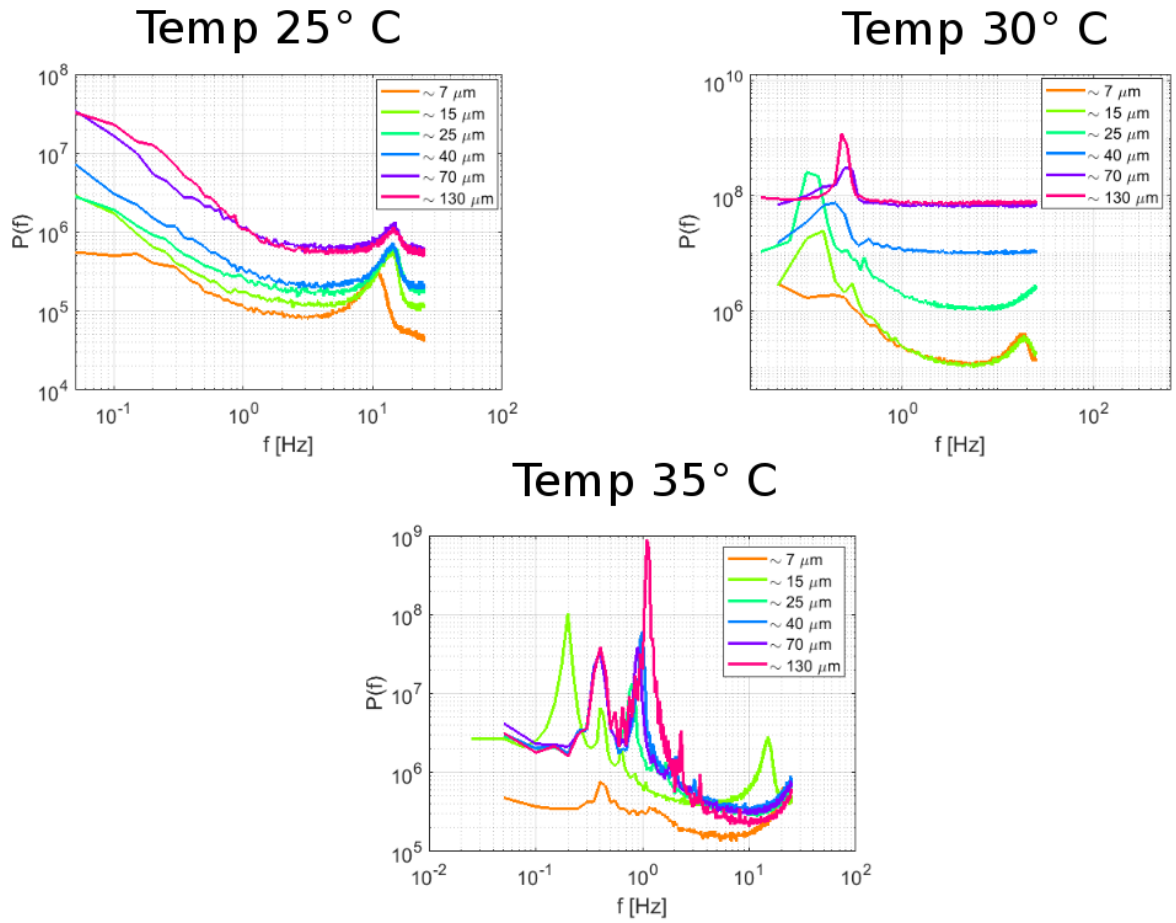
Figure 6.3: Power spectra for three increasing temperature and the six thickness of the device. They show the evolution of the system from turbulent motion to oscillations in the volume with increasing temperature. New frequency modes correlated with these motion phase arise and dominate the collective behaviour of the system.

of the device at high temperatures we saw a wave propagating through the entire volume of the step is seen.

Three major quantities were changed: the confinement, with six different heights, the temperature and finally the concentration.

### 6.3.1 Height and temperature

First of all we analysed a 1:1 concentration system, with concentration calculated at the surface being of approximatly $10^8$cells/ml. We investigated the behaviour of the different thicknesses for three temperatures. At 25 °C, the behaviour of the power spectra, figure 6.3 resemble the one of the bulk measurements from Chapter 3, having a peak in the power spectra at the sperm cells beating frequency. For very thin chamber, the values are smaller, probably due to the interference of the boundaries over the beating pattern. Indeed, from the derivation of the curvature radius, eq. 2.24, with a length of the sperm cell $l = 50\mu m$

and since l/2$\delta \sim 3$, as calculated by [73], the conical envelope that includes the beating pattern has a radius $\delta \sim 8\mu$m. This confinement probably modifies the beating, reducing its frequency, but with the increasing thickness, the frequency matches with the one calculated at the bulk. Not much different behaviour can be seen from the 25 °C data for different confinement, while if we increase the temperature to 30 °C, the two thinnest heights still conserve the beating peak, but at $\sim 15\mu$m, a mode starts showing, which is the excited mode of the cells, with increasing heights, the peak on the right disappear, the power spectra results flat apart from one or two peaks at low frequency. Those additional peaks are excitement modes that arise from the system starting its oscillation. Ring-like structures (as shown in figure 6.17) do not appear yet on the quasi-2D environments ($H_1$ and $H_2$), but from the videos, the cells seem to start vibrating at a low frequency. While for the rest of the heights the motion is oscillatory, but not fully a propagating wave as it emerges for the highest temperature. At this point, increasing additionally 5 °C the temperature, ring-like structures at the 7 and 15 $\mu$m chambers appear. In the 7 $\mu$m chamber, the rings appear and are stable, where spermatozoa locked in a ring without being able to move between rings, they indeed create separate structures that often push the dead cells to the boundary, creating enclosures between rings. While for the next chamber, 15 $\mu$m, sperm cells are grouped in clusters swimming in a semi circular motion, where rings can be recognised but they are not stable over time, indeed the clusters merge and move from ring to ring, creating a more dynamic system. In the following heights, 40, 70 and 130 $\mu$m, the motion is oscillatory, with a wave propagating though the chamber. Four peaks can be recognised in the power spectra with the major one at frequencies between 0.8 - 1 Hz, which results to be the frequency of the wave moving in the volume.

We then looked at the behaviour of the 25°C for a 1:2 dilution, comparing it with the 1:1 behaviour as show in figure 6.4. No noticeable difference appears with dilution, indeed neither dilution shows characteristic of the high temperature motion.

We then moved to analyse the highest temperature, 35°C, that seems to lead to the biggest motion changes in the fluid. We considered four dilutions, figure 6.5, one diluted sample, of 4 parts of buffer and one of sample, for concentration of **1:4** $\sim 2 \cdot 10^7$cell/ml. For lower concentrations we obtain flat power spectra for 3D environments and only a slight indication of a peak for 2D environment, showing the absence of ring-like structures in the think chambers and of waves in the thicker chambers. We then increased the concentration slightly to 1 part of sample and 2 of buffer, for a concentration of around **1:2** $\sim 3.34 \cdot 10^7$cell/ml. In this case we have the rings at $H_1$ and $H_2$, while the rest shows slight oscillations, which frequency of the major mode is always between 0.8 and 1 Hz. The oscillation has the same frequency as in higher concentrations, but the minor modes are very noisy. The reference concentration of **1:1** $\sim 10^8$cell/ml, commented from now on and finally we looked at the undiluted sample. Unfortunately in this case we have a lack of data
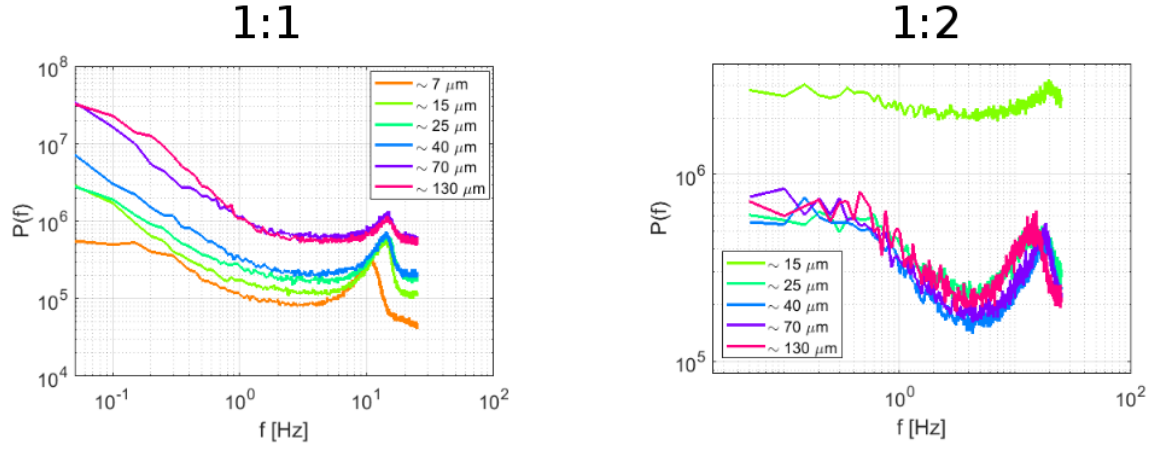
Figure 6.4: At constant low temperature, 25 °C, the system at two different dilutions does not show any significant difference. At similar to ambient temperature, the sperm cells behave like the bulk system analysed previously, without showing any characteristic of the high temperature dependent motion.

for the chambers with the highest thickness due to cell death, but we can still recognise the emergence of modes for heights $\geq 25\mu$m. Since during the experiments we noticed that the cell death of undiluted samples at high temperatures occurred very rapidly, not allowing for thorough measurements we decided that undiluted samples are not suitable for high temperature, 30 °C, experiments. From now on we will consider the 1:1 dilution.
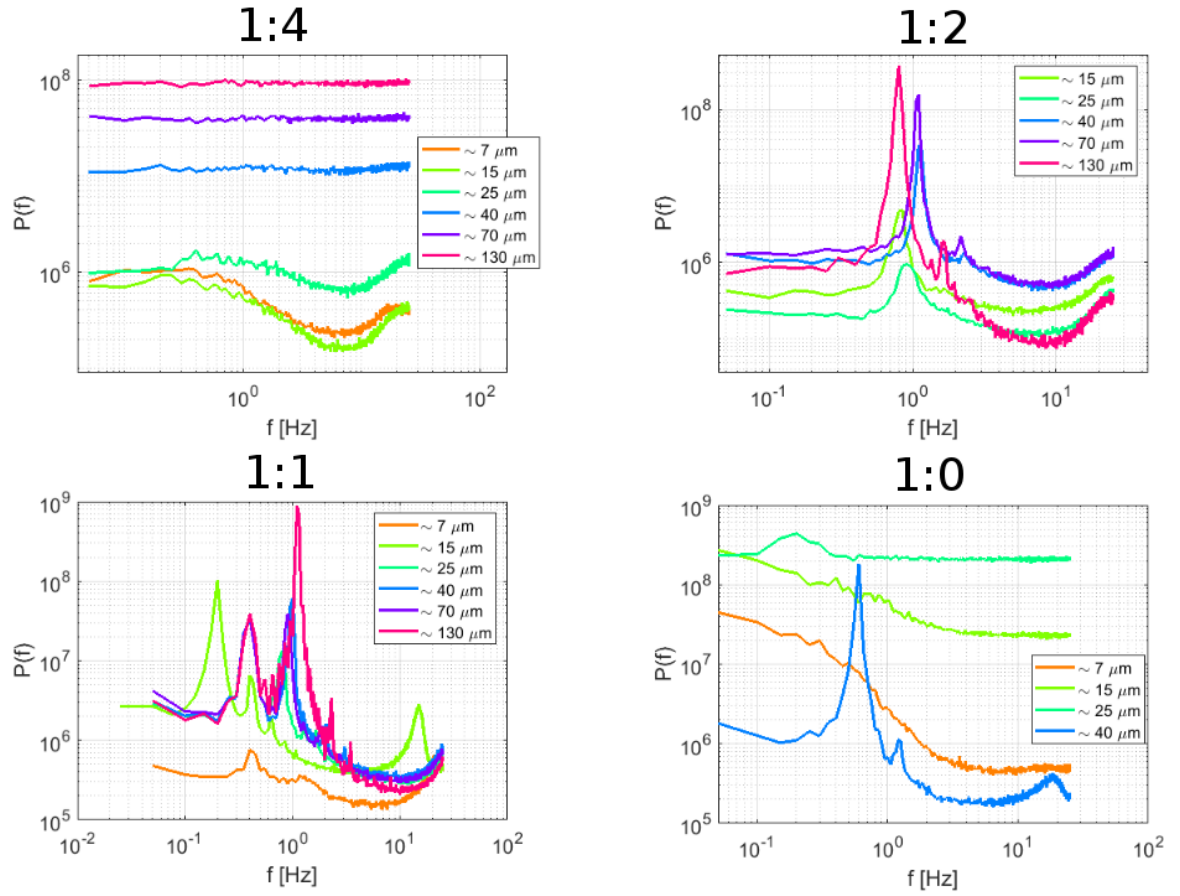
Figure 6.5: When temperature increased to 35 °C, the systems with higher concentrations of swimming sperm cells, show a transition to ring structures and propagating waves depending on the thickness of the environment they swim in. On the other hand, there is no appearance of frequency modes connected to rings and waves for the highest dilution, showing only what looks like a transition to collective motion.
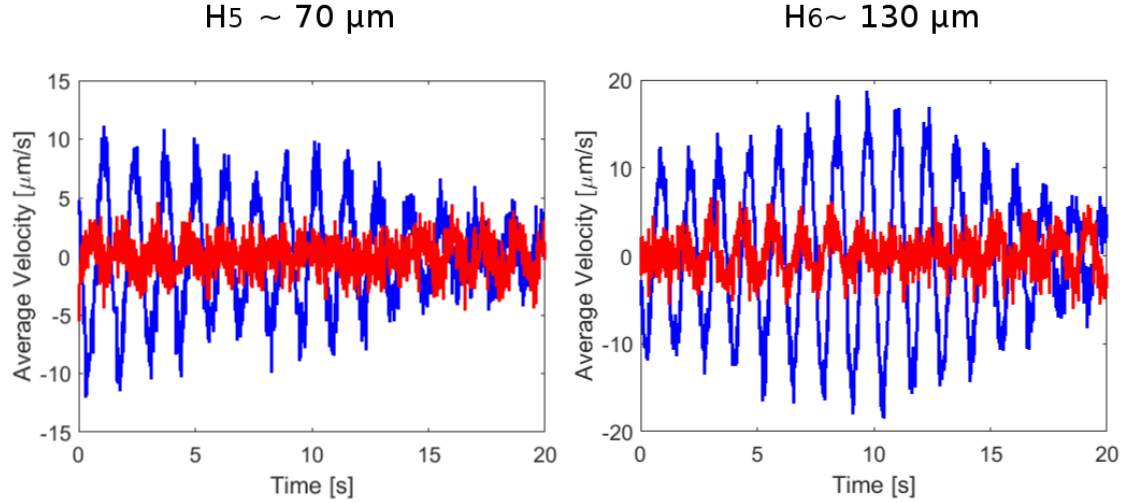
Figure 6.6: The average of the velocity in space, $V_x$ in blue and $V_y$ in red over time is plotted for the two thickest chambers, where the propagating wave is stronger and more accentuated. The clarity of the oscillatory behaviour of the velocities in the chamber is striking, with well defined period and frequency of oscillation. The difference in amplitude between the two direction of the flow field, show that the oscillation has a specific directionality for the propagation, preferring the propagation in the x direction.

## 6.3.2   Wave analysis

With the intention to study the oscillatory behaviour in the high chambers, we concentrated on temperature 35 °C and concentration **1:1** $\sim 10^8$cell/ml. In order to reduce the short interaction influence and trying to look at a wider field of view, we reduced the magnification. The spatial average of the velocities is shown in figure 6.6, where it is possible to notice the oscillatory behaviour for the two highest chambers. Both the oscillatory average velocity appear to vary in amplitude in time, but with a fixed period of variation. This variation is more visible in the $H_5$ velocities since it seems that a couple of variations can be recorded.

Taking as a reference point the center of the flow fields, examples of the flow fields can be seen in figure 6.7, we plotted the velocity kymographs of the cross section in x and then in y over time of both $V_x$ and $V_y$, figure 6.8 and 6.9. They show a wave propagating in space and time for both chambers, but the frequency of propagation changes depending on the height of the chamber.
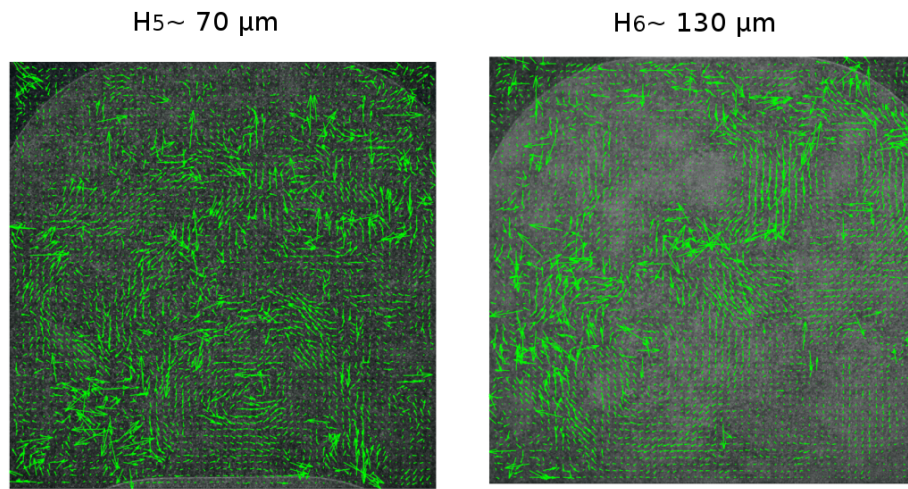
112

Figure 6.7: Figure from the analysed data with its quiver plot superimposed. It is possible to see the typical flow representation in case of propagating waves in the chamber. For the $H_6$ chamber, $200\mu m$ is distance between the two main vortices present in the wave pattern. Those two points do not move in the fluid and remain constant points throughout the oscillations of the system.
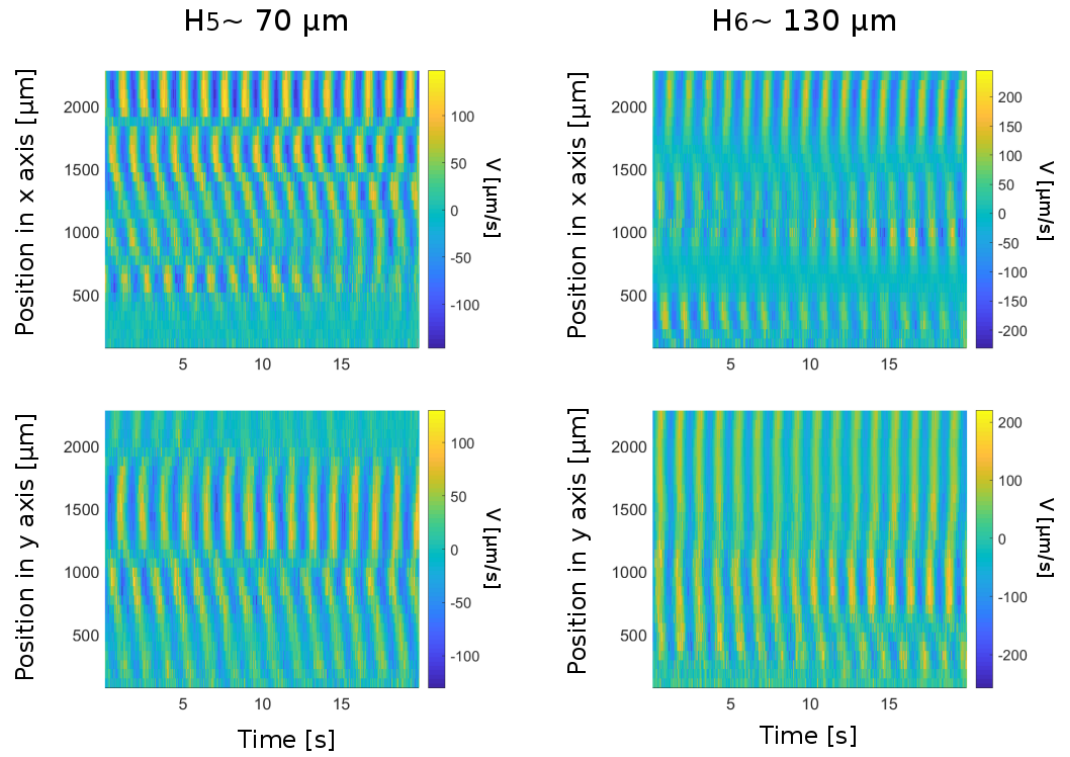
Figure 6.8: Kymographs of $V_x$ velocity components for the two thickest chambers. The velocities are taken at the central point of the velocity flow field and a cross section for the x and one for the y direction are shown here as representative of the propagating wave present in the fluid.
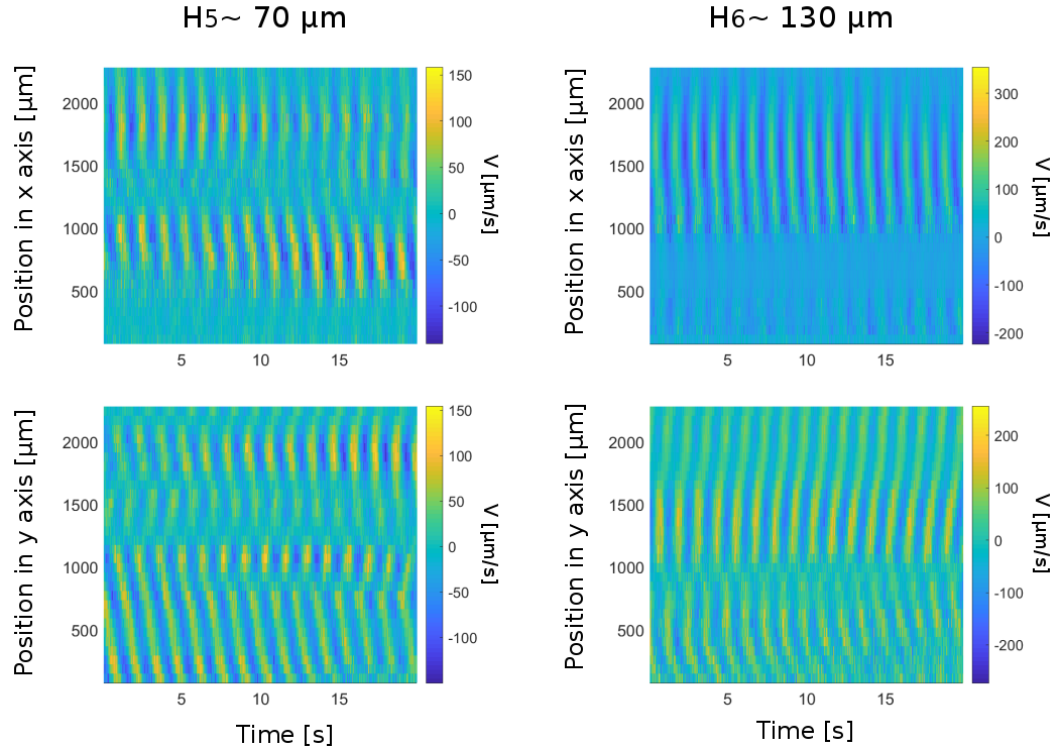
Figure 6.9: Kymographs of $V_y$ velocity components for the two thickest chambers. The velocities are taken at the central point of the velocity flow field and a cross section for the x and one for the y direction are shown here as representative of the propagating wave present in the fluid.

As a first step, analysing the velocities we can conclude that there is a wave propagating and moving along the chamber, which characteristics vary with the height of the chamber. To corroborate this, we try to fit a sine wave $y(t) = A \sin(\omega t - \phi)$ onto the wave signal from the data, finding the basic quantities for the wave. Mostly, we consider the peak frequency of the power spectra, which results on average around 0.8 Hz, giving an angular frequency of $\omega = 2\pi f = 5 \, \text{rad/s}$ and a period of the sine wave of 1.25 seconds. And then we computed the phase of the wave at that frequency, resulting in two plot of the average phase in time over the space shown in figure 6.10. We can notice that the phase for the highest chamber shows a very specific pattern, representing a stable wave in the entire field of view, with fix phase in space.

### 6.3.3 Correlations

We then turned our attention back again to the full set of heights and we tried to compute the autocorrelations and cross correlations for the entire dataset of heights.
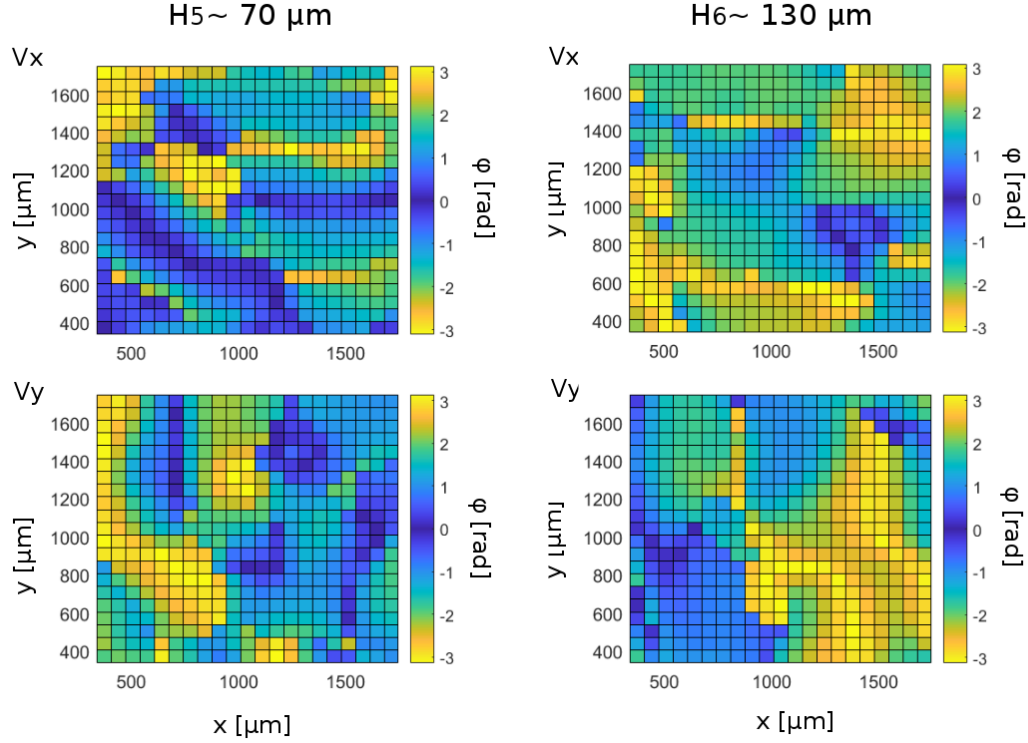
Figure 6.10: Colour plots of the phase at the peak frequency of the oscillation for both highest thickness of chamber of for both $V_x$ and $V_y$ data.

#### 6.3.3.1 Autocorrelation

Firstly the autocorrelations show a very peculiar and specific damped oscillation patterns that vary with height. The 7 $\mu$m environment does not show temporal correlations, while the next one have a longer temporal correlation compared to the thickest chambers. In fact, the chambers $H_3$ to $H_6$, show a similar time scale for the end of the autocorrelation, even if their damping looks different between them. If we estimate $\tau$, in a different way from the previous chapters, considering it as the time scale of the end of the damped behaviour of the autocorrelation, we can see how the temporal correlations vary with height. First of all, the time scale for $H_2$ is the longest, showing that the points in space correlate with themselves for longer times, with ring like structures reappearing continuously in the same points in space. Hence, $\tau$ can be estimated to be around 37 seconds, almost as long as the recording. Increasing the height of the chamber lead to two shorter correlation times, $\tau_{H_3} \sim 16$s and $\tau_{H_4} \sim 18$s, but that are not simple damped oscillations, while they show, one a two slope damping and the other has a recovery in the autocorrelation, before decreasing again with a different slope. The final two chambers have a typical damped oscillator autocorrelation, with in the first case a time scale of around 15 second and the second one of around 17 second.

116

The autocorrelations can be interpreted as that for all the chamber apart the last two and the first one, there are two temporal correlations, one at shorter times, probably due to the ring structures in the thinnest and temporary structures or different wave patterns in the oscillatory phase.
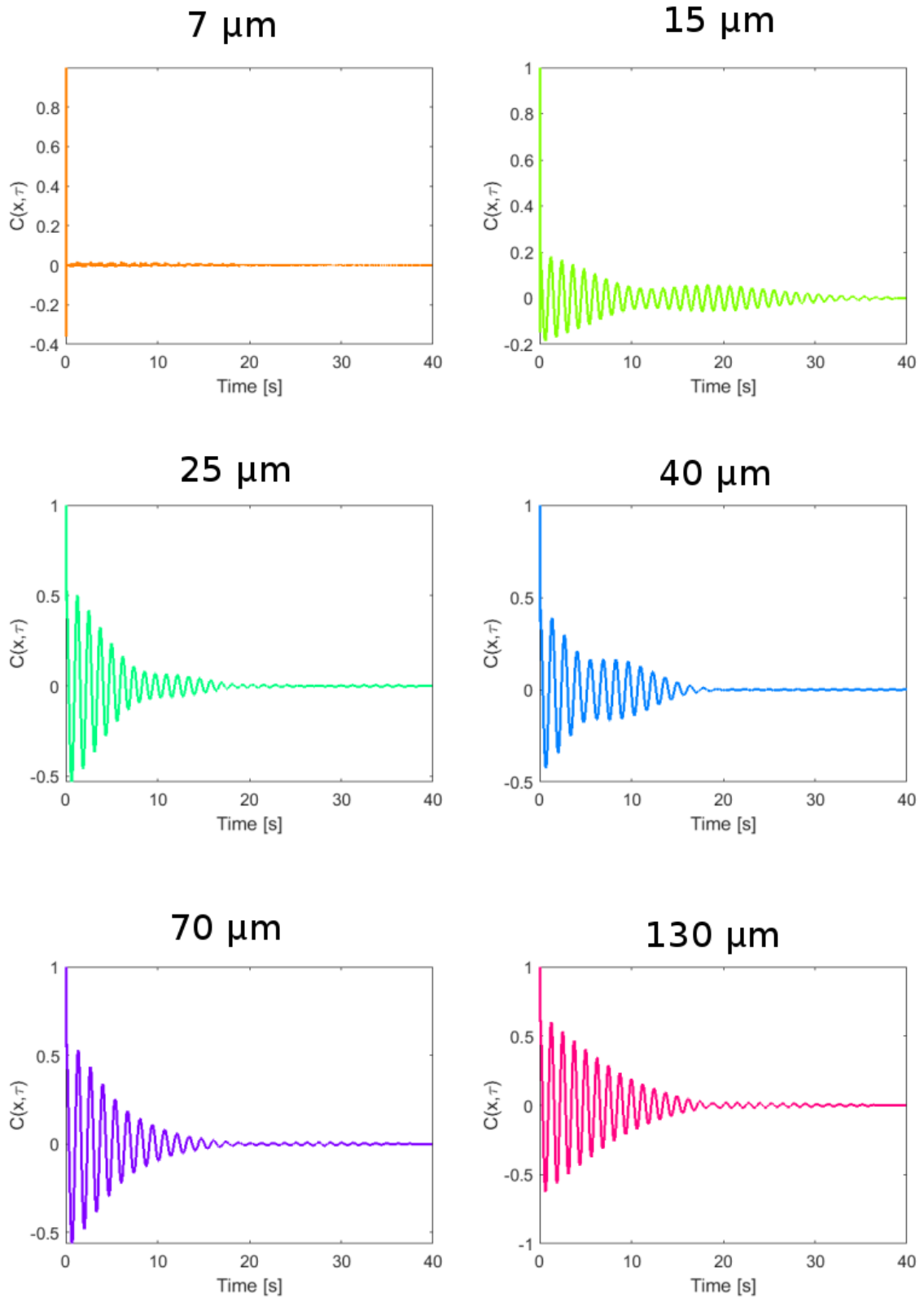
Figure 6.11: Autocorrelation functions for the velocity $V_x$, showing the damped oscillatory behaviour. The different correlation times vary slightly in between thickness, but most importantly it appears to be a oscillatory motion for the majority of the environments, but for the intermediate heights the decrease in temporal correlation seem to follow two or more trends, probably due to the multiple interactions taking part: the correlation of cells in the ring-like structures, the interaction between rings and finally, when the width is large enough the collective oscillatory motion of the fluid.
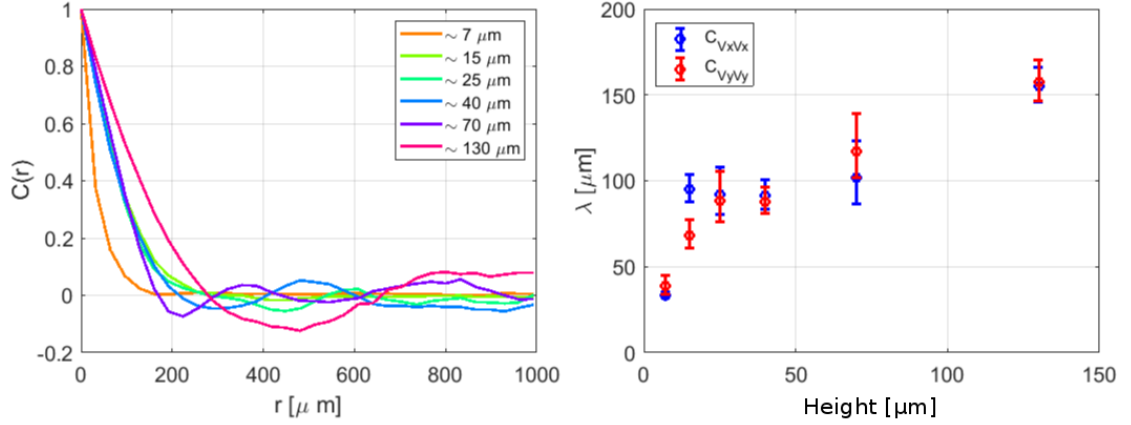
Figure 6.12: Plot of the spatial correlations for the velocities of every height. The correlation length increases with height, with correlation length shorter than the single cell length, where the spermatozoa are "trapped" in ring-like structures dimension smaller than the one of the swimmers composing the ring. The lack of inter-ring interaction leads to correlation length of the order of the ring size, while with increasing 3D size of the environment, the cells can interact leading to an increase in the correlation length. Additionally, $\lambda$ results to be, for the thicker chamber, near the value of the distance between fixed points in the wave motion found previously.

### 6.3.4   Cross correlation

We calculated the cross-correlation as in eq. (4.5) and as in Chapter 4, we fitted an exponential function and we extrapolated the correlation length as $\lambda$: $C(|\mathbf{r}|) = e^{-r\lambda}$.

Looking at the spatial correlation, not only the single correlation function continue correlate and anticorrelate, but their exponential fit $\lambda$ increases up to close to $200\mu$m.

Specifically, in fig. 6.12, it can be seen that the correlation length $\lambda$ in creases logarithmically up till 50 $\mu$m and then it linearly increases for the thickest chambers. The maximum value for the spatial correlation is similar to the distance found between vortices in the 3D system.

## 6.4   Swimming patterns

After having analysed the thicker chambers we turned our attention to the single cells swimming patterns, trying to understand the dependence between the trajectories and the temperature that leads to the ring appearance. We diluted the sample 100 times, introduced 10 $\mu$m glass beads in the sample and a drop of it was squeezed in between two glass slides. The glass beads will provide the separation in between the slides, giving an environment with only upper and under boundaries distant 10 $\mu m$. Slow motion videos

119

of the trajectories of single cells have been recorded and the sperm cells trajectory has been followed throughout the length of the video. With such a high number of frames per second, the reconstruction of the sperm motion has been possible, not only defining the overall trajectory, but even resolving the movement of the head over time. The found trajectories have been then fitted with a second polynomial, the radius of curvature of the fits have been computed and plotted against the temperature.

### 6.4.1  Curvature

The sign of the signed curvature $k$, is an indication of the rotational direction of the curve: negative clockwise and positive counter-clockwise. In case of a plane curve defined by parametric Cartesian coordinates $(x(t), y(t))$, the signed curvature $k$, is defined as:

$$k = \frac{\dot{x}\ddot{y} - \dot{y}\ddot{x}}{(\dot{x}^2 + \dot{y}^2)^{3/2}} \tag{6.1}$$

where, $\dot{x}$ and $\dot{y}$ are the first time derivatives, while $\ddot{x}$ and $\ddot{y}$ are the second time derivatives. The radius of the curvature is defined as $R = |1/k|$.

From the trajectories traced as in fig. 6.13, the radius R has been calculated. It is possible to see in fig. 6.13 the change in the trajectories of sperm cells at different temperatures. As explained in Chapter 1, sperm cells travel at a boundary with a curved trajectory, so there was no surprise when the low temperature trajectories have a finite value for the average radius of curvature. This radius reduces, as shown in figure 6.14, in value and remains without variations at temperatures between 30 °C and 32 °C. The trajectories at temperatures between 33 °C and 35 °C are the one with the smallest values, then they increase again.

We can compare the values for the radius at 34 °C with the correlation length found in the previous section from figure 6.12 at heights $\sim 7\mu$m and $\sim 15\mu$m, we notice that the average radius R(34) $\sim 100\mu$m, while the correlation length $\lambda \sim 50 - 100\mu$m.

This reduction in the radius of the turning of the trajectory, is considered to be at the base of the ring formation at high enough concentration of sperm cells.

In order to complete the picture, we looked at the distributions of right and left turning trajectories at the temperatures and we can see similar distributions, with the only variation is in the position of the two peaks. We can then deduce that there is no preferred rotational direction, see figure 6.15. Thus, when the trajectories of sperm cells start to close, the cells rotating counter-clockwise will cluster and create a ring, while the one rotating clockwise, won't be tangled in that ring, but will create another one rotating in the clockwise direction. We can then conclude that the rings do not have a preferred rotation, but will have an equal distribution of clockwise and counter-clockwise rotating rings.
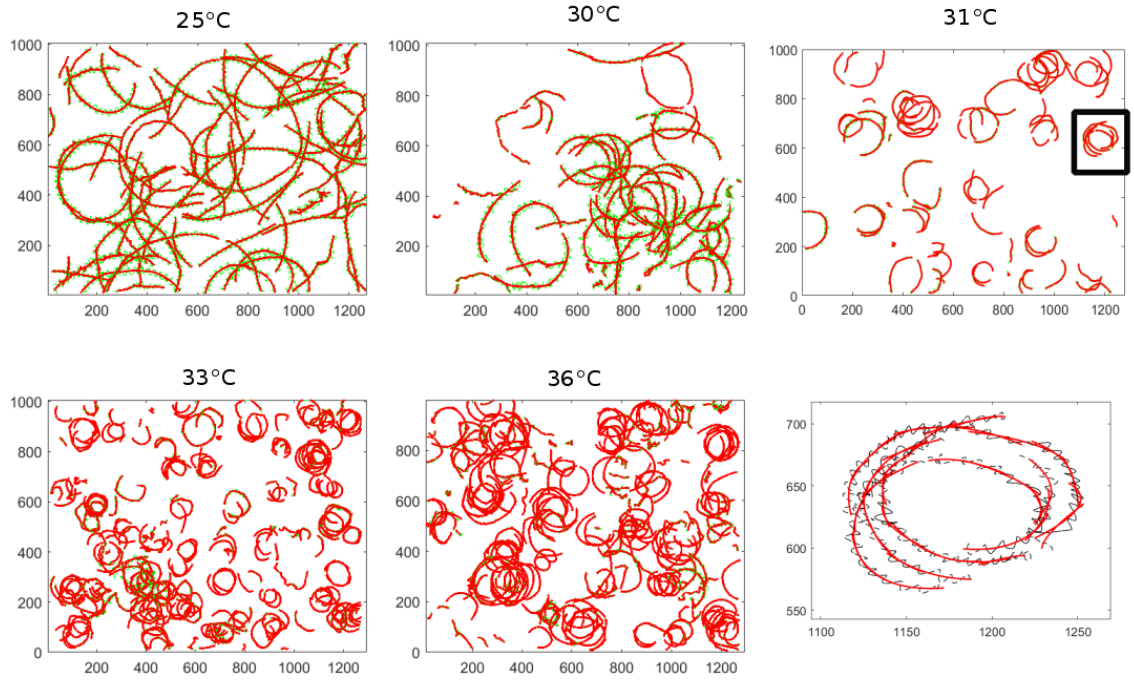
Figure 6.13: The trajectories of the single sperm cells are traced. Few examples of the trajectories found for different temperatures, where it is possible to see that the trajectories appear to follow a much steeper turn when swimming at high temperatures. Green lines are the tracked trajectories, while the red line are the fitted trajectories. The dimensions of the images here shown are in pixels. The cased trajectory is zoomed to show the head tracking (in black) and the trajectory fit in red.

## 6.4.2 Velocities

Since we were able to reconstruct the full movement of the sperm head, we considered that the beating frequency would reflect on the wave pattern of the sperm head trajectory. We hence subtracted from the full trajectory, the fitted path and we Fourier transformed the resulting function. From the power spectra we then took the main frequency and we plotted it as a function of temperature. We saw an increase in the head oscillation frequency from $f \sim 12.5$Hz to $\sim 16$Hz.

On the other hand, calculating the cell overall velocity from the fit function of the trajectory, figure 6.16, we can notice a significant drop, more than half, in the cell speed from 25 °C to 30 °C. Indeed, the speed reduces from $\sim 50\mu$m/s to $\sim 25\mu$m/s over 5 degrees. After we notice a slow and linear increase up to around $37\mu$m/s for 35 °C.
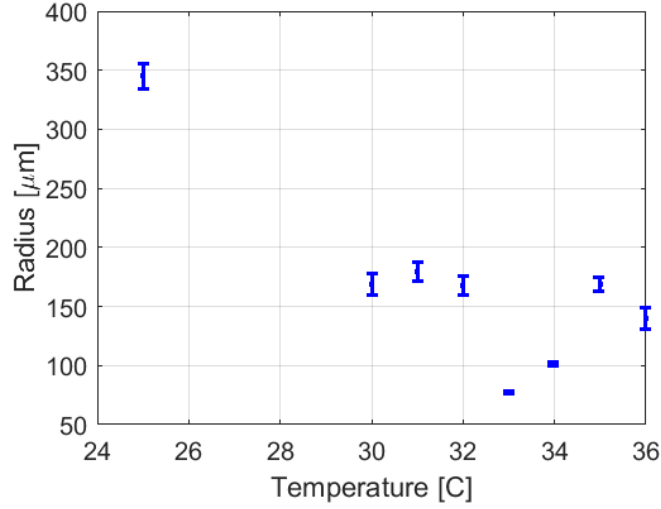
Figure 6.14: For different recorded temperatures the radius of curvature of the single cell trajectories has been computed and then the average value per temperature have been plotted.
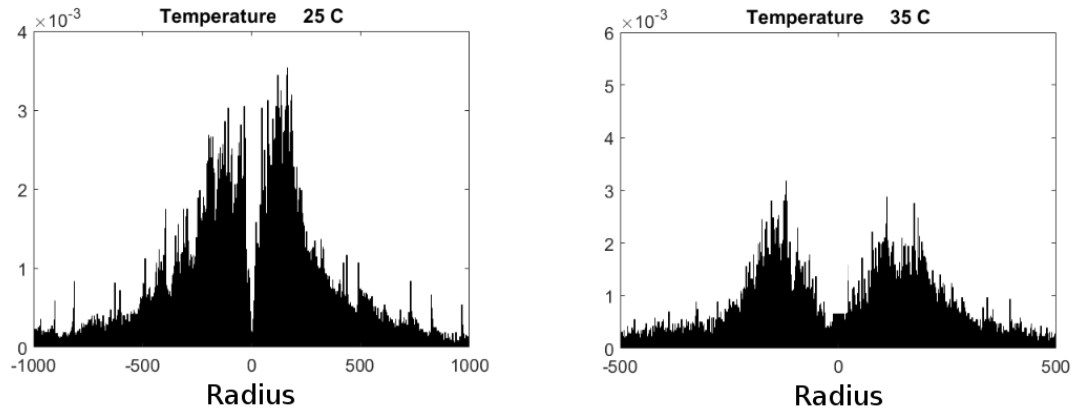


Figure 6.15: Histogram of the radius of curvature at two different temperature, showing that the radii are equally distributed between clockwise and counter-clockwise rotating.

### 6.4.3  Circular patterns

Looking at a $15\mu$m thick chamber, similar to the one from chapter 4, with only progressively motile cells in the environment, we can study the high concentration collective motion of the cells trapped in a very thin device at high temperature. High concentration of cells are present, but the system does not enable the formation of multiple layers of circulating cells, that working as oscillators creates the wave seen before. In this case, since the system is quasi 2D, not allowing stacking of cells, the collective motion is not a propagating wave, but it results in circular structures of different radii, figure 6.17.

It can be noticed that at lower temperatures the rings appear wide and the radius decreases as expected with temperature. When the highest temperature of 37 °C is reached the single
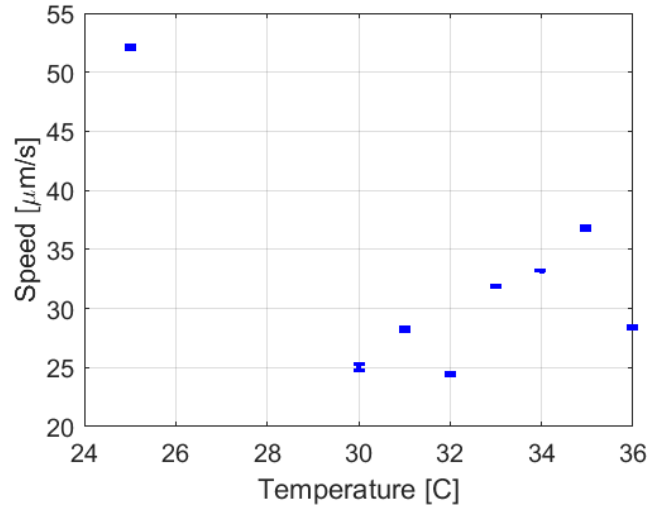
Figure 6.16: For different recorded temperatures the velocities of the single cell trajectories has been found from the fitted trajectory and then the average value per temperature have been plotted.
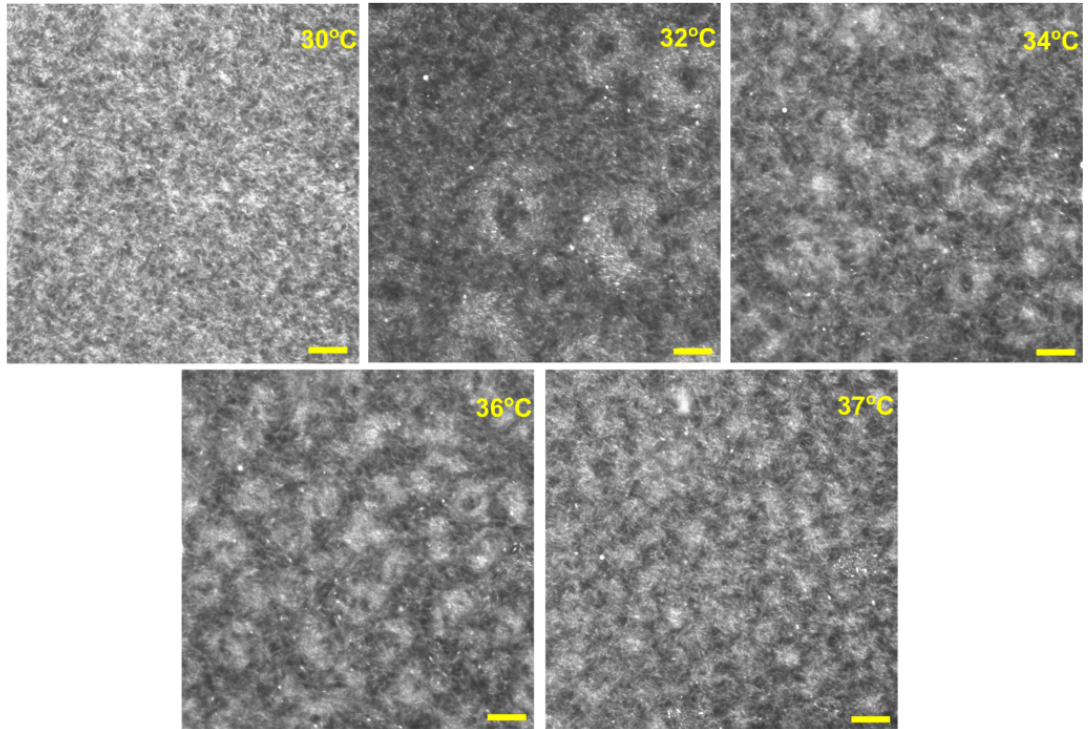


Figure 6.17: Pictures from variation of temperatures in 2D system of sperm cells. Scale bar 100$\mu$m. The rings arising at higher temperature decrease in size with increasing temperatures, until the motion is strongly disrupted by temperature at 37 °C, with the breaking of the rings structures.

cell motion is disrupted by temperature, reducing the motility and hence destroying the ring structures. Interestingly, when the temperatures are lowered, the cells will reactivate and swim in a circular pattern with the same radius as previously for that specific temperature. This shows a coherent and robust system, where cells swim with a specific curvature in their trajectory, independently of the history of the system, but only depending on the instantaneous temperature perceived.

## 6.5   Discussion

On this preliminary work on change of motion depending on the increase of the temperature in the system we can see two main patterns: one in the bulk and one in quasi-2D. When the system is in 3D, the collective motion of the system is a wave. From a height of $\sim 70\mu$m to $\sim 130\mu$m the collective behaviour is a wave propagating in space. We quantified the frequency and the phase of the propagating wave. The period of these waves are around 1.25 s, but when the average velocity in space are plotted, figure 6.6, it is possible to see that the waves are not homogeneous waves, but they looked encased in a oscillating envelope, showing a possible evidence of existing beats or it could derive from a propagating wave more similar to active gels. On the other hand, the correlations for thick chambers show an exponential decay of the envelope of the autocorrelation function, while the cross correlation shows high values of the correlation lengths, around 200 $\mu$m. More experiments and analysis needs to be performed in order to characterise properly the wave seen in these experiments.

On the other hand, when the system is confined in quasi-2D, the collective motion of the sperm cells show a peculiar pattern only seen in [40] on sea urchin sperm when concentration in increased. In our case, the temperature is the variable that "activate" the ring formation. Indeed, when the temperature increases the highly concentrated sperm cells create circular pattern, shown in figure 6.17, which size decreases with increasing temperature. In this quasi-2D system the autocorrelation varies with height. For very thin chambers, $\sim 7\mu$m, no temporal correlation is seen, while for 15 $\mu$m shows a long time correlation that seems encased in an oscillating manner. In this latter confinement, the rings are not only present, but more stable respect the the other heights. The correlation lengths for the thinnest step is smaller that the cell length, while for the 15 $\mu$m chamber it increase to just below 100 $\mu$m. In both steps ring-like structures are present, but we can deduce that the vertical confinement can influence the distance of interactions and it could possibly influence the size of the rings. Indeed, when looking at figure 6.17, taken in a 15 $\mu$m device, we can notice that for high temperatures, over 35 °C, the radius appears to have values just below 100 $\mu$m.

We tried to correlate this collective ring formation to single cells tracks. We performed

an analysis of the movement of the single cells, where we averaged over all the tracks for each temperature. This analysis showed, figure 6.14, a very peculiar pattern in the radius size: at first it decreases in temperature, but then it increases again. We do not see this behaviour in the collective experiments, where the ring sizes appear to keep decreasing with increasing temperature. On the other hand, the single tracks analysis shows that the rotation of the cells does not have a preferred rotation, but the distributions appear to be symmetrical, see figure 6.15. In figure 6.16, even the average velocities per temperature show an initial decrease and then an increase in its values. We can only deduce that the relation between radius and velocities with increasing temperature is not as simple as we initially thought. More data and single track correlations between radius and velocities need to be taken and carried on. We expect that after some in depth analysis of the single cell motion, it would be possible to create a Vicsek model replicating the ring formation. Additionally, more experiments are needed to elaborate the expansion from the quasi-2D system to the 3D one. We hypothesise that on the upper and lower surface of the 3D bulk environment, series of ring-like structures are present, which act like coupled oscillators and drive the wave propagation inside the bulk.

## 6.6   Conclusions

This behaviour arising from thermal excitation of sperm cells is most fascinating. The single cell motion changes drastically with temperature accentuating the tendency of sperm cells to swim on a curvilinear trajectory. With increasing the radius of curvature of the trajectories, there is a decrease in the overall velocity of the path and an increase in the frequency of head movement. This could be the result of the cells beating pattern changing with temperature, with wider head oscillations which are reflection of a variation in the shape of the tail beating itself. This results in a decrease of the overall distance covered in time, hence the mean velocity will decrease proportionally.

With the radius of the trajectories becoming smaller with temperature and when high concentrations of cells swim in a 2D environment the sperm cells in the system create ring-like structures that move in space, but most interestingly, the ring-like structures change their sizes with temperature, following the shrinking of the single cell trajectories.

The cells trapped in the ring structures do not interact with the cells in the other rings. This lack of interaction is due to the size of the system. Indeed, the minimum interaction distance between cells is given by the height of the third dimension confinement, that for very thin chamber results in almost no interaction between cells belonging to two adjacent rings. In fact, those rings are virtually isolated from the other neighbouring rings.

Finally much further work has to be completed. The study of the variation in shape of the beating pattern with temperature should be carried on, additionally with the study of

the reason for the sharper turn of the trajectories with temperature. Moreover, along with simulations, further studies on the creation of both the ring-like structures and the waves arising with temperature. The aim should be to understand how these structure are created and in case of the ring like structures which interactions are between them. A further step in the understanding of these temperature controlled changes of motion, would be to explore the biological consequences. The real temperature which the sperm cells have to navigate to reach the egg for fecundation, is much higher than the usual ambient temperature. Indeed, the body temperature in mammals is higher than 30 °C. This could imply that inside the female tract the trajectory of the spermatozoa do not result in a wide radius curve, but on the contrary, have very sharp turns. Interesting point would be to look at the high temperature behaviour in very narrow and/or tortuous channels, to understand how both temperature and confinement coexist and lead the transport of cells towards the egg.

# Chapter 7

# Conclusions

From this widely spread and scattered work we would like to point out some key results:

- **Bulk**: A system with increasing concentration of actively swimming sperm cells confined in a space large enough that the boundary interactions can be considered to be overlooked, shows a phase transition from random to collective motion. The behaviour throughout the concentration range looks to behave similarly with respect to the critical concentration for different mammalian species, showing a certain degree of universality. We found that the correlation length of the velocities in the collective state weakly depends on the cells concentration, while the velocity autocorrelation time reaches a maximum value immediately after the transition, and sharply decays with further increase in the cells' concentration.

- **Confinement**: Reducing the size of the system and retrieving the importance of boundary interactions, it is possible to see that in circular systems an lower and upper bound for presence of single vortex motion, while outside this bounds, the system acts randomly or turbulent, with respectively higher or lower boundary interactions. Rendering the system slightly more complex with different pattern of confinement oscillations of vortex rotations have been seen. The system change the direction of rotation and if it is a symmetrically connected system, the perturbation leading to directional change, is protracted to the rest of the connected system. After a readjustement period, the connected structures appear to be again in equilibrium, as concerning the rotation of the system's components. On the other hand, an asymmetric layout, will not let the system reach rotational equilibrium at any point, continuously varying the rotational order of the components as a result of small perturbations of the system. Finally, addition of an extra boundary at the center of the circular structures, leads to more robust oscillations that periodically change the rotation of the internal flow. The distance between the inner and outer boundary will define the oscillatory frequency and the coherence of the internal flow, indeed if the

two boundary result far away enough, the internal part of the doughnut will show turbulence and not coherent motion.

- **Channels and transport**: When confining the system in narrow channels the same oscillatory behaviour arise, but even though no significant correlation has been found between concentrations, channel width and oscillatory frequency, this type of system is very useful to study the characteristic of sperm transport throughout long distances. Indeed, when presenting a wide space without boundaries and confinements if not the upper and lower bounds defined by the thickness of the chamber, the sperm cells struggle to move directionally towards the desired space. Moreover, when confinement, in form of narrow channels, is present, the movement of the sperm cells from one reservoir to the other is extremely efficient even for very low concentrations. We can deduce that confinement plays an important role for egg fecundation, not only directing the cells towards the right direction, but making more efficient the displacement towards the ovum.

- **Temperature**: One of the most fascinating results appears to be the correlation between temperature and single cell trajectory modification. Where the sperm cells results with a radius of curvature for their trajectories that decrease with increasing temperature, while the overall velocity of the trajectory decreases. These single cell behaviour translate to the creating of ring-like structures in two-dimensional systems and for the presence of waves, similar to mitochronal waves seen for the cilia in the three-dimensional systems. For the 2D cases, the rings change size with increasing temperature, shrinking proportionally with the radius of curvature radius of the single trajectories. The rings are present when cells can move, when the temperature reaches high values, they shut down, reducing motility to a minimum and the rings then disappear. This static system will turn back to motion when the temperatures will decrease, creating rings of size similar to the ones from before the high temperature stop, showing that the dependence on the radius is only on the perceived temperature. Additionally, when cells are in a3D environment, the different rings, not only manage to stack on multiple layers, but since their interaction is due to the third dimensional confinement, they can finally have the cells composing the rings interacting. This interaction leads to a system behaving like a myriad of coupled oscillators, that macroscopically result in a wave propagating throughout the entire fluid.

# List of Figures

# Bibliography

[1] Edward M Purcell. Life at low reynolds number. *American journal of physics,* 45(1):3–11, 1977.

[2] Eric Lauga and Thomas R Powers. The hydrodynamics of swimming microorganisms. *Reports on Progress in Physics,* 72(9):096601, 2009.

[3] J Happel. *H., Brenner,* volume 115. 1965.

[4] GJ Hancock. The self-propulsion of microscopic organisms through liquids. *Proceedings of the Royal Society of London. Series A. Mathematical and Physical Sciences,* 217(1128):96–121, 1953.

[5] Allen T Chwang and T Yao-Tsu Wu. Hydromechanics of low-reynolds-number flow. part 2. singularity method for stokes flows. *Journal of Fluid Mechanics,* 67(4):787–815, 1975.

[6] TJ Pedley and JO Kessler. Hydrodynamic phenomena in suspensions of swimming microorganisms. *Annual Review of Fluid Mechanics,* 24(1):313–358, 1992.

[7] GK Batchelor. The stress system in a suspension of force-free particles. *Journal of fluid mechanics,* 41(3):545–570, 1970.

[8] Howard A Stone and Aravinthan DT Samuel. Propulsion of microorganisms by surface distortions. *Physical review letters,* 77(19):4102, 1996.

[9] James Gray and GJ Hancock. The propulsion of sea-urchin spermatozoa. *Journal of Experimental Biology,* 32(4):802–814, 1955.

[10] Leif E Becker, Stephan A Koehler, and Howard A Stone. On self-propulsion of micro-machines at low reynolds number: Purcell's three-link swimmer. *Journal of fluid mechanics,* 490:15–35, 2003.

[11] AT Chwang and Th Y Wu. A note on the helical movement of micro-organisms. *Proceedings of the Royal Society of London. Series B. Biological Sciences,* 178(1052):327–346, 1971.

[12] James Lighthill. Flagellar hydrodynamics. *SIAM review*, 18(2):161–230, 1976.

[13] RG Cox. The motion of long slender bodies in a viscous fluid part 1. general theory. *Journal of Fluid mechanics*, 44(4):791–810, 1970.

[14] G. K. Batchelor. Slender-body theory for particles of arbitrary cross-section in stokes flow. *Journal of Fluid Mechanics*, 44(3):419–440, 1970.

[15] J. P. K. Tillett. Axial and transverse stokes flow past slender axisymmetric bodies. *Journal of Fluid Mechanics*, 44(3):401–417, 1970.

[16] L Gary Leal. *Advanced transport phenomena: fluid mechanics and convective transport processes*, volume 7. Cambridge University Press, 2007.

[17] RG Cox. The motion of long slender bodies in a viscous fluid part 1. general theory. *Journal of Fluid mechanics*, 44(4):791–810, 1970.

[18] GK Batchelor. Slender-body theory for particles of arbitrary cross-section in stokes flow. *Journal of Fluid Mechanics*, 44(3):419–440, 1970.

[19] JPK Tillett. Axial and transverse stokes flow past slender axisymmetric bodies. *Journal of Fluid Mechanics*, 44(3):401–417, 1970.

[20] Joseph B. Keller and Sol I. Rubinow. Slender-body theory for slow viscous flow. *Journal of Fluid Mechanics*, 75(4):705–714, 1976.

[21] James Geer. Stokes flow past a slender body of revolution. *Journal of Fluid Mechanics*, 78(3):577–600, 1976.

[22] Robert E. Johnson. An improved slender-body theory for stokes flow. *Journal of Fluid Mechanics*, 99(2):411–431, 1980.

[23] James Lighthill. Reinterpreting the basic theorem of flagellar hydrodynamics. pages 25–34, 1996.

[24] Shay Gueron and Nadav Liron. Ciliary motion modeling, and dynamic multicilia interactions. *Biophysical Journal*, 63(4):1045 – 1058, 1992.

[25] Shay Gueron and Nadav Liron. Simulations of Three-dimensional Ciliary Beats and Cilia Interactions. 65(June 1992):499–507, 1993.

[26] Shay Gueron, Konstantin Levit-Gurevich, Nadav Liron, and Jacob J. Blum. Cilia internal mechanism and metachronal coordination as the result of hydrodynamical coupling. *Proceedings of the National Academy of Sciences*, 94(12):6001–6006, 1997.

[27] Shay Gueron and Konstantin Levit-Gurevich. Energetic considerations of ciliary beating and the advantage of metachronal coordination. *Proceedings of the National Academy of Sciences*, 96(22):12240–12245, 1999.

[28] R. Cortez. The method of regularized stokeslets. *SIAM Journal on Scientific Computing*, 23(4):1204–1225, 2001.

[29] Susan S Suarez and AA Pacey. Sperm transport in the female reproductive tract. *Human reproduction update*, 12(1):23–37, 2006.

[30] JO Kessler. Collective behavior and dynamics of swimming bacteria. *Bacteria as multicellular organisms*, 1997.

[31] Neil H Mendelson, Adrienne Bourque, Kathryn Wilkening, Kevin R Anderson, and Joseph C Watkins. Organized cell swimming motions in bacillus subtilis colonies: patterns of short-lived whirls and jets. *Journal of bacteriology*, 181(2):600–609, 1999.

[32] John O Kessler. Dynamics of swimming bacteria at low and high volume fractions. In *Equadiff 99: (In 2 Volumes)*, pages 1284–1287. World Scientific, 2000.

[33] Christopher Dombrowski, Luis Cisneros, Sunita Chatkaew, Raymond E Goldstein, and John O Kessler. Self-concentration and large-scale coherence in bacterial dynamics. *Physical review letters*, 93(9):098103, 2004.

[34] Luis H Cisneros, Ricardo Cortez, Christopher Dombrowski, Raymond E Goldstein, and John O Kessler. Fluid dynamics of self-propelled microorganisms, from individuals to concentrated populations. In *Animal Locomotion*, pages 99–115. Springer, 2010.

[35] Andrey Sokolov, Igor S Aranson, John O Kessler, and Raymond E Goldstein. Concentration dependence of the collective dynamics of swimming bacteria. *Physical review letters*, 98(15):158102, 2007.

[36] Charles W Wolgemuth. Collective swimming and the dynamics of bacterial turbulence. *Biophysical journal*, 95(4):1564–1574, 2008.

[37] Harry Moore, Katerina Dvořáková, Nicholas Jenkins, and William Breed. Exceptional sperm cooperation in the wood mouse. *Nature*, 418(6894):174, 2002.

[38] Harry DM Moore and DA Taggart. Sperm pairing in the opossum increases the efficiency of sperm movement in a viscous environment. *Biology of reproduction*, 52(4):947–953, 1995.

[39] F Hayashi. Sperm co-operation in the fishfly, parachauliodes japonicus. *Functional Ecology*, 12(3):347–350, 1998.

[40] Ingmar H. Riedel, Karsten Kruse, and Jonathon Howard. Biophysics: A self-organized vortex array of hydrodynamically entrained sperm cells. *Science*, 309(5732):300–303, 2005.

[41] Sangtae Kim and Seppo J Karrila. *Microhydrodynamics: principles and selected applications*. Courier Corporation, 2013.

[42] TJ Pedley and JO Kessler. Hydrodynamic phenomena in suspensions of swimming microorganisms. *Annual Review of Fluid Mechanics*, 24(1):313–358, 1992.

[43] David Saintillan and Michael J Shelley. Instabilities and pattern formation in active particle suspensions: kinetic theory and continuum simulations. *Physical Review Letters*, 100(17):178103, 2008.

[44] R Aditi Simha and Sriram Ramaswamy. Hydrodynamic fluctuations and instabilities in ordered suspensions of self-propelled particles. *Physical review letters*, 89(5):058101, 2002.

[45] David Saintillan and Michael J Shelley. Orientational order and instabilities in suspensions of self-locomoting rods. *Physical review letters*, 99(5):058102, 2007.

[46] Madilyn Fletcher and Kevin C Marshall. Are solid surfaces of ecological significance to aquatic bacteria? In *Advances in microbial ecology*, pages 199–236. Springer, 1982.

[47] Christopher Brennen and Howard Winet. Fluid mechanics of propulsion by cilia and flagella. *Annual Review of Fluid Mechanics*, 9(1):339–398, 1977.

[48] AJ Reynolds. The swimming of minute organisms. *Journal of Fluid Mechanics*, 23(2):241–260, 1965.

[49] David F Katz. On the propulsion of micro-organisms near solid boundaries. *Journal of Fluid Mechanics*, 64(1):33–49, 1974.

[50] David F Katz, JR Blake, and SL Paveri-Fontana. On the movement of slender bodies near plane boundaries at low reynolds number. *Journal of Fluid Mechanics*, 72(3):529–540, 1975.

[51] DF Katz. Flagellar motions near walls. *Swimming and Flying in Nature.*, 1:173–184, 1975.

[52] Eric Lauga, Willow R DiLuzio, George M Whitesides, and Howard A Stone. Swimming in circles: motion of bacteria near solid boundaries. *Biophysical journal*, 90(2):400–412, 2006.

[53] M Ramia, DL Tullock, and N Phan-Thien. The role of hydrodynamic interaction in the locomotion of microorganisms. *Biophysical journal*, 65(2):755–778, 1993.

[54] Paul D Frymier, Roseanne M Ford, Howard C Berg, and Peter T Cummings. Three-dimensional tracking of motile bacteria near a solid planar surface. *Proceedings of the National Academy of Sciences*, 92(13):6195–6199, 1995.

[55] Paul D Frymier and Roseanne M Ford. Analysis of bacterial swimming speed approaching a solid–liquid interface. *AIChE journal*, 43(5):1341–1347, 1997.

[56] MA Vigeant and Roseanne M Ford. Interactions between motile escherichia coli and glass in media with various ionic strengths, as observed with a three-dimensional-tracking microscope. *Appl. Environ. Microbiol.*, 63(9):3474–3479, 1997.

[57] Jens Elgeti and Gerhard Gompper. Self-propelled rods near surfaces. *EPL (Europhysics Letters)*, 85(3):38002, 2009.

[58] Juan P Hernandez-Ortiz, Christopher G Stoltz, and Michael D Graham. Transport and collective dynamics in suspensions of confined swimming particles. *Physical review letters*, 95(20):204501, 2005.

[59] Lisa J Fauci and Robert Dillon. Biofluidmechanics of reproduction. *Annu. Rev. Fluid Mech.*, 38:371–394, 2006.

[60] RH Dillon, LJ Fauci, and Xingzhou Yang. Sperm motility and multiciliary beating: an integrative mechanical model. *Computers and Mathematics with Applications*, 52(5):749–758, 2006.

[61] DM Woolley. Motility of spermatozoa at surfaces. *REPRODUCTION-CAMBRIDGE-*, 126(2):259–270, 2003.

[62] David M Woolley. Flagellar oscillation: a commentary on proposed mechanisms. *Biological Reviews*, 85(3):453–470, 2010.

[63] Jens Elgeti and Gerhard Gompper. Microswimmers near surfaces. *The European Physical Journal Special Topics*, 225(11-12):2333–2352, 2016.

[64] AD Maude. Non-random distribution of bull spermatozoa in a drop of sperm suspension. *Nature*, 200(4904):381, 1963.

[65] Benjamin M Friedrich, Ingmar H Riedel-Kruse, Jonathon Howard, and Frank Julicher. High-precision tracking of sperm swimming fine structure provides strong test of resistive force theory. *Journal of Experimental Biology*, 213(8):1226–1234, 2010.

[66] H Winet, GS Bernstein, and J Head. Observations on the response of human spermatozoa to gravity, boundaries and fluid shear. *Reproduction*, 70(2):511–523, 1984.

[67] Martin Böhmer, Qui Van, Ingo Weyand, Volker Hagen, Michael Beyermann, Midori Matsumoto, Motonori Hoshi, Eilo Hildebrand, and Ulrich Benjamin Kaupp. Ca2+ spikes in the flagellum control chemotactic behavior of sperm. *The EMBO journal*, 24(15):2741–2752, 2005.

[68] J Cosson, P Huitorel, and C Gagnon. How spermatozoa come to be confined to surfaces. *Cell motility and the cytoskeleton*, 54(1):56–63, 2003.

[69] U Benjamin Kaupp, Johannes Solzin, Eilo Hildebrand, Joel E Brown, Annika Helbig, Volker Hagen, Michael Beyermann, Francesco Pampaloni, and Ingo Weyand. The signal flow and motor response controling chemotaxis of sea urchin sperm. *Nature cell biology*, 5(2):109, 2003.

[70] Anton Bukatin, Igor Kukhtevich, Norbert Stoop, Jörn Dunkel, and Vasily Kantsler. Bimodal rheotactic behavior reflects flagellar beat asymmetry in human sperm cells. *Proceedings of the National Academy of Sciences*, 112(52):15904–15909, 2015.

[71] Jens Elgeti, U Benjamin Kaupp, and Gerhard Gompper. Hydrodynamics of sperm cells near surfaces. *Biophysical journal*, 99(4):1018–1026, 2010.

[72] Jens Elgeti, U Benjamin Kaupp, and Gerhard Gompper. Response to comment on article: hydrodynamics of sperm cells near surfaces, 2011.

[73] Petr Denissenko, Vasily Kantsler, David J Smith, and Jackson Kirkman-Brown. Human spermatozoa migration in microchannels reveals boundary-following navigation. *Proceedings of the National Academy of Sciences*, 109(21):8007–8010, 2012.

[74] Jens Elgeti, Roland G Winkler, and Gerhard Gompper. Physics of microswimmers—single particle motion and collective behavior: a review. *Reports on progress in physics*, 78(5):056601, 2015.

[75] Reza Nosrati, Amine Driouchi, Christopher M Yip, and David Sinton. Two-dimensional slither swimming of sperm within a micrometre of a surface. *Nature communications*, 6:8703, 2015.

[76] David J Smith, EA Gaffney, H Gadêlha, N Kapur, and JC Kirkman-Brown. Bend propagation in the flagella of migrating human sperm, and its modulation by viscosity. *Cell motility and the cytoskeleton*, 66(4):220–236, 2009.

[77] DJ Smith, EA Gaffney, JR Blake, and JC Kirkman-Brown. Human sperm accumulation near surfaces: a simulation study. *Journal of Fluid Mechanics*, 621:289–320, 2009.

[78] Allison P Berke, Linda Turner, Howard C Berg, and Eric Lauga. Hydrodynamic attraction of swimming microorganisms by surfaces. *Physical Review Letters*, 101(3):038102, 2008.

[79] Lisa J Fauci. Interaction of oscillating filaments: a computational study. *Journal of Computational Physics*, 86(2):294–313, 1990.

[80] Gwynn J Elfring and Eric Lauga. Hydrodynamic phase locking of swimming microorganisms. *Physical review letters*, 103(8):088101, 2009.

[81] Steven H Strogatz. From kuramoto to crawford: exploring the onset of synchronization in populations of coupled oscillators. *Physica D: Nonlinear Phenomena*, 143(1-4):1–20, 2000.

[82] Simon F. Schoeller and Eric E. Keaveny. From flagellar undulations to collective motion: predicting the dynamics of sperm suspensions. *Journal of royal society interface*, 2018.

[83] Michael A Sleigh, John R Blake, and Nadav Liron. The propulsion of mucus by cilia. *American Review of Respiratory Disease*, 137(3):726–741, 1988.

[84] Douglas R Brumley, Marco Polin, Timothy J Pedley, and Raymond E Goldstein. Hydrodynamic synchronization and metachronal waves on the surface of the colonial alga volvox carteri. *Physical review letters*, 109(26):268102, 2012.

[85] Douglas R Brumley, Marco Polin, Timothy J Pedley, and Raymond E Goldstein. Metachronal waves in the flagellar beating of volvox and their hydrodynamic origin. *Journal of the Royal Society Interface*, 12(108):20141358, 2015.

[86] Peter Lenz and Andrey Ryskin. Collective effects in ciliar arrays. *Physical biology*, 3(4):285, 2006.

[87] Andrej Vilfan and Frank Jülicher. Hydrodynamic flow patterns and synchronization of beating cilia. *Physical review letters*, 96(5):058102, 2006.

[88] Boris Guirao and Jean-François Joanny. Spontaneous creation of macroscopic flow and metachronal waves in an array of cilia. *Biophysical journal*, 92(6):1900–1917, 2007.

[89] Thomas Niedermayer, Bruno Eckhardt, and Peter Lenz. Synchronization, phase locking, and metachronal wave formation in ciliary chains. *Chaos: An Interdisciplinary Journal of Nonlinear Science*, 18(3):037128, 2008.

[90] Martin Dvorkin and James Alan Shapiro. *Bacteria as Multicellular Organisms*. Oxford University Press, 1997.

[91] Vladimir A Teplov, Yuri M Romanovsky, Dmitri A Pavlov, and Wolfgang Alt. Auto-oscillatory processes and feedback mechanisms in physarum plasmodium motility. In *Dynamics of Cell and Tissue Motion*, pages 83–92. Springer, 1997.

[92] Tamás Vicsek and Anna Zafeiris. Collective motion. *Physics reports*, 517(3-4):71–140, 2012.

[93] Tamás Vicsek, András Czirók, Eshel Ben-Jacob, Inon Cohen, and Ofer Shochet. Novel type of phase transition in a system of self-driven particles. *Physical review letters*, 75(6):1226, 1995.

[94] Hiroshi Fujikawa and Mitsugu Matsushita. Fractal growth of <i>bacillus subtilis</i> on agar plates. *Journal of the Physical Society of Japan*, 58(11):3875–3878, 1989.

[95] et al. Ben-Jacob, Eshel. "generic modelling of cooperative growth patterns in bacterial colonies.". *Nature*, 364:6466, 1994.

[96] Xia-qing Shi Hugues Chate Chong Chen, Song Liu and Yilin Wu. Weak synchronization and large-scale collective oscillation in dense bacterial suspensions. *Nature*, 542:210–214, 2017.

[97] Evelyn F. Keller and Lee A. Segel. Traveling bands of chemotactic bacteria: A theoretical analysis. *Journal of Theoretical Biology*, 30(2):235 – 248, 1971.

[98] András Czirók, Eshel Ben-Jacob, Inon Cohen, and Tamás Vicsek. Formation of complex bacterial colonies via self-generated vortices. *Phys. Rev. E*, 54:1791–1801, Aug 1996.

[99] Yilin Wu, A Dale Kaiser, Yi Jiang, and Mark S Alber. Periodic reversal of direction allows myxobacteria to swarm. *Proceedings of the National Academy of Sciences*, 106(4):1222–1227, 2009.

[100] Simone Immler, Harry D.M. Moore, William G. Breed, and Tim R. Birkhead. By hook or by crook? morphometry, competition and cooperation in rodent sperm. *PLOS ONE*, 2(1):1–5, 01 2007.

[101] Nicholas Jenkins Harry Moore, Katerina Dvoráková and William Breed. Exceptional sperm cooperation in the wood mouse. *Nature*, 418:174–177, 2002.

[102] H D M Moore and D A Taggart. Sperm Pairing in the Opossum Increases the Efficiency of Sperm Movement in a Viscous Environment1. *Biology of Reproduction*, 52(4):947–953, 1995.

[103] Adama Creppy, Franck Plouraboué, Olivier Praud, Xavier Druart, Sébastien Cazin, Hui Yu, and Pierre Degond. Symmetry-breaking phase transitions in highly concentrated semen. *Journal of the Royal Society Interface*, 13(123), 2016.

[104] Adama Creppy, Olivier Praud, Xavier Druart, Philippa L. Kohnke, and Franck Plouraboué. Turbulence of swarming sperm. *Phys. Rev. E*, 92:032722, Sep 2015.

[105] Masoud Abkenar, Kristian Marx, Thorsten Auth, and Gerhard Gompper. Collective behavior of penetrable self-propelled rods in two dimensions. *Physical Review E*, 88(6):062314, 2013.

[106] HH Wensink and H Löwen. Aggregation of self-propelled colloidal rods near confining walls. *Physical Review E*, 78(3):031409, 2008.

[107] Yingzi Yang, Vincent Marceau, and Gerhard Gompper. Swarm behavior of self-propelled rods and swimming flagella. *Physical Review E*, 82(3):031904, 2010.

[108] H. H. Wensink, J. Dunkel, S. Heidenreich, K. Drescher, R. E. Goldstein, H. Lowen, and J. M. Yeomans. Meso-scale turbulence in living fluids. *Proceedings of the National Academy of Sciences*, 109(36):14308–14313, 2012.

[109] Pavel Kraikivski, Reinhard Lipowsky, and Jan Kierfeld. Enhanced ordering of interacting filaments by molecular motors. *Physical review letters*, 96(25):258103, 2006.

[110] Samuel R McCandlish, Aparna Baskaran, and Michael F Hagan. Spontaneous segregation of self-propelled particles with different motilities. *Soft Matter*, 8(8):2527–2534, 2012.

[111] Fernando Peruani, Andreas Deutsch, and Markus Bär. Nonequilibrium clustering of self-propelled rods. *Physical Review E*, 74(3):030904, 2006.

[112] Eric Bertin, Michel Droz, and Guillaume Grégoire. Hydrodynamic equations for self-propelled particles: microscopic derivation and stability analysis. *Journal of Physics A: Mathematical and Theoretical*, 42(44):445001, 2009.

[113] Francesco Ginelli, Fernando Peruani, Markus Bär, and Hugues Chaté. Large-scale collective properties of self-propelled rods. *Physical review letters*, 104(18):184502, 2010.

[114] Anton Peshkov, Igor S Aranson, Eric Bertin, Hugues Chaté, and Francesco Ginelli. Nonlinear field equations for aligning self-propelled rods. *Physical review letters*, 109(26):268701, 2012.

[115] Xu Zheng, Borge ten Hagen, Andreas Kaiser, Meiling Wu, Haihang Cui, Zhanhua Silber-Li, and Hartmut Löwen. Non-gaussian statistics for the motion of self-propelled janus particles: Experiment versus theory. *Physical Review E*, 88(3):032304, 2013.

[116] Neil H. Mendelson, Adrienne Bourque, Kathryn Wilkening, Kevin R. Anderson, and Joseph C. Watkins. Organized cell swimming motions in bacillus subtilis colonies: Patterns of short-lived whirls and jets. *Journal of Bacteriology*, 181(2):600–609, 1999.

[117] Luis H Cisneros, John O Kessler, Sujoy Ganguly, and Raymond E Goldstein. Dynamics of swimming bacteria: Transition to directional order at high concentration. *Physical Review E*, 83(6):061907, 2011.

[118] Igor S Aranson, Andrey Sokolov, John O Kessler, and Raymond E Goldstein. Model for dynamical coherence in thin films of self-propelled microorganisms. *Physical Review E*, 75(4):040901, 2007.

[119] Jörn Dunkel, Sebastian Heidenreich, Knut Drescher, Henricus H. Wensink, Markus Bär, and Raymond E. Goldstein. Fluid dynamics of bacterial turbulence. *Phys. Rev. Lett.*, 110:228102, May 2013.

[120] Robert H Kraichnan and David Montgomery. Two-dimensional turbulence. *Reports on Progress in Physics*, 43(5):547, 1980.

[121] David M Woolley, Rachel F Crockett, William DI Groom, and Stuart G Revell. A study of synchronisation between the flagella of bull spermatozoa, with related observations. *Journal of Experimental Biology*, 212(14):2215–2223, 2009.

[122] Yingzi Yang, Jens Elgeti, and Gerhard Gompper. Cooperation of sperm in two dimensions: Synchronization, attraction, and aggregation through hydrodynamic interactions. *Phys. Rev. E*, 78:061903, Dec 2008.

[123] Yingzi Yang, Feng Qiu, and Gerhard Gompper. Self-organized vortices of circling self-propelled particles and curved active flagella. *Physical Review E*, 89(1):012720, 2014.

[124] Andrea Cavagna, Alessio Cimarelli, Irene Giardina, Giorgio Parisi, Raffaele Santagati, Fabio Stefanini, and Massimiliano Viale. Scale-free correlations in starling flocks. *Proceedings of the National Academy of Sciences*, 107(26):11865–11870, 2010.

[125] William Bialek, Andrea Cavagna, Irene Giardina, Thierry Mora, Edmondo Silvestri, Massimiliano Viale, and Aleksandra M Walczak. Statistical mechanics for natural flocks of birds. *Proceedings of the National Academy of Sciences*, 109(13):4786–4791, 2012.

[126] Hugues Chaté, Francesco Ginelli, and Raúl Montagne. Simple model for active nematics: quasi-long-range order and giant fluctuations. *Physical review letters*, 96(18):180602, 2006.

[127] Hugues Chaté, Francesco Ginelli, Guillaume Grégoire, Fernando Peruani, and Franck Raynaud. Modeling collective motion: variations on the vicsek model. *The European Physical Journal B*, 64(3-4):451–456, 2008.

[128] Gabriel Baglietto and Ezequiel V Albano. Finite-size scaling analysis and dynamic study of the critical behavior of a model for the collective displacement of self-driven individuals. *Physical Review E*, 78(2):021125, 2008.

[129] Gabriel Baglietto and Ezequiel V Albano. Nature of the order-disorder transition in the vicsek model for the collective motion of self-propelled particles. *Physical Review E*, 80(5):050103, 2009.

[130] Gabriel Baglietto and Ezequiel V Albano. Computer simulations of the collective displacement of self-propelled agents. *Computer Physics Communications*, 180(4):527–531, 2009.

[131] Thomas Ihle. Kinetic theory of flocking: Derivation of hydrodynamic equations. *Physical Review E*, 83(3):030901, 2011.

[132] Shradha Mishra, Aparna Baskaran, and M Cristina Marchetti. Fluctuations and pattern formation in self-propelled particles. *Physical Review E*, 81(6):061916, 2010.

[133] Maximino Aldana, Victor Dossetti, Christian Huepe, VM Kenkre, and Hernán Larralde. Phase transitions in systems of self-propelled agents and related network models. *Physical review letters*, 98(9):095702, 2007.

[134] M Aldana, H Larralde, and B Vázquez. On the emergence of collective order in swarming systems: a recent debate. *International Journal of Modern Physics B*, 23(18):3661–3685, 2009.

[135] Jaime A Pimentel, Maximino Aldana, Cristián Huepe, and Hernán Larralde. Intrinsic and extrinsic noise effects on phase transitions of network models with applications to swarming systems. *Physical Review E*, 77(6):061138, 2008.

[136] Balázs Gönci, Máté Nagy, and Tamás Vicsek. Phase transition in the scalar noise model of collective motion in three dimensions. *The European Physical Journal Special Topics*, 157(1):53–59, 2008.

[137] Fernando Peruani, Andreas Deutsch, and Markus Bär. Nonequilibrium clustering of self-propelled rods. *Physical Review E*, 74(3):030904, 2006.

[138] Arshad Kudrolli. Concentration dependent diffusion of self-propelled rods. *Physical review letters*, 104(8):088001, 2010.

[139] D Grossman, IS Aranson, and E Ben Jacob. Emergence of agent swarm migration and vortex formation through inelastic collisions. *New Journal of Physics*, 10(2):023036, 2008.

[140] Francesco Ginelli, Fernando Peruani, Markus Bär, and Hugues Chaté. Large-scale collective properties of self-propelled rods. *Phys. Rev. Lett.*, 104:184502, May 2010.

[141] Yilin Wu, A. Dale Kaiser, Yi Jiang, and Mark S. Alber. Periodic reversal of direction allows myxobacteria to swarm. *Proceedings of the National Academy of Sciences*, 106(4):1222–1227, 2009.

[142] Udo Erdmann, Werner Ebeling, and Alexander S. Mikhailov. Noise-induced transition from translational to rotational motion of swarms. *Phys. Rev. E*, 71:051904, May 2005.

[143] A Derzsi, G Szőlősi, and T Vicsek. Most minimal spp model. *URL http://hal. elte. hu/~vicsek/SPP-minimal*, 2009.

[144] D Grossman, IS Aranson, and E Ben Jacob. Emergence of agent swarm migration and vortex formation through inelastic collisions. *New Journal of Physics*, 10(2):023036, 2008.

[145] Daniel Strombom. Collective motion from local attraction. *Journal of Theoretical Biology*, 283(1):145 – 151, 2011.

[146] Guillaume Grégoire and Hugues Chaté. Onset of collective and cohesive motion. *Phys. Rev. Lett.*, 92:025702, Jan 2004.

[147] Hugues Chaté, Francesco Ginelli, Guillaume Grégoire, and Franck Raynaud. Collective motion of self-propelled particles interacting without cohesion. *Phys. Rev. E*, 77:046113, Apr 2008.

[148] Máté Nagy, István Daruka, and Tamás Vicsek. New aspects of the continuous phase transition in the scalar noise model (snm) of collective motion. *Physica A: Statistical Mechanics and its Applications*, 373:445 – 454, 2007.

[149] John Toner, Yuhai Tu, and Sriram Ramaswamy. Hydrodynamics and phases of flocks. *Annals of Physics*, 318(1):170 – 244, 2005. Special Issue.

[150] John Toner and Yuhai Tu. Flocks, herds, and schools: A quantitative theory of flocking. *Phys. Rev. E*, 58:4828–4858, Oct 1998.

[151] John Toner and Yuhai Tu. Long-range order in a two-dimensional dynamical XY model: How birds fly together. *Phys. Rev. Lett.*, 75:4326–4329, Dec 1995.

[152] Dieter Forster, David R. Nelson, and Michael J. Stephen. Large-distance and long-time properties of a randomly stirred fluid. *Phys. Rev. A*, 16:732–749, Aug 1977.

[153] Aparna Baskaran and M. Cristina Marchetti. Statistical mechanics and hydrodynamics of bacterial suspensions. *Proceedings of the National Academy of Sciences*, 106(37):15567–15572, 2009.

[154] Aparna Baskaran and M. Cristina Marchetti. Enhanced diffusion and ordering of self-propelled rods. *Phys. Rev. Lett.*, 101:268101, Dec 2008.

[155] Fernando Peruani, Tobias Klauss, Andreas Deutsch, and Anja Voss-Boehme. Traffic jams, gliders, and bands in the quest for collective motion of self-propelled particles. *Phys. Rev. Lett.*, 106:128101, Mar 2011.

[156] F. Peruani, A. Deutsch, and M. Bär. A mean-field theory for self-propelled particles interacting by velocity alignment mechanisms. *The European Physical Journal Special Topics*, 157(1):111–122, Apr 2008.

[157] András Czirók, Katalin Schlett, Emília Madarász, and Tamás Vicsek. Exponential distribution of locomotion activity in cell cultures. *Physical Review Letters*, 81(14):3038, 1998.

[158] Christopher Dombrowski, Luis Cisneros, Sunita Chatkaew, Raymond E. Goldstein, and John O. Kessler. Self-concentration and large-scale coherence in bacterial dynamics. *Phys. Rev. Lett.,* 93:098103, Aug 2004.

[159] Leibniz Collection. Antony van Leeuwenhoekl: Tercentenary of His Discovery. 40(2):260–269, 1976.

[160] Nick Lane. The unseen world: reflections on leeuwenhoek (1677) concerning little animals;. *Philosophical Transactions of the Royal Society B: Biological Sciences,* 370(1666):20140344, 2015.

[161] J. M. Cummins and P. F. Woodall. On mammalian sperm dimensions. *Reproduction,* 75(1):153–175, 1985.

[162] Don W. Fawcett and David M. Phillips. The fine structure and development of the neck region of the mammalian spermatozoon. *The Anatomical Record,* 165(2):153–183, 1969.

[163] Peter Sutovsky and Gaurishankar Manandhar. Mammalian spermatogenesis and sperm structure: anatomical and compartmental analysis. The Sperm Cell: Production, Maturation, Fertilization, Regeneration,. 2006.

[164] E.A. Gaffney, H. Gadêlha, D.J. Smith, J.R. Blake, and J.C. Kirkman-Brown. Mammalian Sperm Motility: Observation and Theory. *Annual Review of Fluid Mechanics,* 43(1):501–528, 2011.

[165] Don W. Fawcett. The mammalian spermatozoon. *Developmental Biology,* 44(2):394 – 436, 1975.

[166] Don W. Fawcett. The structure of the mammalian spermatozoon11the author's investigations were supported by research grants c-2623 and rg-4558 (cs) from the national cancer institute of the national institutes of health, public service, united states. volume 7 of *International Review of Cytology,* pages 195 – 234. Academic Press, 1958.

[167] Peter Sutovsky, Yukihiro Terada, and Gerald Schatten. Ubiquitin-based sperm assay for the diagnosis of male factor infertility. *Human Reproduction,* 16(2):250–258, 2001.

[168] P. Sutovsky, R. Moreno, J. Ramalho-Santos, T. Dominko, W.E. Thompson, and G. Schatten. A putative, ubiquitin-dependent mechanism for the recognition and elimination of defective spermatozoa in the mammalian epididymis. *Journal of Cell Science,* 114(9):1665–1675, 2001.

[169] Effects of increased viscosity on the move ments of some invertebrate spermatozoa. *Journal of Experimental Biology*, 45(1):113–139, 1966.

[170] C. J. BROKAW. Bend propagation by a sliding filament model for flagella. *Journal of Experimental Biology*, 55(2):289–304, 1971.

[171] C.J. Brokaw. Computer simulation of flagellar movement: I. demonstration of stable bend propagation and bend initiation by the sliding filament model. *Biophysical Journal*, 12(5):564 – 586, 1972.

[172] C.J. Brokaw. Computer simulation of movement-generating cross-bridges. *Biophysical Journal*, 16(9):1013 – 1027, 1976.

[173] C J Brokaw, D J Luck, and B Huang. Analysis of the movement of chlamydomonas flagella:" the function of the radial-spoke system is revealed by comparison of wild-type and mutant flagella. *The Journal of Cell Biology*, 92(3):722–732, 1982.

[174] C J Brokaw. Microtubule sliding in swimming sperm flagella: direct and indirect measurements on sea urchin and tunicate spermatozoa. *The Journal of Cell Biology*, 114(6):1201–1215, 1991.

[175] Control of flagellar bending: A new agenda based on dynein diversity. *Cell Motility*, 28(3):199–204, 1994.

[176] Charles J Brokaw. Direct measurements of sliding between outer doublet microtubules in swimming sperm flagella. *Science*, 243(4898):1593–1596, 1989.

[177] Charles B. Lindemann and Robert Rikmenspoel. Sperm flagella: Autonomous oscillations of the contractile system. *Science*, 175(4019):337–338, 1972.

[178] Charles B. Lindemann, Walter G. Rudd, and Robert Rikmenspoel. The stiffness of the flagella of impaled bull sperm. *Biophysical Journal*, 13(5):437 – 448, 1973.

[179] Charles B. Lindemann. A model of flagellar and ciliary functioning which uses the forces transverse to the axoneme as the regulator of dynein activation. *Cell Motility*, 29(2):141–154, 1994.

[180] Zachary Bird, Robert Hard, Kathleen S. Kanous, and Charles B. Lindemann. Inter-doublet sliding in bovine spermatozoa: Its relationship to flagellar motility and the action of inhibitory agents. *Journal of Structural Biology*, 116(3):418 – 428, 1996.

[181] Charles B. Lindemann. Functional significance of the outer dense fibers of mammalian sperm examined by computer simulations with the geometric clutch model. *Cell Motility*, 34(4):258–270, 1996.

[182] Charles B. Lindemann. Geometric clutch model version 3: The role of the inner and outer arm dyneins in the ciliary beat. *Cell Motility*, 52(4):242–254, 2002.

[183] Charles B. Lindemann. Testing the geometric clutch hypothesis. *Biology of the Cell*, 96(9):681–690, 2004.

[184] C. B. Lindemann and K. S. Kanous. Regulation of mammalian sperm motility. *Archives of Andrology*, 23(1):1–22, 1989.

[185] Charles B Lindemann. Heart of the Beat (the Flagellar Beat, that Is). *Biophysj*, 97(11):2865–2866, 2009.

[186] Charles B. Lindemann and Kathleen A. Lesich. Flagellar and ciliary beating: the proven and the possible. *Journal of Cell Science*, 123(4):519–528, 2010.

[187] Charles B. Lindemann and Robert Rikmenspoel. Sperm flagella: Autonomous oscillations of the contractile system. *Science*, 175(4019):337–338, 1972.

[188] Jinzhou Yuan, Jessie Zhou, David M Raizen, and Haim H Bau. High-throughput, motility-based sorter for microswimmers such as c. elegans. *Lab on a Chip*, 15(13):2790–2798, 2015.

[189] Juliane Simmchen, Jaideep Katuri, William E Uspal, Mihail N Popescu, Mykola Tasinkevych, and Samuel Sánchez. Topographical pathways guide chemical microswimmers. *Nature communications*, 7:10598, 2016.

[190] Jiang Zhuang and Metin Sitti. Chemotaxis of bio-hybrid multiple bacteria-driven microswimmers. *Scientific reports*, 6:32135, 2016.

[191] Jinzhou Yuan. Microswimmers and microfluidics: Understanding and manipulating the locomotion of undulatory microswimmers. 2015.

[192] Saurabh Vyawahare, Andrew D Griffiths, and Christoph A Merten. Miniaturization and parallelization of biological and chemical assays in microfluidic devices. *Chemistry & biology*, 17(10):1052–1065, 2010.

[193] Brian M Paegel, Robert G Blazej, and Richard A Mathies. Microfluidic devices for dna sequencing: sample preparation and electrophoretic analysis. *Current opinion in biotechnology*, 14(1):42–50, 2003.

[194] Sebastian J Maerkl. Integration column: Microfluidic high-throughput screening. *Integrative Biology*, 1(1):19–29, 2008.

[195] JE Mark, HR Allcock, and R West. Inorganic polymers prentice hall. *New Jersey, USA*, 1992.

[196] Mark Wang, Erhan Polatkan Ata, and Sadik C Esener. Microfluidic sorting device, June 27 2006. US Patent 7,068,874.

[197] Dongeun Huh, Joong Hwan Bahng, Yibo Ling, Hsien-Hung Wei, Oliver D Kripfgans, J Brian Fowlkes, James B Grotberg, and Shuichi Takayama. Gravity-driven microfluidic particle sorting device with hydrodynamic separation amplification. *Analytical chemistry*, 79(4):1369–1376, 2007.

[198] Pun-Pang Shiu, George K Knopf, Mile Ostojic, and S Nikumb. Rapid fabrication of tooling for microfluidic devices via laser micromachining and hot embossing. *Journal of Micromechanics and Microengineering*, 18(2):025012, 2008.

[199] Kevin Ward and Z Hugh Fan. Mixing in microfluidic devices and enhancement methods. *Journal of Micromechanics and Microengineering*, 25(9):094001, 2015.

[200] Alireza Bahadorimehr and Burhanuddin Yeop Majlis. Fabrication of glass-based microfluidic devices with photoresist as mask. *Informacije MIDEM*, 41(3):193–196, 2011.

[201] Ziya Isiksacan, M Tahsin Guler, Berkan Aydogdu, Ismail Bilican, and Caglar Elbuken. Rapid fabrication of microfluidic pdms devices from reusable pdms molds using laser ablation. *Journal of Micromechanics and Microengineering*, 26(3):035008, 2016.

[202] Ciprian Iliescu, Hayden Taylor, Marioara Avram, Jianmin Miao, and Sami Franssila. A practical guide for the fabrication of microfluidic devices using glass and silicon. *Biomicrofluidics*, 6(1):016505, 2012.

[203] J Cooper McDonald, David C Duffy, Janelle R Anderson, Daniel T Chiu, Hongkai Wu, Olivier JA Schueller, and George M Whitesides. Fabrication of microfluidic systems in poly (dimethylsiloxane). *ELECTROPHORESIS: An International Journal*, 21(1):27–40, 2000.

[204] John A Rogers and Ralph G Nuzzo. Recent progress in soft lithography. *Materials today*, 8(2):50–56, 2005.

[205] David C. Duffy, J. Cooper McDonald, Olivier J. A. Schueller, and George M. Whitesides. Rapid prototyping of microfluidic systems in poly(dimethylsiloxane). *Analytical Chemistry*, 70(23):4974–4984, 1998. PMID: 21644679.

[206] Adrien Plecis and Yong Chen. Fabrication of microfluidic devices based on glass–pdms–glass technology. *Microelectronic Engineering*, 84(5-8):1265–1269, 2007.

[207] James Friend and Leslie Yeo. Fabrication of microfluidic devices using polydimethylsiloxane. *Biomicrofluidics*, 4(2):026502, 2010.

[208] Björn Samel, M Kamruzzaman Chowdhury, and Göran Stemme. The fabrication of microfluidic structures by means of full-wafer adhesive bonding using a poly (dimethylsiloxane) catalyst. *Journal of Micromechanics and Microengineering*, 17(8):1710, 2007.

[209] Fulvio Scarano Christian J. Kähler Steven T. Wereley Jürgen Kompenhans Markus Raffel, Christian E. Willert. *Particle Image Velocimentry: a practical guide.* 2007.

[210] Manabu Iguchi Tomomasa Uemura, Yoshiaki Ueda. *Flow Visualization in Materials Processing.* 2018.

[211] Ronald J Adrian. Particle-imaging techniques for experimental fluid mechanics. *Annual review of fluid mechanics*, 23(1):261–304, 1991.

[212] Azriel Rosenfeld. *Digital picture processing*. Academic press, 1976.

[213] WK Pratt. Digital image processing and analysis. In *In Von Karman Inst. for Fluid Dynamics Digital Image Processing in Fluid Dyn. 140 p (SEE N84-25973 16-34)*, 1984.

[214] W. Thielicke and E.J. Stamhuis. Pivlab – towards user-friendly, affordable and accurate digital particle image velocimetry in matlab. *Journal of Open Research Software 2*, 1:e30, 2014.

[215] Jerry Westerweel. Fundamentals of digital particle image velocimetry. *Measurement science and technology*, 8(12):1379, 1997.

[216] A Melling. Tracer particles and seeding for particle image velocimetry. *Measurement science and technology*, 8(12):1406, 1997.

[217] T Zhang, D Celik, and SW Van Sciver. Tracer particles for application to piv studies of liquid helium. *Journal of low temperature physics*, 134(3-4):985–1000, 2004.

[218] JW Hoyt and RHJ Sellin. A comparison of tracer and piv results in visualizing water flow around a cylinder close to the free surface. *Experiments in Fluids*, 28(3):261–265, 2000.

[219] Wing T Lai, Daniel C Bjorkquist, Martin P Abbott, and Amir A Naqwi. Video systems for piv recording. *Measurement Science and Technology*, 9(3):297, 1998.

[220] L Gui and W Merzkirch. A comparative study of the mqd method and several correlation-based piv evaluation algorithms. *Experiments in Fluids*, 28(1):36–44, 2000.

[221] K Okamoto, YA Hassan, and WD Schmidl. New tracking algorithm for particle image velocimetry. *Experiments in Fluids*, 19(5):342–347, 1995.

[222] RC Singleton. An algorithm for computing the mixed radix fast fourier transform. *IEEE Transactions on audio and electroacoustics*, 17(2):93–103, 1969.

[223] Richard D Keane and Ronald J Adrian. Optimization of particle image velocimeters. i. double pulsed systems. *Measurement science and technology*, 1(11):1202, 1990.

[224] Alfred Vogel and Werner Lauterborn. Time-resolved particle image velocimetry used in the investigation of cavitation bubble dynamics. *Applied Optics*, 27(9):1869–1876, 1988.

[225] Jerry Westerweel, D Dabiri, and Morteza Gharib. The effect of a discrete window offset on the accuracy of cross-correlation analysis of digital piv recordings. *Experiments in fluids*, 23(1):20–28, 1997.

[226] Thomas Rösgen and R Totaro. Two-dimensional on-line particle imaging velocimetry. *Experiments in Fluids*, 19(3):188–193, 1995.

[227] HT Huang, HE Fiedler, and JJ Wang. Limitation and improvement of piv. *Experiments in fluids*, 15(4-5):263–273, 1993.

[228] C Freek, JMF Raposo, JMM Sousa, W Hentschel, and W Merzkirch. On the accuracy of a dic-piv system based on massive sampling. In *Proc 9th Int Symp on Applications of Laser Techniques to Fluid Mechanics, Lisbon, Portugal*, pages 13–16, 1998.

[229] L Gui and W Merzkirch. Generating arbitrarily sized interrogation windows for correlation-based analysis of particle image velocimetry recordings. *Experiments in fluids*, 24(1):66–69, 1998.

[230] Jeremy M Coupland and Neil A Halliwell. Particle image velocimetry: rapid transparency analysis using optical correlation. *Applied optics*, 27(10):1919–1921, 1988.

[231] FK Browand and DA Plocher. Image processing for sediment transport. In *NATL. CONF. PUBL. INST. ENG. AUST. 1985.*, 1985.

[232] DB Barker and ME Fourney. Measuring fluid velocities with speckle patterns. *Optics letters*, 1(4):135–137, 1977.

[233] Ronald J Adrian. Scattering particle characteristics and their effect on pulsed laser measurements of fluid flow: speckle velocimetry vs particle image velocimetry. *Applied optics*, 23(11):1690–1691, 1984.

[234] Roland Meynart. Speckle velocimetry study of vortex pairing in a low-re unexcited jet. *The Physics of fluids*, 26(8):2074–2079, 1983.

[235] L Lourenco and A Krothapalli. The role of photographic parameters in laser speckle or particle image displacement velocimetry. *Experiments in Fluids*, 5:29–32, 1987.

[236] Juan C Agüí and J Jimenez. On the performance of particle tracking. *Journal of fluid mechanics*, 185:447–468, 1987.

[237] Markus Raffel, Christian E Willert, Fulvio Scarano, Christian J Kähler, Steve T Wereley, and Jürgen Kompenhans. *Particle image velocimetry: a practical guide*. Springer, 2018.

[238] Hazime Mori. Transport, collective motion, and brownian motion. *Progress of theoretical physics*, 33(3):423–455, 1965.

[239] George E Uhlenbeck and Leonard S Ornstein. On the theory of the brownian motion. *Physical review*, 36(5):823, 1930.

[240] MA Islam. Einstein–smoluchowski diffusion equation: a discussion. *Physica Scripta*, 70(2-3):120, 2004.

[241] Reza Sadr, Haifeng Li, and Minami Yoda. Impact of hindered brownian diffusion on the accuracy of particle-image velocimetry using evanescent-wave illumination. *Experiments in fluids*, 38(1):90–98, 2005.

[242] Christian E Willert and Morteza Gharib. Digital particle image velocimetry. *Experiments in fluids*, 10(4):181–193, 1991.

[243] Ronald J Adrian. Image shifting technique to resolve directional ambiguity in double-pulsed velocimetry. *Applied Optics*, 25(21):3855–3858, 1986.

[244] RJ Adrian. Multi-point optical measurements of simultaneous vectors in unsteady flow—a review. *International journal of heat and fluid flow*, 7(2):127–145, 1986.

[245] Shendruk T. N. Thijssen K. Yeomans J. M. Doostmohammadi, A. Onset of meso-scale turbulence in active nematics. *Nature communications*, 8:15326, 2017.

[246] Héctor Matías López, Jérémie Gachelin, Carine Douarche, Harold Auradou, and Eric Clément. Turning bacteria suspensions into superfluids. *Physical review letters*, 115(2):028301, 2015.

[247] Andrey Sokolov and Igor S Aranson. Reduction of viscosity in suspension of swimming bacteria. *Physical Review Letters*, 103(14):148101, 2009.

[248] Jérémie Gachelin, Gastón Mino, Hélene Berthet, Anke Lindner, Annie Rousselet, and Éric Clément. Non-newtonian viscosity of escherichia coli suspensions. *Physical review letters*, 110(26):268103, 2013.

[249] D. J. SMITH, E. A. GAFFNEY, J. R. BLAKE, and J. C. KIRKMAN-BROWN. Human sperm accumulation near surfaces: a simulation study. *Journal of Fluid Mechanics*, 621:289–320, 2009.

[250] E.A. Gaffney, H. Gadêlha, D.J. Smith, J.R. Blake, and J.C. Kirkman-Brown. Mammalian sperm motility: Observation and theory. *Annual Review of Fluid Mechanics*, 43(1):501–528, 2011.

[251] Enkeleida Lushi, Hugo Wioland, and Raymond E. Goldstein. Fluid flows created by swimming bacteria drive self-organization in confined suspensions. *Proceedings of the National Academy of Sciences*, 111(27):9733–9738, 2014.

[252] Kazusa Beppu, Ziane Izri, Jun Gohya, Kanta Eto, Masatoshi Ichikawa, and Yusuke T. Maeda. Geometry-driven collective ordering of bacterial vortices. *Soft Matter*, 13:5038–5043, 2017.

[253] Hugo Wioland, Francis G. Woodhouse, Jörn Dunkel, John O. Kessler, and Raymond E. Goldstein. Confinement stabilizes a bacterial suspension into a spiral vortex. *Phys. Rev. Lett.*, 110:268102, Jun 2013.

[254] Camille Boutin, Paul Labedan, Jordane Dimidschstein, Fabrice Richard, Harold Cremer, Philipp André, Yingzi Yang, Mireille Montcouquiol, Andre M. Goffinet, and Fadel Tissir. A dual role for planar cell polarity genes in ciliated cells. *Proceedings of the National Academy of Sciences*, 111(30):E3129–E3138, 2014.